Technische Universität München
Department of Informatics

PhD Thesis

Advanced Reconstruction and Noise Reduction Techniques in Four- and Six-Dimensional X-ray Imaging Modalities

Saeed Seyyedi

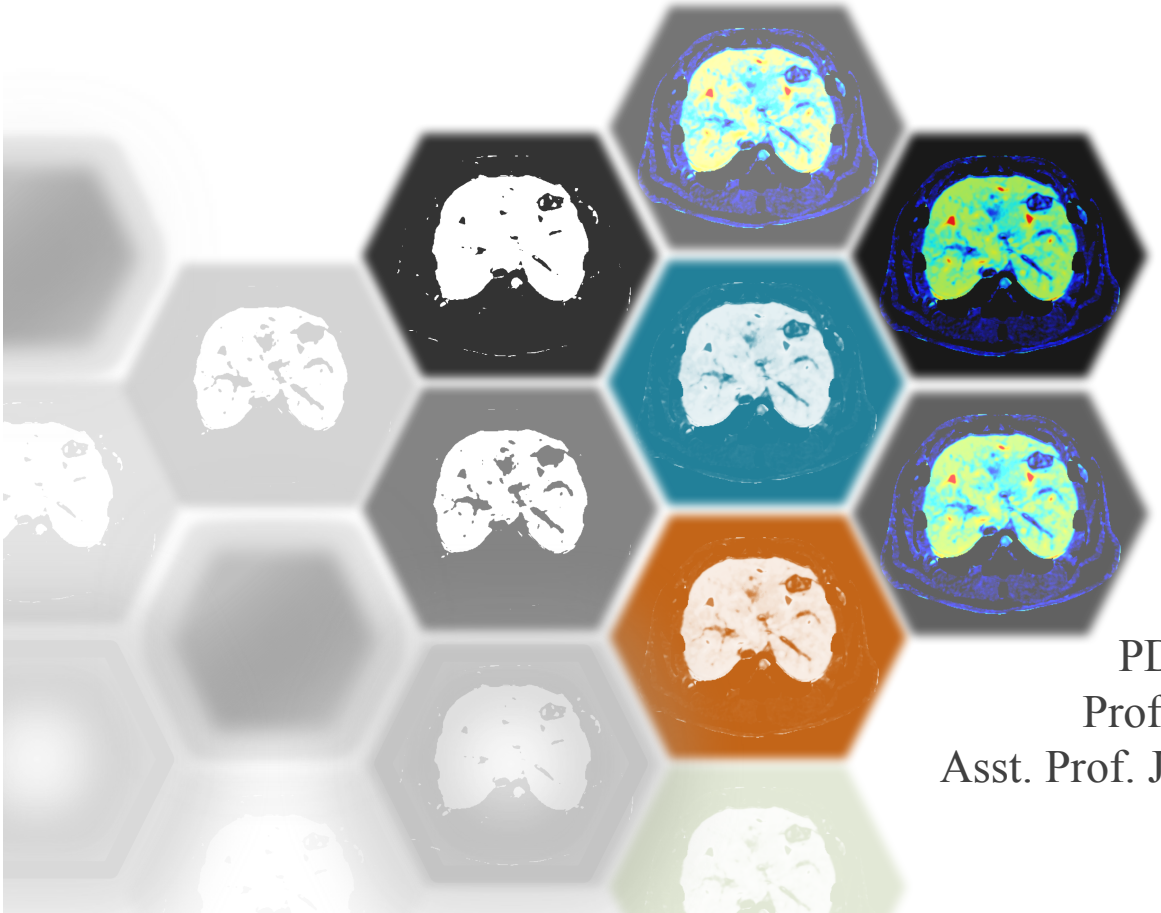

Supervisors:
PD Dr. Tobias Lasser
Prof. Dr. Franz Pfeiffer
Asst. Prof. J. Webster Stayman

July 2018

Technische Universität München
Informatik Department

Advanced Reconstruction and Noise Reduction Techniques in Four- and Six-Dimensional X-ray Imaging Modalities

Saeed Seyyedi

Vollständiger Abdruck der von der Fakultät für Informatik der Technischen Universität München zur Erlangung des akademischen Grades eines

Doktors der Naturwissenschaften (Dr. rer. nat.)

genehmigten Dissertation.

Vorsitzender: Univ.-Prof. Dr.-Ing. Darius Burschka

Prüfer der Dissertation:

1. Priv.-Doz. Dr. Tobias Lasser
2. Prof. Dr. Franz Pfeiffer
3. Assistant Prof. J. Webster Stayman, Ph.D.
   Johns Hopkins University, Baltimore, MD, USA

Die Dissertation wurde am 12.04.2018 bei der Technischen Universität München eingereicht und durch die Fakultät für Informatik am 28.06.2018 angenommen.

Abstract

Modern imaging modalities have revolutionized our lives by offering a deeper understanding of the nature. Discovery of x-rays however, allowed the exploration of different structures and to exploit a micro-scaled information of human bodies, industrial objects and materials. In total, several imaging modalities became available using different types of x-ray contrasts, namely, absorption, phase contrast and dark-field.

In this work, we study two modern x-ray imaging modalities and propose several data processing and analysis chains along with evaluation techniques to investigate the effectiveness of proposed methods.

In the first part, we study X-ray Tensor Tomography, a novel imaging modality for three-dimensional reconstruction of x-ray scattering tensors from dark-field images obtained in a grating interferometry setup. One of the main limitations of X-ray Tensor Tomography is the degradation of the measured two-dimensional dark-field images due to the detector readout noise and insufficient photon statistics which is consequently affecting the three-dimensional volumes reconstructed from this data.

In this study, we investigate different two- and three-dimensional noise reduction and regularized reconstruction methods based on Total Variation technique incorporated into the XTT processing pipeline using different schemes. The quantitative and qualitative evaluation based on datasets from several industrial material samples as well as a clinical sample reveal both qualitative and quantitative improvements in noise reduction for all proposed methods compared to the method without denoising.

In the second part, we study Liver CT perfusion which is a novel x-ray imaging technique to enable the evaluation of perfusion metrics that can reveal hepatic diseases and that can be used to assess treatment responses. Despite the several potential applications of CTP, associated x-ray radiation dose with hepatic CTP studies is significant, as it requires many CT datasets spread over about a minute of acquisition. Radiation dose issues limit the more widespread use of CT perfusion as a diagnostic tool. Several traditional image processing methods have been proposed to reconstruct individual temporal samples. However, the sequential scans acquired in CT perfusion share a large amount of anatomical information between temporal samples suggesting an opportunity for improved data processing.

In this work, we adopted a prior-image-based reconstruction approach called Reconstruction of Difference to enable low-exposure data collections in CTP. Several simulation studies have been performed using a four-dimensional digital anthropomorphic phantom which was derived from a combination of human models and measured time-attenuation curves from animal studies. Several evaluations have been performed to assess the quality of temporal reconstructions and the accuracy of the estimated time-attenuation curves, and to investigate the common perfusion metric maps including hepatic arterial perfusion, hepatic portal perfusion, hepatic perfusion index and time-to-peak. The studies suggest that Reconstruction of Difference enables significant exposure reductions and can outperform both standard analytic reconstruction as well as more sophisticated

model-based reconstruction.

Zusammenfassung

Moderne Bildgebungsmodalitäten erlauben ein tieferes Verständnis der Natur und haben dadurch unser Leben revolutioniert. Die Entdeckung von Röntgenstrahlen ermöglichte die Erforschung von verschiedenen Strukturen und die Ausnutzung von Informationen über den menschlichen Körper, industrielle Objekte und Materialien auf Mikroskalen. Insgesamt wurden mehrere Bildgebungsverfahren entwickelt, die verschiedene Röntgen-Kontrastmechanismen benutzen, insbesondere Absorption, Phasen-Kontrast und Dunkelfeld.

In dieser Arbeit untersuchen wir zwei moderne Röntgen-Bildgebungsmodalitäten und stellen mehrere Algorithmen für Datenverarbeitung und Datenanalyse vor, zusammen mit Auswertungstechniken um die Effektivität der vorgeschlagenen Methoden zu prüfen.

Im ersten Teil untersuchen wir „X-ray Tensor Tomography“, eine neue Bildgebungs modalität zur drei-dimensionale Rekonstruktion von Röntgen-Streutensoren aus Bildern, die in einem Grating Interferometer aufgenommen wurden. Eine der größten Limitationen der X-ray Tensor Tomography ist die Verschlechterung der gemessenen, zweidimensionalen Dunkelfeld-Bilder durch Rauschen beim Auslesen des Detektors sowie durch ungenügende Photonen-Statistiken, was in Folge in den von diesen Daten rekonstruierten drei-dimensionalen Volumen ebenfalls zu Artefakten aufgrund von Rauschen führt.

In dieser Arbeit untersuchen wir verschiedene zwei- und drei-dimensionale Methoden zur Reduktion von Rauschen sowie Regularisierungs-Methoden basierend auf der „Total Variation“ Technik, die auf verschiedene Arten in die XTT Bearbeitungs-Pipeline eingebunden werden. Die quantitative und qualitative Evaluation auf Basis von Datensätzen von verschiedenen industriellen Materialproben und einer klinischen Materialprobe zeigen Verbesserungen in der Rauschunterdrückung bei allen drei Methoden im Vergleich zu der Methode ohne Rauschunterdrückung.

Im zweiten Teil untersuchen wir Leber CT Perfusion (CTP), eine neue Röntgen Bildgebungs-Technik, die die Evaluierung von Perfusions-Metriken erlaubt, wodurch hepatische Krankheiten entdeckt werden können, und womit der Behandlungserfolg eingeschätzt werden kann. Trotz einige potentieller Anwendungen von CTP ist die damit assoziierte Röntgen Strahlendosis für hepatische CTP Studien signifikant hoch, da mehrere CT Datensätze über eine Minute hinweg aufgenommen werden müssen. Das Problem der Strahlendosis beschränkt daher den weiteren, grösser angelegten Einsatz von CTP als ein diagnostisches Hilfsmittel. Einige traditionelle Bildverarbeitungsmethoden wurden bereits vorgeschlagen, um einzelne zeitliche Aufnahmen zu rekonstruieren. Allerdings teilen sich die sequentiellen Aufnahmen, die in CTP gemacht werden, einen großen Anteil von anatomischen Informationen zwischen den einzelnen zeitlichen Aufnahmen, was eine Gelegenheit bietet für verbesserte Bildverarbeitungsmethoden.

In dieser Arbeit adaptieren wir a-priori Informationen in die Rekonstruktionsmethode, genannt „Reconstruction of Difference“, um CTP Aufnahmen mit einer geringen Strahlendosis zu ermöglichen. Verschiedene Simulations-Studien wurden durchge-

führt anhand eines vier-dimensionalen anthropomorphischen Phantoms, das wir aus einer Kombination von menschlichen Modellen und gemessenen Abschwächungskurven aus Tierstudien. Verschiedene Auswertungen wurden durchgeführt um die Qualität der Rekonstruktionen zu beurteilen in Hinblick auf Zeit und Genauigkeit der Zeit-Abschwächungs-Kurven, und um die allgemeinen Perfusions-Metriken zu untersuchen, insbesondere die hepatische arterielle Perfusion, die hepatische Portal-Perfusion, den hepatischen Perfusions-Index und die Zeit bis zum Peak. Die Studien legen nahe, dass durch die „Reconstruction of Difference“-Methode signifikante Reduktionen in der Strahlendosis möglich sind, und dass die Methode sowohl die Standard-Methoden der analytischen Rekonstruktion und andere, hoch-entwickelte Modell-basierte Methoden übertreffen kann.

Contents

Part I.

INTRODUCTION

1. Basics

> Great discoveries are made accidentally less often than the populace likes to think.
>
> *A Shorter History of Science* [Dam13]
> *Sir William Cecil Dampier*

Electromagnetic waves can be classified and arranged according to their varying frequencies; this classification is called electromagnetic spectrum. Visible light region - the only part of electromagnetic spectrum we can see, is a very narrow band of wavelengths that is located to the right of the infrared region and to the left of the ultraviolet region (see Figure 1.1). As the full spectrum of visible light travels through a prism, the wavelengths separate into the colors of the rainbow due to the different wavelength of each color. Red has the longest wavelength at around 700 nanometers and violet has the shortest wavelength at around 380 nanometers. When all the waves are seen together, they make white light.

In the year 1665, Sir Isaac Newton experimented with light using a prism. In his experiments, Newton had proved that white light was made up of colors mixed together, and the prism merely separated them - he was the first person to understand the rainbow [New04].

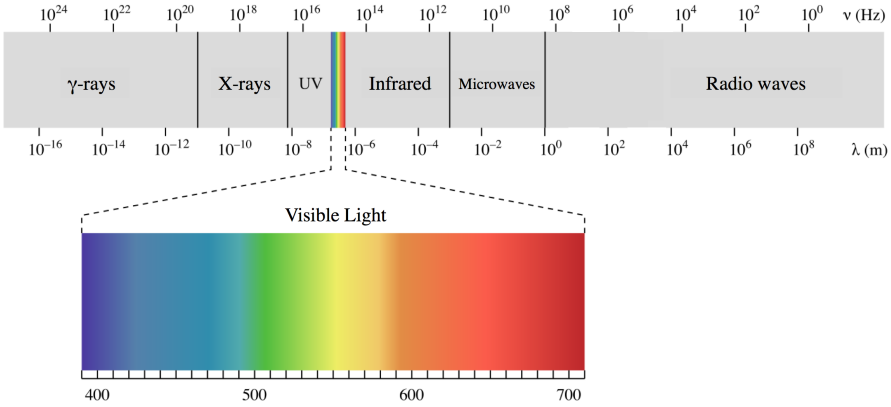

Figure 1.1.: The Electromagnetic spectrum describes all the wavelengths of light. The electromagnetic waves that human eyes detect – visible light – oscillates between 400 and 790 terahertz.

In the year 1800, Sir William Herschel was exploring the question of how much heat was contained by the different colors of visible light [Her00]. In his experiment, he placed several thermometers under each color separated using a glass prism and found that the thermometer that was seemingly out of the light had the highest temperature. Thus,

he discovered infrared light. A year later, Johann Wilhelm Ritter discovered ultraviolet light [Rit06].

In 1867, James Clerk Maxwell, an English scientist, developed a scientific theory to explain electromagnetic waves [Max65]. He noticed that electrical fields and magnetic fields can couple together to form electromagnetic waves. Neither an electrical field, nor a magnetic field will go anywhere by themselves. But, Maxwell discovered that a changing magnetic field will induce a changing electric field and vice-versa.

In 1887 Heinrich Hertz, a German physicist, applied Maxwell's theories to the production and reception of radio waves [Her87]. In his laboratory, Hertz proved the existence of radio waves in the late 1880s. Hertz showed that these signals possessed all of the properties of electromagnetic waves.

It took a bit longer for scientists to discover the higher-energy light in the electromagnetic spectrum.

2. X-ray based Imaging

X-ray imaging has been proven to be an incredible component of several medical diagnostic and treatment techniques as well as many industrial Inspections of solid materials and products. X-ray technology is the oldest and most commonly used form of imaging that uses ionizing radiation to produce images of the internal structure of different objects. Owing to the recent advances in computing power, several x-ray based imaging devices and techniques have been developed and are in use in medical and non-medical applications, including computed tomography (CT), mammography, interventional radiology and digital radiography.

2.1 X-radiation or Röntgen-rays

In the evening of November 8, 1895, Wilhelm Röntgen , a German professor of physics, was the first person to discover electromagnetic radiation in a wavelength range commonly known as x-radiation or x-rays today, a significant scientific advancement that became a useful tool for experiments and observations in several different applications such as medical imaging and industrial objects' inspection [Rön96]. Although, many people had observed the effects of x-ray beams before, Röntgen was the first person to study them systematically. To highlight the unknown nature of his discovery, he called them x-rays, though they are still known as Röntgen-rays as well. The first x-ray image was taken in the same year from Prof. Röntgen's wife which was recorded on a film, showing the finger bones and her ring (see Figure 2.1).

For his remarkable achievement, he was honored with the first Nobel Prize in Physics in 1901. The award was officially "in recognition of the extraordinary services he has rendered by the discovery of the x-rays or Röntgen-rays subsequently named after him" [AB14].

Royal Swedish Academy of Sciences, mentioned this achievement of Röntgen using the following words [Odh01]:

> *"Academy awarded the Nobel Prize in Physics to Wilhelm Conrad Röntgen, Professor in the University of Munich, for the discovery with which his name is linked for all time: the discovery of the so-called Röntgen rays or, as he himself called them, x-rays. These are, as we know, a new form of energy and have received the name "rays" on account of their property of propagating themselves in straight lines as light does. The actual constitution of this radiation of energy is still unknown. Several of its characteristic properties have, however, been discovered first by Röntgen himself and then by other physicists who have directed their researches into this field. And there is no doubt that much success will be gained in physical science when this strange energy form is sufficiently investigated and its wide field thoroughly explored. Let us remind ourselves of but one of the properties which have been found in Röntgen rays; that which is the basis of the extensive use of x-rays in medical practice. Many bodies,*

Figure 2.1.: The first x-ray projection was taken in 1895 from Prof. Wilhelm Röntgen's wife which was recorded on a film, showing the finger bones and her ring [Kev98].

> *just as they allow light to pass through them in varying degrees, behave likewise with x-rays, but with the difference that some which are totally impenetrable to light can easily be penetrated by x-rays, while other bodies stop them completely. Thus, for example, metals are impenetrable to them; wood, leather, cardboard and other materials are penetrable and this is also the case with the muscular tissues of animal organisms... ."*

2.2 Generation of X-rays

X-rays are waves of electromagnetic energy. They behave in a similar way as light rays, but at much shorter wavelengths - in the range of 0.01-10 nm - and are capable of penetrating some thickness of matter. There are three major ways that x-rays are generated. The most common is the Bremsstrahlung process. Bremsstrahlung is a German term that means "braking rays". It is an important phenomenon in the generation of x-rays where rays are produced by slowing down of the primary beam electrons by the electric field surrounding the nuclei of the atoms in the sample [Low58].

Another method is K-shell emission, where a high energy electron knocks an electron from an inner orbit in an atom, and an x-ray is emitted with the replacement of that electron.

The third method occurs in a synchrotron, which is a subatomic particle accelerator that creates high intensity x-rays used for nuclear studies.

2.2.1 X-ray Tubes

The x-ray tubes serve the function of creating x-ray photons from electric energy supplied by the x-ray generator [oth60; HN82; Nas14]. An x-ray tube is a vacuum tube which is converting electrical input power into the x-rays. X-ray tubes have evolved from the experimental Crookes tubes with which Röntgen implemented his first experiments. Crookes tubes are cold cathode tubes which means that they do not include a heated filament in them to release electrons like the later electronic vacuum tubes. Instead,

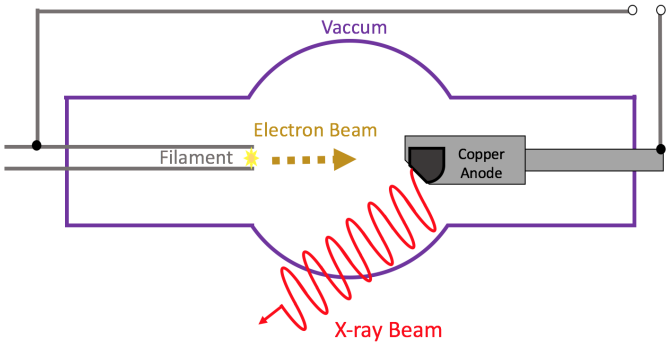

Figure 2.2.: A diagram of a modern x-ray tube. This type of tube was devised by Coolidge in 1913 [SP08].

electrons are generated by the ionization of the residual air by a high DC voltage which is applied between the electrodes [Beh15; Alb77].

In 1913, William Coolidge invented the Coolidge tube, an x-ray tube with an improved cathode to be used in x-ray machines which enabled more intense visualization of deep-seated anatomy and tumors. Figure 2.2 illustrates basic parts of an original Coolidge tube including a spherical bulb with two cylindrical arms, cathode arm and the anode arm [Coo16].

2.2.2 Synchrotron X-rays

X-ray photons can also be created under different conditions. A synchrotron is an extremely powerful source of x-rays. The x-rays are produced by high energy electrons which circulate around the synchrotron. Synchrotron x-rays can be used for traditional x-ray imaging, phase-contrast x-ray imaging, and tomography. The Ångström-scale wavelength of x-rays enables imaging well below the diffraction limit of visible light [Win97; Wil91; Van79]. Extremely bright, short x-ray pulses which are tuned to selected wavelength regions, have several applications including the probing of chemical reactions on surfaces, electronic structures of semiconductors and magnetic materials, the structure and function of proteins and biological macromolecules and also for photon activation therapy, tomotherapy, microbeam radiation therapy [Lew97; AJ94; Bla05].

2.3 Interaction of X-rays with Matter

X-rays in the diagnostic range interact with matter via two main processes, which are fundamental of the image formation in a radiographic measurement process. These processes are the photoelectric effect (photoelectric absorption) and Compton effect or Compton scattering [Set06; Spa94].

Photoelectric absorption (PEA) is a form of interaction of x-rays or gamma photons with the matter (see Figure 2.3). A low energy photon interacts with the electron in the atom and remove it from its shell. Photoelectric interactions usually happen with electrons that are firmly bound to the atoms with a relatively high binding energy.

Photoelectric interactions are most probable when the energy of the electron is slightly less than the photon energy. If the binding energy is more than the energy of the photon,

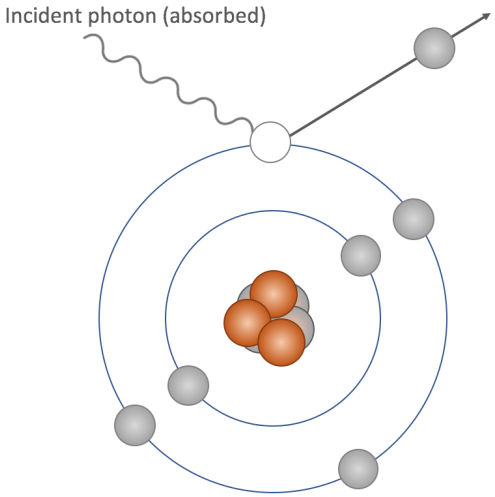

Figure 2.3.: Photoelectric absorption process: a photon undergoes an interaction with an absorber atom in which the photon completely disappears.

a photoelectric interaction will not occur. This interaction occurs only when the photon has enough energy to overcome the binding energy and to remove the electron from its atom [Eva68].

Compton effect or Compton scattering is another form of photon interaction. It is the main cause of scattered radiation in a material which happens due to the interaction of the x-rays or gamma photons with free electrons (unattached to atoms) or loosely bound valence shell (outer shell) electrons [Hub82; Eva68] (see Figure 2.4).

2.4 Applications of X-rays

In clinical applications, two-dimensional Röntgen images as well as three-dimensional images of human body acquired in computed tomography (CT) scanners are obtained by using x-rays.

Several x-ray imaging modalities have been developed based on the different attenuation of x-rays in the structures [WK03]. Different composition and density of tissues are the causes for the variance in x-ray transmissions. For instance, hard tissues like skeletal structures absorb x-rays more than lowly absorbing parts, such as surrounding tissues. However, low x-ray attenuation acquired in softer tissues like liver and some of the lesions which usually contain only minor density difference, results in poor x-ray images [HRH03]. More advanced x-ray imaging techniques such as CT perfusion (CTP) imaging method, have been recently developed to address these limitations by employing contrast administrations in combination with dynamic acquisition based imaging methods [Win05; Koe98; Pan05]. Recently, an advanced family of x-ray imaging techniques have been developed by using different physical concepts such as phase-contrast rather than traditionally used attenuation contrast [Mar16; Mom96; Pfe07; BCS12; Hoh06]. X-ray dark-field imaging is another instance of the newly developed x-ray imaging modalities which is being used for measurements and reconstruction of different clinical and non-clinical samples [Pfe08b; Jen10].

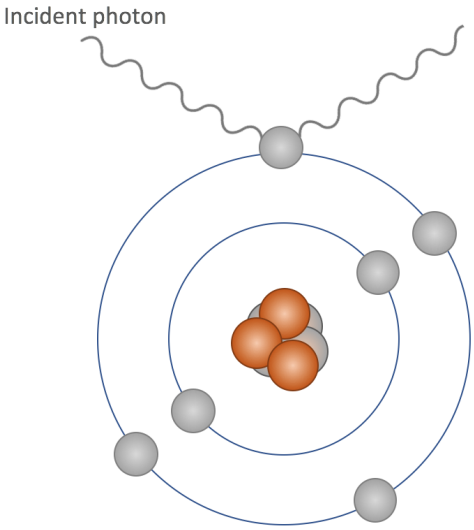

Figure 2.4.: Elastic scattering takes place between the incident photon and an electron in the absorbing material.

Several x-ray phase-contrast and dark-field imaging methods exist. Among them are crystal interferometer based phase-contrast, diffraction-enhanced imaging and propagation-based phase-contrast. Most of these methods are limited to synchrotron setups, requiring monochromatic and highly coherent x-ray illumination as well as a small field of view [Sni95; BH65; FGZ80].

Grating-based x-ray interferometry, is a recently developed method that offers the advantage of using the conventional polychromatic laboratory x-ray sources without the necessity of a monochromator, enabling the use of relatively high flux and short exposure times as well as the capability of acquiring absorption, phase-contrast and dark-field signals simultaneously in the same measurement [Pfe06a; Mom03; Pfe08b; Bec10; Pel14a]. Despite certain problems such as phase wrapping, x-ray phase-contrast based imaging methods have since become quite popular, particularly due to their improved soft-tissue contrast, and several research studies currently investigating their applications.

Dark-field imaging techniques have recently become quite popular in several fields due to their promising results for medical applications, such as the diagnosis of pulmonary emphysema in lungs, providing better resolution of small, calcified tumor nodules in breast scanning [Gra15; Yar13; And05; Sid11], the visualization of the orientation of bone micro-architecture without requiring high resolution detectors [Pot12], x-ray imaging using microbubbles as a scattering contrast [Vel13], reconstruction of tiny dentinal tubules [Vog15], and also in material science applications, for example to acquire quantitative information on the form and structure factor of materials [Pra15] and investigation of the fiber orientation of injection moulded polymers [Han15; Rev11].

Grating-based x-ray interferometry is one of the techniques used to exploit x-ray dark-field contrast images [Mom03; Con12]. This technique, offers the advantage of using a conventional polychromatic laboratory x-ray source without the necessity of a monochromator, enabling the use of relatively high flux and short exposure times as well as the capability of acquiring absorption , phase-contrast and dark-field signals simultaneously in the same measurement [Pfe06a; Mom03; Pfe08b]. More discussions of

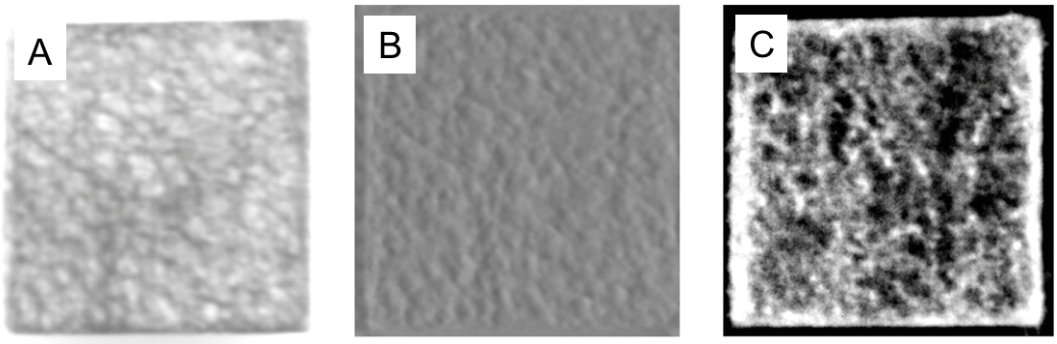

Figure 2.5.: Three different x-ray contrast projections of a femur sample, (A) Absorption contrast shows the attenuated parts of the sample, (B) Phase contrast which visualizes its phase-shifting properties, and (C) Dark-field contrast which is sensitive to scattering structures.

grating based imaging can be followed in chapter 6.

Figure 2.5 shows three different contrast projections of a femur bone sample measured within a grating-based x-ray interferometry setup.

Recently, new applications have been developed using grating-based x-ray interferometry to utilize acquired dark-field contrast measurements and to three-dimensional reconstruction of volumetric samples. Among them is X-ray Tensor Tomography (XTT), which is a novel dark-field imaging modality for three-dimensional reconstruction of x-ray scattering tensors from dark-field projections obtained in a grating interferometry setup. Similar to other novel imaging modalities, several challenges related to XTT measurement, data models and images' quality needs to be addressed. One of the main issues in XTT imaging modality, is that two-dimensional dark-field images measured in XTT are degraded by noise effects, such as detector readout noise and insufficient photon statistics, which is consequently affecting the reconstructed three-dimensional volumes to show noise artifacts.

3. Computed Tomography

In this section, we first introduce a brief history of computed tomography in section 3.1. Next, we will introduce a theoretical concept of computed tomography imaging in section 3.2 and finally will explain the tomographic reconstruction algorithms in section 4.1.

3.1 Background

Computed tomography (CT) is one of the well-established x-ray imaging modalities with wide spread applications from medical diagnosis to industrial non-destructive testing [Kal06]. CT technology has seen remarkable innovations in the past decades which have improved the performance of this modality in diagnosis and steadily increased its clinical indications. The first successful practical implementation of the theory was achieved in 1972 by Sir Godfrey Newbold Hounsfield [AH73], who played a vital role in the development of CT by conducting several experiments based on the mathematical theories of Allan McLeod Cormack in 1964 [Cor63]. They received a Nobel Prize for their contributions in the development of CT, and Hounsfield's name was selected to be as a standard measurement unit for recorded x-ray attenuation.

3.2 Theory

A CT scanner combines a series of two-dimensional x-ray projections taken from different angles and uses computer processing to create three-dimensional images, or slices, of a medical sample like bones, blood vessels and soft tissues inside the human body or some industrial materials.

Due to the three-dimensional nature of CT scans, this modality provides more detailed information in comparison to a single x-ray image acquisition. In fact, conventional CT scanners are developed to acquire the absorption contrast projections. Due to this reason, CT imaging is one of the mostly used modalities for imaging of hard tissues like bones rather than softer tissues. However, recent advances in x-ray imaging modalities such as contrast enhanced imaging and introduction of phase and dark-field contrast imaging methods have proved a potential for precise measuring and visualizing of softer tissues like hepatic tumors, brain tissue and long nodules.

3.3 Applications

Owing to the recent advancements in mechanics, electronics and computing power, the CT scanning time has been reduced, resultant images have a better quality and readability which helps CT scanners to be chosen as a good non-invasive imaging technology for clinical and non-clinical studies.

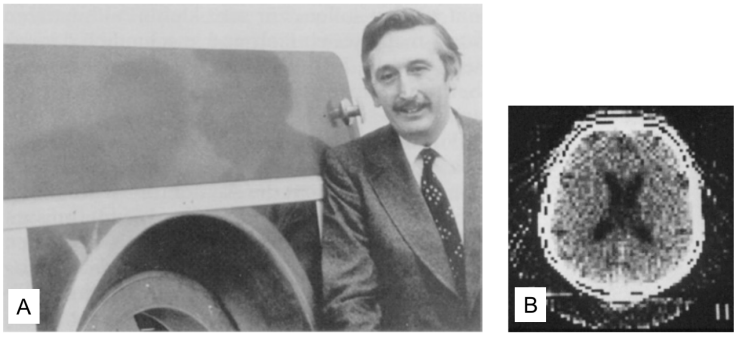

Figure 3.1.: (A) Godfrey Newbold Hounsfield developed the first CT scanner, and (B) Transverse slice imaging of the brain at low resolution with 80×80 pixels became the standard CT application in the 1970s [Kal06].

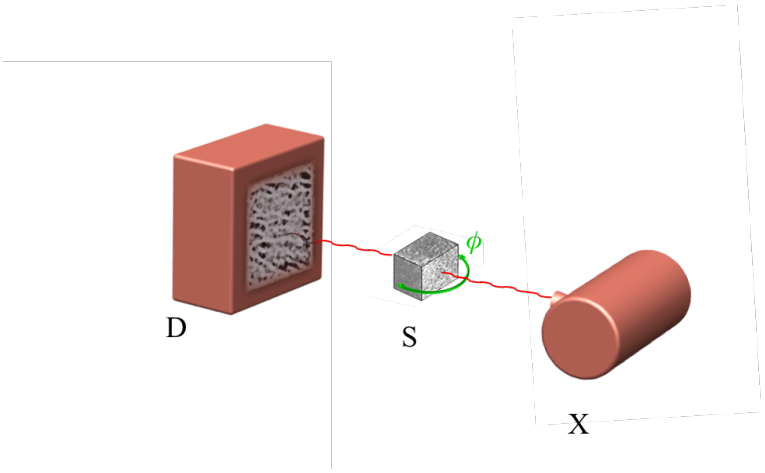

Figure 3.2.: Illustration of a typical x-ray absorption tomography setup including an x-ray tube (X), sample (S) with one degree of freedom (rotation angle ϕ), and x-ray detector (D).

3.3.1 Clinical Applications

CT enables direct imaging and differentiation of soft and hard tissue structures in abdomen, head and chest such as liver, lung tissue, fat, bone etc. It is especially useful in detecting for presence, size, spatial location, texture and extent of different types of abnormalities such as lesions, tumors and metastasis within body organs.

3.3.1.1 Abdomen

The abdomen contains several organs of the gastrointestinal, urinary, endocrine, and reproductive systems including liver, kidneys, pancreas, spleen, GI tract, and the area around these organs. A CT scan of the abdomen may be performed to assess the abdominal organs for lesions, injuries, or other abnormalities and also to investigate the effects of treatments on tumors [Hsi09]. Applying CT to hepatic imaging reveals promising results in detection and characterizing of liver masses and hepatic tumors. Several studies have been conducted to investigate the applicability of CT perfusion imaging for detecting and analyzing of hepatocellular carcinoma (HCC), which is known

as an epithelial tumor originating in the liver and composed of cells with characteristics similar to those of normal hepatocytes [Rod01]. A CT scan of the kidney may be performed to assess for tumors and other lesions, obstructions such as kidney stones and abscesses[Ryd00].

3.3.1.2 Bone

CT scans are frequently performed to evaluate the bones, and joints for damage, lesions, fractures, or other abnormalities, particularly when another type of examination, such as X-rays or physical examination are not conclusive.

CT imaging of the bone is used to image the temporal anatomy as a useful map for diagnosing pathologic disorders such as inflammatory and neoplastic processes and identifying pertinent positives and negatives [JGM13]. High resolution CT scans could be also utilized to study and diagnosis of osteoporosis based on the measurement of bone mineral density (BMD) [Kan05].

3.3.1.3 Head

CT scans of the head can provide detailed information about head injuries, severe headaches, dizziness, stroke and brain tumors. One of the major advances in modern neuroimaging applications was the use of the contrast enhanced CT approach, which enabled the accurate anatomic localization of brain lesions. A CT scan of the brain may also be utilized to investigate the results of a treatment on brain tumors and to detect abnormalities in the brain responsible for strokes. CT perfusion of the brain is also used to analyze the blood flow in the brain which shows the areas of the brain that are adequately supplied or perfused with blood and provides information on delivery of blood to the brain [Cas14].

3.3.1.4 Chest

CT scans are frequently performed to detection of abnormalities and to help diagnosis of unexplained cough, shortness of breath, chest pain, or fever. Lung nodules are detected very commonly on CT scans of the chest, and the ability to detect very small nodules improves with each new generation of CT scanner [Awa04].

Several worldwide large-scale clinical lung cancer screening trials are being conducted using the low-dose CT (LDCT) examinations, investigating whether early detection of lung cancer in high-risk individuals will eventually reduce lung cancer. In lung cancer screening, individuals who have a high risk of developing lung cancer but no signs or symptoms of the disease are being imaged using LDCT scanning of the chest [DWH03] to find related disorders and diseases before symptoms begin.

3.3.2 Non-clinical Applications

Industrial CT is an emerging laboratory-based non-destructive testing technique that is used in several applications for inspecting the industrial samples, machine parts and manufactured devices. Usually, μCT scanners are used for industrial non-destructive testing due to their superior resolution compared to medical CT scanners [PRG16]. Its use is also widely found in academic research, with several research and applications in food

science [Sch16], material science [MW14] as well as in geoscience applications [CB13]. Recently, CT imaging has successfully entered the field of coordinate metrology as a flexible measurement technique for performing dimensional measurements on industrial parts [War16].

3.4 Artifacts in CT

Artifacts can seriously degrade the quality of images in computed tomography scans, which could make them diagnostically unusable. To improve image quality, it is essential to understand why artifacts occur and how they can be corrected or removed.

CT artifacts originate due to the range of reasons. Physics-based artifacts occur due to the physical processes in the acquisition process of images. Patient related artifacts are happening due to the several factors associated with patient movement or the presence of metal part in or on the patient body. Scanner related artifacts result from issues in scanner functioning parts. However, in most of the cases, careful patient positioning and precise selection of scanner parameters are the most vital factors to prevent CT artifacts [Hsi09; BK04].

Noise, is one of the most commonly encountered artifact in CT images as a result of the statistical error of reduced photon counts, which results in several bright and dark streaks appearing along the direction of greatest attenuation [Hsi09]. Several iterative reconstruction techniques associated with regularization and noise reduction methods have been proposed to reduce the effect of this artifact [Nak05]. We will discuss more about this artifact and several pipelines including denoising methods and reconstruction techniques to prevent reduced image quality in the next chapters (see part I,chapter 11).

Beam hardening and scattering are two other commonly existing types of artifacts that produce dark streaks in the CT images. Iterative reconstruction and several post-processing approaches methods have been proposed to reduce the effect of this class of artifacts [Van11; BF12; WFV00]. Its also proved that, dual energy CT imaging can reduce the effects of beam hardening artifact by scanning the target with two different energies. The acquired information can be used to derive virtual monochromatic images that do not suffer from beam hardening effects [AM76].

Metal artifacts are another commonly seen artifacts that occur due to the existence of high density objects such as metal prostheses, surgical clips, or dental fillings which could generate streak-like lines in CT images [De 99; De 00]. Several techniques have been proposed to address the metal artifact reduction. Among them are iterative metal deletion technique [BF11], or a technique to determine the implant boundaries semi-automatically and to replace the missing projection data by linear interpolation [KHE87].

Recently, Stayman et. al. [Sta12] proposed a Known-Component reconstruction method to reduce the artifacts such as noise and streaking due to the existing of metal implants that degrade the image quality. This method is integrating the already known shape and material information of an object into the reconstruction problem benefiting a registration step for the known component [Xu17; Zha17].

4. Tomographic Reconstruction

While advances in CT hardware technology continue to overcome its physical limitations, recent updates in computing power have opened additional doors for improving the performance of CT imaging via more advanced processing methods, such as tomographic reconstruction techniques.

Mathematically, computed tomography can be assumed as an inverse problem, since it recovers the attenuation coefficients of a measured sample from a set of transmission values. As shown in Figure 3.2, rotation of a sample results in several number of coefficients of the two-dimensional Fourier transform for each sample slice. Tomographic reconstruction seeks to estimate a specific system from a finite number of projections. The mathematical fundamentals for tomographic imaging was described by Johann Radon [Rad86].

As shown in Figure 4.1, the projection of an object is a set of line integrals acquired during the measurement process at an arbitrary given angle such as θ.

Assuming the data collection process as a series of parallel rays, at position, across a projection at angle θ, the computed tomography problem can be given according to the Beer-Lambert law [Buz08], which describes the absorption of x-rays as,

$$I = I_0 e^{-\int \mu(x,y)ds}, \tag{4.1}$$

where $\mu(x, y)$ refers to the attenuation coefficient which is specific to each material and I and I_0 denote the transmitted and incident intensities respectively.

In theory, the inverse Radon transformation would yield the original image. Fourier slice theorem states that the values along the one-dimensional Fourier transform of a parallel projection of an object's slice are equal to those along a line parallel to the detector through the center of the slice's two-dimensional Fourier transform. In other words, if we had an infinite number of one-dimensional projections of an object taken at an infinite number of angles, we could perfectly reconstruct the original object, $f(x, y)$. However, in practical applications, there exist a finite number of projections available.

Figure 4.2 shows a visual illustration of the Fourier slice theorem.

4.1 Reconstruction Algorithms

Image reconstruction in CT imaging is a mathematical process that generates tomographic images from x-ray projection data acquired at many different angles around the patient and has fundamental impacts on image quality, radiation dose and therefore on diagnosis process.

Image reconstruction algorithms play a critical role in the quality and appearance of tomographic images. These methods are divided into two major categories, analytical reconstruction methods and iterative reconstruction (IR) techniques. Although iterative

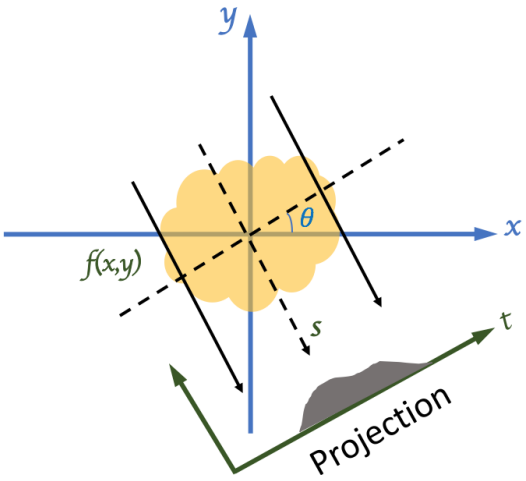

Figure 4.1.: Sketch of a tomographic measurement at a given angle θ.

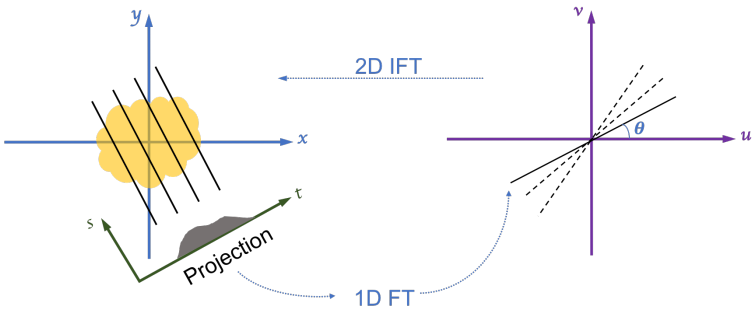

Figure 4.2.: Illustration of the Fourier slice theorem: one-dimensional Fourier transform (1D FT) of a projection taken at angle θ equals the central radial slice at angle θ of the two-dimensional Fourier transform (2D FT) of the original object.

image reconstruction algorithms were used to generate images with the very first commercial clinical CT scanner and underwent substantial improvements in the 1980s, especially in the context of emission tomography, analytical algorithms were used for CT image reconstruction due to their faster image reconstruction and ease of implementation [SV82; Sin10; L84a].

4.2 Analytical Reconstruction Methods

Analytical methods are a commonly used category of image reconstruction techniques for CT imaging modality. The most commonly used analytical reconstruction methods on commercial CT scanners are all in the form of filtered back-projection (FBP), which uses a one-dimensional filter on the projection data before back-projecting (two- or three-dimensional) the data onto the image space [Gey15; Oli11; FDK84].

As already mentioned, the reconstruction process is the solution of the resulting integral equations by inversion which is also called back projection process. In other words, back projection describes the propagation of the measured projections into the image domain and is also combined with applying of a filter such as Ram-Lak filter.

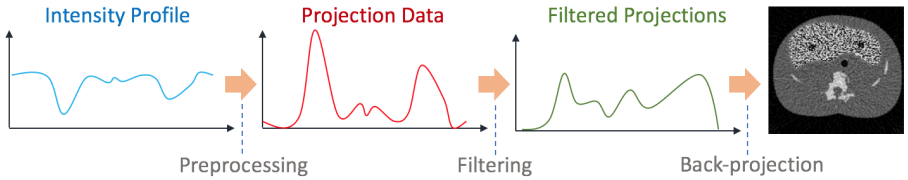

Figure 4.3.: A simplified schematic of CT data reconstruction in the context of analytic reconstruction technique: FBP.

In clinical practice, different variations of the filter (kernels) can be chosen [Gen02] depending on the target that is being imaged. Figure 4.3 displays a simplified pipeline of CT data reconstruction in the context of FBP.

Several limitations reduce the performance of analytical reconstruction methods for practical medical and industrial scenarios. These methods generally ignore associated noise of measurements in the problem and tries to reduce this artifact's effect by post-filtering operations. Also, it is usually assumed that the measurements are done continuously and integral solutions are being applied [Fes].

4.3 Iterative Reconstruction Techniques

Iterative reconstruction (IR) refers to a category of algorithms used in CT imaging that begin with an image assumption, and compares it to the real time measured values while making constant adjustments until these two are in agreement'[Her09; Hu99].

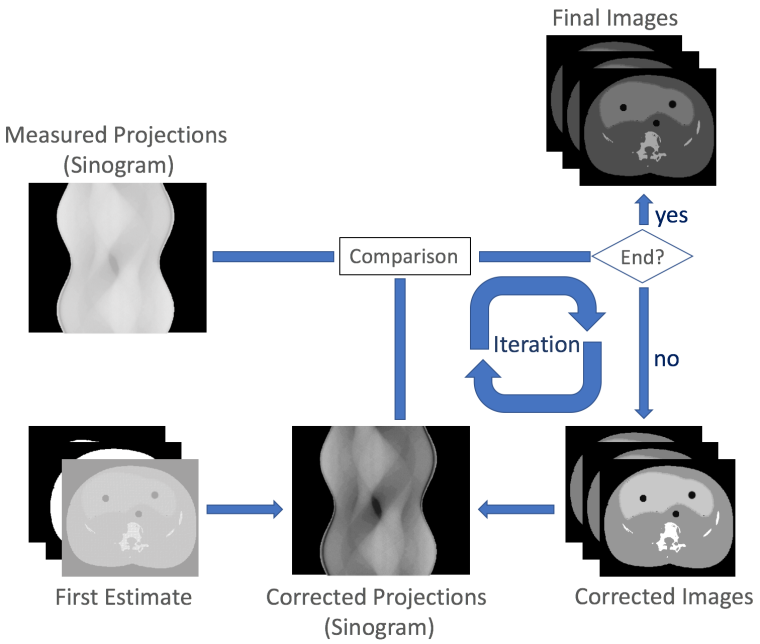

Figure 4.4.: A simplified schematic for principle steps of iterative reconstruction techniques for CT data.

Due to the recent advances in computing power, IR algorithms have become a clinically viable option in CT imaging scenarios. The principle of iterative image algorithms

is illustrated in Figure 4.4 in several steps. As shown in this figure, following a CT acquisition process to measure projections, a first image estimation is generated. An x-ray beam is simulated via forward projection to obtain simulated projection data, which are then compared with the measured projection data. In case of difference, the first image estimation will be updated based on the features of the underlying method.

This correction of image and projection data will be repeated to reach to a condition predefined by the algorithm and then final image will be generated [Fes00; Fes].

Due to the major difference in data handling in FBP and IR methods, reconstructed images from IR may have a different appearance (e.g., noise texture) from those using FBP approach. Its also known that the spatial resolution in a local region of IR images is highly dependent on the contrast and noise of the surrounding structures due to the non-linear regularization term and other factors during the optimization process [FR96].

4.3.1 Algebraic Reconstruction Technique (ART)

The algebraic reconstruction technique (ART) was the first widely used iterative approach with a long history and rich literature. It was first introduced by Kaczmarz in 1937 [Kac37] and was independently used by Gordon et al. [GBH70] in image reconstruction. ART is a reconstruction algorithm that uses a set of projections to reconstruct the desired object.

Assuming the original linear problem $AX = Y$, we can write,

$$\sum_{j=1}^{N} a_{ij} x_j = y_i, \quad s.t. \quad i = 1, 2, ..., M \quad and \quad j = 1, 2, ..., N, \tag{4.2}$$

where a_{ij} is the weighting parameter which denotes the influence of ith cell on the jth line integral, x_j is the constant intensity value of the jth cell, N refers to the total number of cells, and M refers to the total number of rays.

The implementation procedure starts with an initial guess, $x^{(0)}$ at the solution, and continues by projecting $x^{(0)}$ onto the first plane giving $x^{(1)}$. his process is updated so on and can be formulated as projection of $x^{(i-1)}$ on the ith plane which yields $x^{(i)}$ as,

$$x_j^{k+1} = x_j^k + \frac{(y_i - \sum_{m=1}^{N} a_{im}.x_m^{(k)})}{\sum_{m=1}^{N} a_{im}^2}.a_{ij}, \quad s.t. \quad i = 1, 2, ..., M \quad and \quad j = 1, 2, ..., N, \tag{4.3}$$

Updating process of Equation 4.3 continues until all the projections are considered and all the pixel values converge to a solution [Gor74].

Figure 4.5 illustrates a visual flowchart of algebraic reconstruction technique.

4.3.2 Simultaneous Iterative Reconstruction Technique (SIRT)

Simultaneous Iterative Reconstruction Technique (SIRT) is an improved version of the original ART approach with several major alterations to evaluate only one correction term for each grid cell and to consider all observations. The correction term is therefore independent of the order of the constant vector. Update term for SIRT is given by [KS88],

$$x_j^{k+1} = x_j^k + \sum_{i=1}^{M} \lambda a_{ij} \frac{y_i - \sum_{j=1}^{N} a_{ij}.x_j^{(k)}}{\sum_{i=1}^{N} a_{ij}}, \quad s.t. \quad i = 1, 2, ..., M \quad and \quad j = 1, 2, ..., N, \tag{4.4}$$

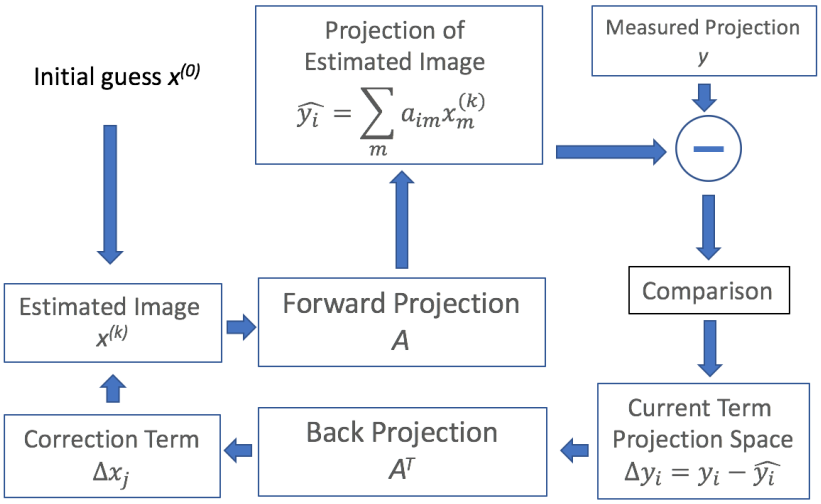

Figure 4.5.: Flowchart of algebraic reconstruction technique.

where a_{ij} refers to the weighting parameter which denotes the influence of ith cell on the jth line integral, x_j is the constant intensity value of the jth cell, N is the total number of cells, M is the total number of rays and y_i refers to the measured data whereas λ denotes the relaxation parameter.

SIRT approach requires several iterations to converge to a solution. A criteria could be defined to be small in number, which controls the number of iterations. Another possible approach would be to define a criterion such as $|y_i - \sum_{j=1}^{N} a_{ij}.x_j^{(k)}| < \epsilon$, where ϵ has a small value.

4.3.3 Simultaneous Algebraic Reconstruction Technique (SART)

In 1984, the simultaneous algebraic reconstruction technique (SART) was introduced with major changes in the standard ART approach. SART had a major impact in CT imaging scenarios with limited projection data. It generates a good reconstruction in just one iteration and illustrates superior performance comparing to the original ART approach. SART formulation described by Andersen and Kak [KS88], is given by,

$$x_j^{k+1} = x_j^k + \frac{\lambda}{\sum_i a_{ij}} \sum_{i=1}^{M} \frac{a_{ij}.(y_i - \sum_{m=1}^{N} a_{im}.x_m^{(k)})}{\sum_{m=1}^{N} a_{im}}, \quad s.t. \quad i = 1, 2, ..., M \quad and \quad j = 1, 2, ..., N, \tag{4.5}$$

where λ refers to the relaxation parameter. Larger values of λ may speed up convergence, however, with larger values, too much weight will be assigned to the last projection, which prevents convergence. Smaller values will cause the slower convergence, which is not feasible for real-time applications with larger images.

4.3.4 Conjugate Gradient (CG)

There are some additional approaches for iteratively solving linear systems in mathematics. The conjugate gradients (CG) method is a widely used iterative algorithm for the numerical solution of large sparse systems that have a symmetric matrix and are positive

definite. CG approach was first proposed by Hestenes and Stiefel [HS52; Sti52] in 1952 and has become a well-known method for its rapid convergence in several application areas [VV86].

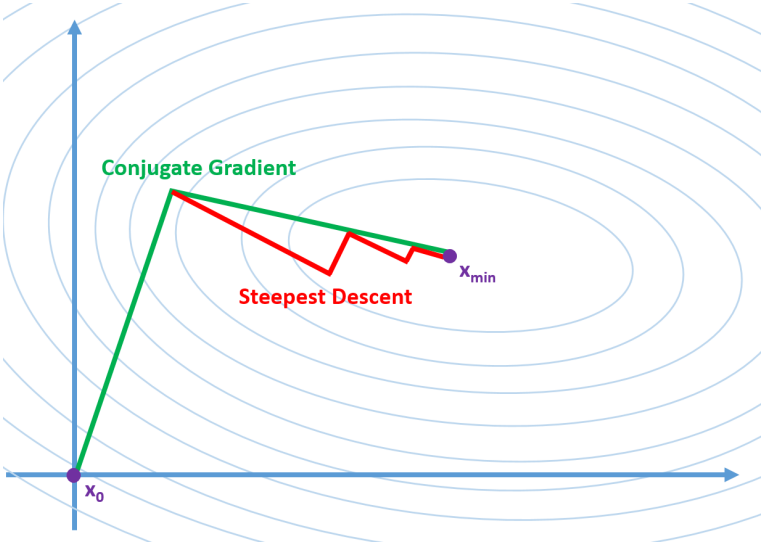

Figure 4.6.: A schematic quadratic form for a normal equation (symmetric, positive-definite) will have a shape similar to a bowl. To search Searching for the minimum c using steepest descent approach to search for an x_{min} starting from an initial guess (x_0) is shown in blue. However, the conjugate gradient method which is utilizing an optimal scheme to find the minimum quickly is marked in orange. This figure is adapted from [Vog15].

Considering the least-square problem as,

$$\arg\min_x \{\frac{1}{2}\|Ax - y\|_2^2\} \tag{4.6}$$

where A refers to the system matrix and y denotes the values measured in a particular experiment, a solution can be found using the normal equation,

$$A^T Ax = A^T y, \tag{4.7}$$

from which the auxiliary variables could be defined as,

$$B := A^T A, \tag{4.8}$$

and,

$$k := A^T, \tag{4.9}$$

where B is square, symmetric and positive-definite. Then, we can define the quadratic form as,

$$g(x) = \frac{1}{2}x^T Bx - k^T x. \tag{4.10}$$

Assuming the properties in B, as shown in Figure 4.6, function g will illustrate a bowl shape around the minimum where the gradient is zero ($\bigtriangledown g(x) = 0$) and will be

computed as,

$$\bigtriangledown g(x) = Bx - k, \tag{4.11}$$

which is simply describing the idea of relaxation approach. A vector$x$ which is solving a linear system $Bx = k$, will also minimize the quadratic form of $g(x)$.

Assuming this relation, rather than solving the normal equation $A^T Acx = Bx = k = A^T y$, it will be possible to to search for a minimum of the quadratic form $g(x)$ while computing a least-squares image reconstruction. since the minimization problem is non-linear, steepest descent (gradient descent) would be one possible method to solve it [FP63].

A simplified pseudo-code of CG approach is illustrated in 2. However, the concept of CG is to restrict number of search directions, and to take the optimal step size such that a second search along the same direction is superfluous (see Figure 4.6).

CG approach, is initialized with an arbitrary location (x_0), and evaluates the gradient to obtain a search direction. Then, a new estimate will be computed by moving along this search line to a close point to the solution with respect to the concept of B-orthogonality as described in [AMS90; FR64]. One of the most important aspects in CG is the fact that there is an upper bound on the number of iterations, such that CG is guaranteed to find the optimal solution of the least-squares problem in as many steps as there are dimensions, utilizing the mutually B-orthogonal search directions combined with optimal step lengths [GKR85].

A detailed overview of CG, its applications and generalizations to indefinite or non-symmetric matrices, can be found in [Saa03].

4.3.5 Maximum Likelihood Expectation Maximization (MLEM)

The methods introduced so far are assuming well-posed problem with some good measurements and none of them model the statistical properties of the measurement process.

Likelihood based approaches are another category of methods for photon-limited conditions that are the standard since decades, in order to support low dose imaging.

The problem of image reconstruction can be formulated as a standard statistical estimation problem. This leads to the following multiplicative update equation:

$$x_j^{k+1} = x_j^k + \frac{1}{\sum_i a_{ij}} \sum_i \frac{y_i}{a_i^T x^{(k-1)}}, \quad s.t. \quad i = 1, 2, ..., M \quad and \quad j = 1, 2, ..., N, \tag{4.12}$$

where the variable k refers to the iteration index.

As shown in Equation 4.19, MLEM approach is iteratively maximizing a likelihood function which has several advantages over the conventional FBP techniques. These advantages could be summarized as (1) MLEM methods do not require equally spaced projection data, (2) they can be utilized for limited set of projection data, and (3) they yields less artifacts [VSK85; L84a].

4.3.6 Penalized Likelihood (PL)

Penalized likelihood (PL) estimation is a way to consider the complexity of a model while estimating parameters of different models. In general, instead of applying a simple MLE,

Algorithm 1 Conjugate Gradient algorithm adapted from [She94]

Inputs: $B \in \mathbb{R}^{N \times N}$: a symmetric positive-definite matrix and $y \in \mathbb{R}^N$, initial guess $x^{[0]} \in \mathbb{R}^N$,

Outputs: Minimizer $x \in \mathbb{R}^N$ of the quadric problem, $g(x) = \frac{1}{2}x^T Bx - k^T x$.

$r := y - By$
$d := r$
$\delta_{new} := r^T r$
$\delta_0 := \delta_{new}$
for $it = 0, 1, 2, ...$ and $\delta_{new}/\delta_0\, \epsilon^2$ **do**
  $q := Bd$
  $\alpha := \frac{\delta_{new}}{d^T q}$
  $x := x + \alpha d$
  if $it \ \ mod \ \ NumOfIters == 0$ **then**
    $r := b - Bx$
  else
    $r := r - \alpha q$
  end if
  $\delta_{old} := \delta_{new}$
  $\delta_{new} := r^T r$
  $\beta := \frac{\delta_{new}}{\delta_{old}}$
  $d := r + \beta d$
end for

the log-likelihood minus a penalty term will be maximized, which is depending on the model and most often increasing with number of parameters [Fes00].

The objective function of PL reconstruction can be written as,

$$\phi(x; y) = -L(x; y) + \beta \|\psi_x\|, \tag{4.13}$$

where L represents the log-likelihood function which is derived using the Poisson likelihood assumption and a data model matching. The second term is a traditional edge-preserving roughness penalty term. The operator ψ denotes a local pairwise voxel difference operator. The regularization parameter controls the balance between the data fidelity and roughness penalty allowing user control of the noise-resolution trade-off. The optimization problem can be written as,

$$x_\Delta = \underset{x \in \mathbb{R}^{N_x}}{\operatorname{argmin}}\, \phi(x; y). \tag{4.14}$$

This objective can be solved in an iterative manner, using different approaches such as separable quadratic surrogates method [EF99a]. (more details on separable quadratic surrogate methods in subsection 4.3.8)

4.3.7 Prior Image Registered Penalized Likelihood Estimation (PIRPLE)

Prior Image Registered Penalized Likelihood Estimation (PIRPLE) approach was recently introduced by [Sta13] as a model-based approach which integrates both a (Poisson) noise model and prior images in the reconstruction process and poses the problem as a joint registration and reconstruction.

The objective function of PIRPLE includes a joint formula for the registration and reconstruction as follows,

$$\phi(x;y) = -L(x;y) + \beta_R \|\psi_R x\| + \beta_P \|\psi_P(x - W(\lambda)x_P)\|, \tag{4.15}$$

where W refers to a transformation operator parameterized by the vector λ. Details of the PIRPLE, its registration step and operators can be found in [Sta13].

Algorithm 2 Algorithm for iterative solution of the Prior Image Registered Penalized Likelihood Estimation adapted from [Sta13]

Inputs: initial guess x^0, initial guess of registration parameters λ_0^0 and initial guess for inverse Hessian H_0^0,
Outputs: solution of the PIRPLE objective as stated in Equation 4.15.

for $it = 0, 1, 2, ..., NumOfIters - 1$ **do**
  // Registration Step
  for $r = 1, 2, ..., R$ **do**
    Compute $\nabla_\lambda \Theta(\lambda_{r-1}^{[n]}, x_0^{[n]})$
    BFGS [L84b] update based on $\{\nabla_\lambda \Theta(\lambda_{r-1}^{[n]}), H_{r-1}^{[n]}\}$
    $\hat{\phi} := linesearch in \lambda_{r-1}^{[n]} + \phi H_r^{[n]} \nabla_\lambda \Theta(\lambda_{r-1}^{[n]})$
  end for
  $\lambda_0^{[n+1]} := \lambda_R^{[n]}$
  $H_0^{[n+1]} := H_R^{[n]}$
  // Image Update Step [Sta13]
  for $j = 1, 2, ..., NumberOfVoxels$ **do**
    $x_j^{[n+1]} := x_j^{[n]} + \Delta x_j^{[n]}$
  end for
end for

4.3.8 Separable Paraboloid Surrogates (SPS)

A different type of approaches are utilizing optimization transfer principle [De 93], together with paraboloid surrogates, to maximize the likelihood by locally fitting a simple paraboloid at the location of the current estimate. In 1999, Separable Paraboloid Surrogates (SPS) method, introduced by Erdogan and Fessler [EF99c], is the most commonly used approach. In this approach, the paraboloid curvature has been precomputed, and a relaxation scheme is usually utilized. An overview of SPS, and more details on its applications can be found in [Erd99; AF03].

4.4 Hybrid Algorithms

Hybrid algorithms combine both analytical and iterative methods using different arrangements. In one example, the initial image is generated by the use of analytical methods (e.g. FBP), and then iterative methods have been utilized in order to optimize several image domain characteristics, such as noise [Fun11]. In another example, an iterative algorithm can be directly used in the reconstruction process to focus on image improvements of an initial image estimate that is generated by an analytical method [VLR13; Wil13].

4.5 Image Regularization and Noise Reduction

Images can be improved by considering more constraints e.g. fitting the input data subject to a smooth shape. Mathematically, this can be expressed using Lagrange multipliers [La 97]. General regularised reconstruction can be written as,

$$\arg\min_x \{T(x) + \lambda V(x)\} \tag{4.16}$$

where $T(x)$ refers to the data fidelity term, $V(x)$ denotes a penalty function or regulariser and λ denotes the weight of the penalty term V, and thus its impact in comparison to the data fidelity term T. The latter is minimised if the additional constraint is met.

4.5.1 Tikhonov Regularisation

Tikhonov regularization, named in honor of Andrey Tikhonov, is the most commonly used method for regularization of ill-posed problems [Tik63]. The penalty can be written as,

$$V_{Tikhonov}(x) = \|Lx\|_2^2 \tag{4.17}$$

where L denotes the Tikhonov matrix and can be utilized based on the specific application, and an operator mapping the coefficients into the Fourier domain can be used to level the frequencies of the image.

4.5.2 Total Variation Regularization (TV)

Total Variation regularization (TV) is a most often used penalty in imaging and digital image processing, that has applications in noise removal. It is based on the principle that signals with excessive and possibly spurious detail have high total variation, that is, the integral of the absolute gradient of the signal is high. Considering two-dimensional signal x, such as images, the TV norm proposed by Rudin, Osher and Fatemi in 1992 [ROF92] is,

$$V(x) = \sum_{i,j} \sqrt{|x_{i+1,j} - x_{i,j}|^2 + |x_{i,j+1} - x_{i,j}|^2} \tag{4.18}$$

which is an isotropic and not differentiable. However, an anisotropic variation which could be also easier to minimize, is shown as,

$$V_{anisotropic}(x) = \sum_{i,j} |x_{i+1,j} - x_{i,j}|^2 + |x_{i,j+1} - x_{i,j}|^2 \tag{4.19}$$

TV has been extensively used as a denoising method in imaging applications [SP08; Sey18c; Sey13a; SY14a]. Assuming the signal x corrupted by additive white Gaussian noise,

$$y = x + n \quad x, y, n \in \mathbb{R} \tag{4.20}$$

Standard TV denoising problem can be expressed as,

$$min_x \|y - x\|_2^2 + \lambda V(x). \tag{4.21}$$

where λ refers to the regularization parameter, controlling how much smoothing is performed. Larger noise levels call for larger λ.

4.6 Compressed Sensing and Sparse Regularization

Compressed Sensing (CS) enables a potentially large reduction in the sampling and computation costs for sensing signals that have a sparse or compressible representations [EK12]. While the Nyquist-Shannon sampling theorem states that a certain minimum number of samples is required in order to perfectly capture an arbitrary signal, when the signal is sparse in a known basis we can vastly reduce the number of measurements that need to be stored. Consequently, when sensing sparse signals we might be able to do better than suggested by classical results. This is the fundamental idea behind CS: rather than first sampling at a high rate and then compressing the sampled data, we would like to find ways to directly sense the data in a compressed form.

In a recent work, Donoho, showed that a signal having a sparse representation can be recovered exactly from a small set of linear, nonadaptive measurements. This result suggests that it may be possible to sense sparse signals by taking far fewer measurements, hence the name compressed sensing [Don06].

There are some significant factors in original CS method to be considered such as (1) the image must be sparse, (2) reconstruction of the image must be done using a nonlinear method, and (3) the standard linear reconstruction method should generate incoherent view aliasing artifacts by applying the sparsifying transform [EK12],

$$min\|\psi x\|_1 \quad s.t. \quad AX = Y, \tag{4.22}$$

4.6.1 Prior Image Constrained Compressed Sensing (PICCS)

Prior image constrained compressed sensing (PICCS) method considers a high quality prior image x_p to reconstruct the image x from an undersampled data set by solving the following constrained minimization problem [CTL08a],

$$min_x \left[\alpha\|\psi_1(x - x_p)\|_1 + (1 - \alpha)\|\psi_2 x\|_1\right] \quad s.t. \quad AX = Y, \tag{4.23}$$

Here the sparsifying transforms, ψ_1 and ψ_2 refer to any transform and α denotes the regularization parameter.

4.6.2 Alternating Direction Method of Multipliers (ADMM)

Alternating Direction Method of Multipliers (ADMM) approach has been proposed by [Boy11], to solve a linear combination of two convex functionals via variable splitting. The approach is to use two distinct variables while doing the optimization, where the first one is the minimizing of least-squares data fidelity term and the second one is the sparsity constraint.

Considering the optimization problem with an assumption of both data and regularization terms being convex as,

$$\arg\min_x \{\frac{1}{2}\|Ax - y\|_2^2 + \lambda\|\mathcal{T}c\|_1\}, \tag{4.24}$$

where operator $\mathcal{T}$ can be defined as analysis operator, transforming the pixel coefficients into the coefficients of the respective basis or frame.

Equation 4.25 can be transfered into an equivalent constrained optimization problem using ADMM and decoupling data and regularization terms as below, [Boy11]

$$\arg\min_x \{\frac{1}{2}\|Ax - y\|_2^2 + \lambda\|z\|_1\}, \quad s.t. \quad \mathcal{T}x = z. \tag{4.25}$$

Considering the augmented Lagrangian L_p,

$$L_p(x, z, u) = \frac{1}{2}\|Ax - y\|_2^2 + \lambda\|z\|_1 + u^T(\mathcal{T}x - z) + \frac{\rho}{2}\|\mathcal{T}x - z\|_2^2, \tag{4.26}$$

where the chosen parameter ρ couples $\mathcal{T}x$ and z, and u refers to a Lagrange multiplier. In general, each iteration of ADMM has three distinct steps which involves two optimization problems and one pure update and can be solved as [Boy11],

$$(A^TA + \rho T^TT)x^{p+1} = A^Ty + \rho T^Tz^p + u^p, \tag{4.27}$$

where $\rho \in \mathbb{R}$ denotes the coupling parameter. Second, we perform,

$$z^{p+1} = S_{\lambda/\rho}(Tx^{p+1} + u^p), \tag{4.28}$$

where $S_{\lambda/\rho}$ denotes the soft-thresholding operator. As the third step, we finally perform the update,

$$u^{p+1} = u^p + Tx^{p+1} - z^{p+1}, \tag{4.29}$$

where the first part is a linear problem which can be solved using the methods like CG (see chapter 11), and the second step minimizes the ℓ_1-penalty on the variable z and the last step will be updating the Lagrange multiplier u [Wah12].

5. Four-Dimensional CT Imaging

Four-dimensional (4D) CT is an imaging technique to obtain and reconstruct multiple images of the same target over time. 4D CT increasingly offers potential advantages as an alternative primary investigation and is a common second-line investigation [Hsi09].

4D CT can provide precise anatomic information and can help differentiate healthy tissue and lesions. It includes image sets in three planes (axial, coronal, sagittal) and the fourth dimension could be the perfusion information derived from multiple contrast phases. It is most commonly performed with three phases: non-contrast, arterial, and delayed phase imaging [Hoa14].

5.1 CT Perfusion Imaging

CT perfusion (CTP) is a functional imaging modality that measures the tissue blood-flow parameters through sequential CT scanning of the same tissue or organ over the time. Typically, an iodinated contrast agent is administered and projection images are acquired before, during, and after injection of contrast to track temporal changes in CT attenuation. Several commercial software packages are available for calculating parametric maps like blood volume, blood flow and time to peak values. Most of the available packages however, are using similar mathematical models to quantitatively asses the perfusion parameters. Most of these models are based on the maximum slope method (SM) to calculate the perfusion parameters. The principle of the SM is quite simple which makes it very attractive for brain and liver perfusion evaluation tasks [MHD93a; MHD93b]. Some other methods employ a deconvolution of the arterial input function (AIF). Algebraic deconvolution approaches based on the singular value decomposition (SVD) are also used in some packages [Eas02; Ass16].

CT perfusion imaging has several application for visualization and investigation of abnormalities in brain and liver indications. CTP of the brain, is critical in characterizing the irreversibly infarcted brain tissue and the severely ischemic but potentially salvageable tissue [Kon09]. Liver CT perfusion provides valuable information on blood flow dynamics as a valuable measurement for hepatic fibrosis in patients with chronic liver disease and also in the evaluation of therapeutic effectiveness for liver cancer [KKW14; Qia10; Ass15].

5.2 Perfusion Analysis Techniques

Two basic functional CT paradigms are measured from the acquired data: perfusion measurements and permeability studies [Mil99].

Figure 5.1 illustrates a general perfusion analysis workflow. As shown in this figure, reconstructed CT volumes from different time points (left) are imported to the perfusion analysis to create the perfusion maps (right).

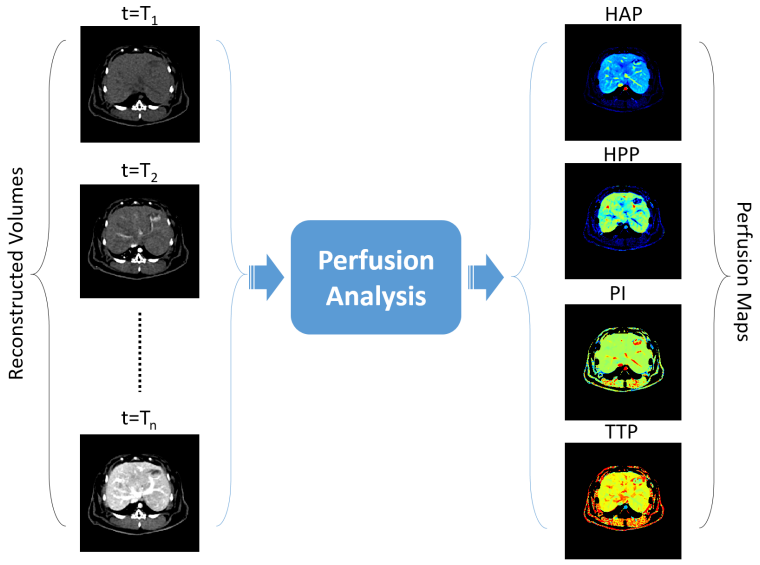

Figure 5.1.: Schematic illustration of the general perfusion analysis workflow. Reconstructed CT volumes from different time points (left) are imported to the perfusion analysis to create the perfusion maps (right). In this case, a liver images are used which gives hepatic arterial perfusion (HAP), hepatic portal perfusion (HPP), perfusion index (PI) and time-to-peak (TTP) maps. More details on these maps creation can be found in section 12.6.

The calculation of perfusion parameters is performed using several mathematical models including two commonly used approaches: Compartmental analysis and Deconvolution analysis [MG03a; MHD93a]. Therefore, the perfusion analysis block in Figure 5.1 can be replaced with any of these models.

5.2.1 Compartmental Analysis

Compartmental analysis approaches include two main categories of single and double compartment models [Mil12].

The single compartmental model is utilized to calculate the tissue perfusion considering the intra-vascular and extra-vascular spaces as a single compartment. It estimates the perfusion either from the maximal slope or the peak height of the same tissue concentration curve normalized to the arterial input function [MEK07].

The two compartmental model, however, has been utilized to evaluating of capillary permeability and blood volume [Mil02]. This model assumes the intra-vascular and extra-vascular spaces as separate compartments and measures perfusion parameters using a technique called Patlak analysis [MG03a].

More details and formulations for the compartment model and maximum slope method can be found in section 12.6.

5.2.2 Deconvolution Analysis

Perfusion analysis using the deconvolution approach is based on the arterial and tissue time attenuation curves (TAC) which have been utilized to calculate the impulse response

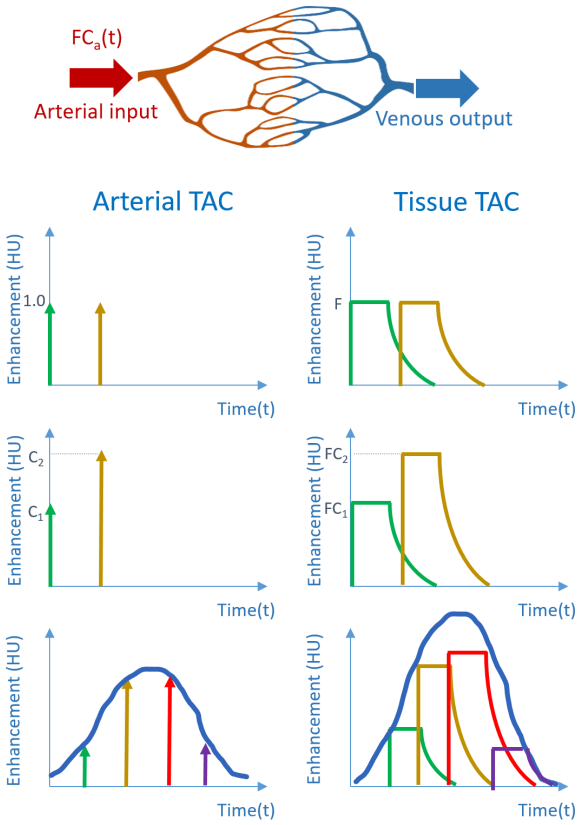

Figure 5.2.: The concept of convolution in CTP analysis (a) Schematic representation of the vascular structure in a tissue region. $FCa(t)$ refers to the input of contrast agent into the tissue, (b) when blood flow is not changed for two injections of the same concentration (left), then the tissue TAC for each injection will be the same; This is called IRF of the tissue. The right shows two IRF for the case of two identical bolus injections of contrast agent of the same concentration. For each IRF, initially, there is a sudden increase in the shape of the graph because the injection is directly into the arterial input. (c) Tissue TAC corresponding to a case in which the arterial TAC consists of two bolus injections of different concentrations C_1 and C_2, and, (d) shows a general arterial TAC as a series of injections equally spaced in time and of different concentrations (left). For each bolus injection, TAC of the tissue is a scaled IRF, which is the product of blood flow, concentration of bolus, and the IRF. The total tissue TAC in response to the general arterial concentration $Ca(t)$ is the sum of all the scaled IRF after they have been shifted in time in accordance to the times of their corresponding bolus injection. This figure is adapted from [Lee02].

function (IRF) for the tissue.

In general, if the IRF is known, the tissue TAC in response to a general arterial TAC, $C_a(t)$, can be calculated as a summation of scaled and time-shifted IRF's. The corresponding scale factors and time shifts are given by the rate of input of contrast agent into the tissue $FC_a(t)$ and t, respectively. This operation is called a convolution,

$$C_l(t) = C_a(t) \otimes FR(t), \tag{5.1}$$

where $\otimes$ denotes the convolution operator, $C_I(t)$ refers to the TAC obtained from tissue, and $FR(t)$ is the blood-flow scaled IRF [Lee02; Cue02].

A schematic overview of the convolution concept for CTP analysis is illustrated in Figure 5.2.

For the estimation of capillary permeability a distributed parameter model is used which consists of an extended deconvolution model [Mil12]. More details and formulations of this approach can be found in [Lee02]

6. Grating Based Imaging

Modern Grating-based imaging (GBI) is a recently introduced approach to phase contrast and dark-field imaging which includes conventional laboratory sources and is based on the use of a three-grating Talbot-Lau interferometer [Cla98; Pfe06b]. It has some similarities to the crystal interferometer [BH65] as it consists of a beam splitter and a beam analyzer, and is also similar to analyzer based imaging (ABI) [IB95] as it measures the first derivative of the phase front, and enables the dark-field imaging.

As shown in Figure 6.1, an ordinary setup of x-ray tube (X), specimen (S) and detector (D) has been extended by inserting a source grating ($G0$) after the tube, and two more gratings ($G1$, $G2$). The source grating $G0$ creates multiple sources with sufficiently high coherence to allow for a periodic interference behind the phase grating $G1$. Finally the analyzer grating $G2$ enables to measure the interference pattern with conventional x-ray detectors [Mom96].

Measurement process starts with several images that recorded while the relative lateral position of $G2$ is being shifted relatively to $G1$ which could be translated into the interference pattern that is too small to be measured directly with a conventional detector.

A periodic function for each detector pixel can be described as [Wei05],

$$I(x_g) \approx a_0 + a_1 cos(\phi + \frac{2\pi}{p_2} x_g) \tag{6.1}$$

where p_2 refers to the period in $G2$, x_g denotes the stepping and ϕ refers to the phase of the intensity curve.

As shown in Figure 6.2, from a scan I_s with a sample located in the setup and also a reference scan I_r without, multiple signals can be extracted. The different signals and their relation to the sample as well as the reference scan are illustrated in the same Figure.

These quantities are computed as [Pfe08b] described below. The absorption a is calculated by the ratio of the mean intensity as,

$$a = \frac{a_{0,s}}{a_{0,r}}. \tag{6.2}$$

Also the differential phase-contrast $\Delta\phi$ can be calculated as

$$\Delta\phi = \phi_s - \phi_r, \tag{6.3}$$

and dark-field signal V will be extracted as,

$$V = \frac{a_{1,s} a_{0,r}}{a_{0,s} a_{1,r}}. \tag{6.4}$$

where $a_{\Delta,s}$ and $a_{\Delta,r}$ refer to $a_{\cdot}$ as in Equation 6.1 respectively for I_s and Ir. The quotients of $a_{1,s}$ and $a_{0,s}$ refer to the visibility V_s, with the reference visibility V_r defined accordingly [Bec10]. More detailed information on grating based imaging concept can be found in [Bec09; Mom96; Pfe06a; Pfe08a; Wei05].

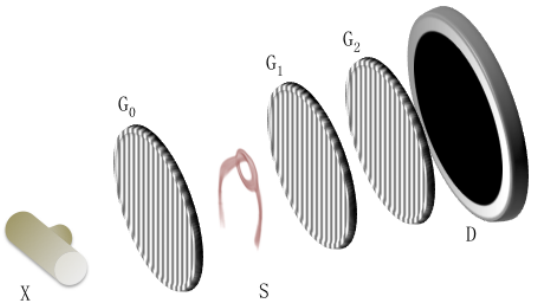

Figure 6.1.: Sketch of the Talbot-Lau X-ray Grating Based Interferometry setup.

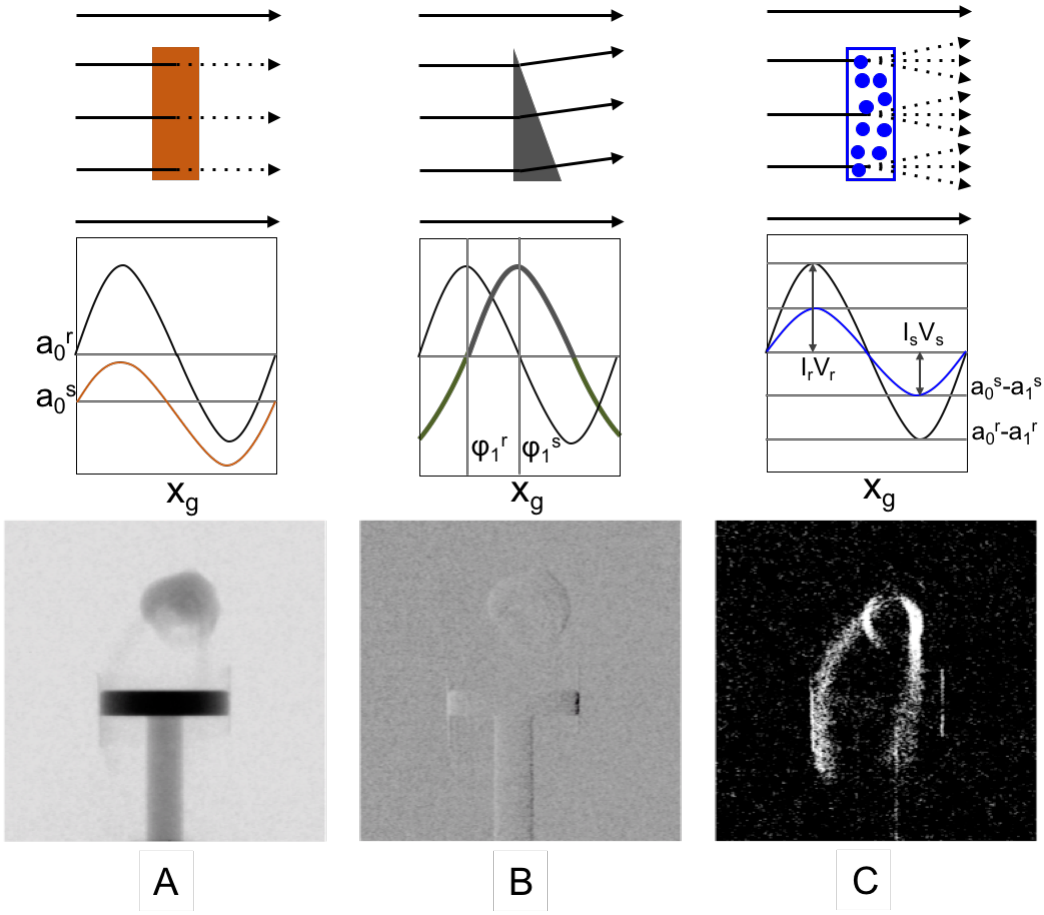

Figure 6.2.: Illustration of three signal components, (A) Absorption-contrast which is shoeing the attenuation of the x-ray beam leads to a reduction of the amplitude of the interference pattern. (B) Phase-contrast which is the refraction that causes a shift of the pattern, and (C) Dark-field contrast showing the scattering that reduces the amplitude of the interference pattern and creates an offset. This figure is adapted from [Sch13].

7. Other Imaging Modalities

In previous sections, We have discussed x-ray based imaging modalities and described CT imaging modality including its physics, theory, reconstruction techniques, limitations and challenges. However, several different types of medical imaging modalities are also being used for clinical and non-clinical applications.

Positron emission tomography (PET) is a nuclear imaging technology that enables the visualization of metabolic processes in the body. Another similar modality, Single-photon emission computed tomography (SPECT) is also using gamma rays and can provide three-dimensional information in the form of cross-sectional slice images of the patient. Some types of medical imaging modalities work without using ionizing radiation, for example magnetic resonance imaging (MRI) and ultrasound imaging, and have been utilized in diagnosis of several diseases.

In this section, we will briefly introduce some of these modalities by explaining their theory, structures and existing challenges.

7.1 Positron Emission Tomography (PET)

A PET scan is a type of nuclear medicine imaging modality which is used to image different tissues to identify some conditions by looking at blood flow, metabolism, and oxygen use [Bai05].

PET imaging modality construct three-dimensional images by detecting gamma rays emitted when certain Radioactive tracers (radiotracers) are injected into a patient's body. Radiotracers are absorbed by tissues with higher levels of metabolism (e.g., active tumors) than the rest of the body. Gamma rays are generated when a positron emitted from the radiotracer collides with an electron in tissue and results a pair of photons that emanate in opposite directions and are detected by detectors which are located around the patient. Unlike other anatomical imaging modalities such as CT and ultrasound, PET imaging provides functional information of the imaging target [ABP12; Ter83; Ass17].

PET scans have been utilized to diagnose several diseases including heart disease, brain tumors, stroke, cancer, head injuries, Parkinson's disease, and many other disorders. In neurology, PET has been used in a range of conditions, and in particular in severe focal epilepsy, where it may be used to compliment Magnetic Resonance Imaging [Gam02].

7.2 Single-photon Emission Computed Tomography (SPECT)

SPECT scanning is similar to PET, and is used to determine how organs inside the body work using the injection of a radioactive tracer; for the SPECT scan, the tracer will stay in the bloodstream [Hol10].

Similar to PET, the radiotracer starts emitting gamma rays, from the patient, which contrasts with the PET scans which emit positrons. Then, these rays are detected by the gamma camera that rotates through 360 degrees around the patient which enables the cross-sectional images to be assembled three-dimensionally similar to CT imaging. This enable the visualization of three-dimensional volumes or a series of two-dimensional images at the end [Kno83].

SPECT imaging has several different applications, which make this form of imaging convenient for the medical tests. Cardiac SPECT scans can be used to inspect the blood flow through the heart. SPECT scans can be also utilized to reveal hidden fractures in bone, such as shin splints and stress fractures because areas of bone healing usually light up on the scans. It could be also used to inspect the parts of the brain that are affected by various disorders including Dementia, Epilepsy and head injuries [HT90].

7.3 Magnetic Resonance Imaging (MRI)

Magnetic resonance imaging is a noninvasive imaging modality that allows for the visualization of both structural and functional information of the scanned human body.

In 1938, Isidor Isaac Rabi described the NMR phenomenon for the first time by developing a technique to measure the magnetic characteristics of atomic nucleus. Discovery of Rabi, facilitated the development of MRI for use in clinical problems [ABP12]. In 1971, Raymond Damadian used NMR in medical applications by measuring T1 and T2 relaxation times in rat tumors. Dr Damadian observed that a tumor tissue possessed longer T2 times than those of a normal tissue, a finding that was published in Science [Dam71]. The first images of humans scanned in an MR machine were produced in 1977 which is the crude images of the human thorax. In 1984, Michael Moseley established his work in diffusion imaging as a groundwork for fMRI techniques [WME84]. In the recent years, diffusion tensor imaging (DTI) and fMRI using blood oxygenation level-dependent (BOLD) techniques were also introduced [Mos90].

Today, an MRI scanner consists of a large, powerful magnet in which the target lies. Signals will be sent to the body using a radio wave antenna and then received back. Returned signals are then converted into images. MR imaging has several applications including imaging of organs of the chest and abdomen such as heart, liver, biliary tract, kidneys, spleen, bowel, pancreas, and adrenal glands. It is also used to visualize the pelvic organs including the bladder and the reproductive organs such as the uterus and ovaries in females and the prostate gland in males and also blood vessels [Le 92; ABP12].

7.4 Ultrasound

In Ultrasound imaging, also known as sonography, sound waves are used to be reflected by organs and other interior body parts in real-time for image producing. An ultrasound image is produced based on the reflection of these waves off of the imaging target structures. The amplitude of the signal and the signal traveling time through the object provide the information to produce the images. Ultrasound imaging has been used for several years and has an excellent safety record. Unlike x-ray based imaging modalities, there is no ionizing radiation exposure associated with ultrasound modality [Sza04; MRA14]. However, diagnostic ultrasound has been one of the active research areas for

last decade and several advancements have been reported in medical ultrasound imaging, elastography, ultrasound contrast agent imaging, super resolution imaging, and 2D array transducer [Lee17; SK17].

Ultrasound imaging has applications to evaluate the abnormalities in pregnancy, imaging of the heart and blood vessels and inspecting organs in the abdomen symptoms of pain [Shu15].

8. Structure of this Thesis

Subject of this thesis is the advanced reconstruction and noise reduction techniques in four- and six-dimensional x-ray imaging modalities. We study two major research topics organized in two main parts, including Part (I) to study the six-dimensional x-ray tensor tomography as a newly developed grating-based imaging modality which leverages the dark-field contrast projections to reconstruct volumes of medical and non-medical targets scanned. In this part, we will introduce XTT setup, theory and discuss the issues and limitations with using this modality for measuring of some medical and non-medical specimens. We particularly, focus on the data processing chain of XTT, including image reconstruction and also noise reduction of XTT data and introduce several evaluation methods to assess the acquired data using these techniques. In this part, we will investigate the best way to incorporate a denoising technique into the XTT reconstruction pipeline, in particular the popular total variation denoising technique. We will propose two different schemes of including denoising into the reconstruction process, one using a column block-parallel iterative scheme and one using a whole-system approach. Additionally, we will compare results using a simple denoising approach, applied either before or after reconstruction. Several experiments will be introduced and corresponding results will be illustrated visually and quantitatively for both medical and non-medical datasets.

Part (II) of this thesis, includes the low-dose CT perfusion imaging study of the liver and includes various advanced data processing, image reconstruction and analysis approaches. In this part, we will introduce CT perfusion which is a recently developed CT imaging technique with several demonstrated clinical and pre-clinical utility in the detection, staging, and analysis of treatment response for different applications such head and neck, liver, lung and colorectal imaging [Mil12]. CT perfusion has been successfully employed to assess the extent of salvageable tissue in acute stroke cases [SL05]. It has also been used in assessing tumor vascularity changes that result from chemotherapy and radiation therapy [Sah07]. CT perfusion of the liver can reveal hepatic diseases and that can be used to assess treatment responses [LMS15]. More widespread adoption of liver CTP in clinical trials to assess its potential as a biomarker as well as broader clinical use have been hampered by concerns over radiation exposure.

A variety of strategies have been proposed to limit radiation exposure including the individualization of scanning parameters, modification of tube current or voltage throughout the observation period. However, decreasing the x-ray radiation dose reduces CT image quality with increased noise and possible streak artifacts which lowers the clinical and diagnosis utility of the scan.

In this part, we address the low-dose CT perfusion imaging of the liver by designing a simulation study based on the real animal data. Finally, we adapt a novel data processing chains including reconstruction of difference [Pou16] to investigate the reduction of radiation dose level for CT perfusion studies.

we apply the RoD method to low-dose CTP data. The approach is investigated in

simulation studies using an anthropomorphic phantom with realistic time attenuation curves (TACs) for different tissue types. We analyze imaging performance in individual reconstructions in the imaging sequence from contrast injection, through uptake, and washout, and perform a perfusion analysis to compare several perfusion metrics including hepatic arterial perfusion, hepatic portal perfusion, hepatic perfusion index and time-to-peak metrics. The RoD approach is compared with traditional FBP and penalized-likelihood (MBIR) reconstructions.

Part II.

X-RAY TENSOR TOMOGRAPHY

9. Introduction to X-ray Tensor Tomography

9.1 Overview

In this chapter, we introduce X-ray Tensor Tomography (XTT), as a novel x-ray imaging modality used for reconstruction of three-dimensional x-ray scattering tensors from dark-field projections obtained in a grating-based interferometry setup. A detailed introduction on the background of XTT imaging modality and previous related studies will be discussed in section 9.2. An introduction of acquisition and forward model will follow in sections 9.3 and 9.4. Finally, in 9.5, we explain the existing reconstruction method for XTT imaging.

9.2 Background

Conventional x-ray imaging methods rely on the attenuation of x-rays when they pass through an object. Recently, grating interferometer based approaches [Mom03; Pfe06a] have been proposed to extract the scattering and refraction of x-rays by the scanned object in order to obtain phase and dark-field contrast. Dark-field contrast is a measurement of the ultra-small angle of x-rays deviating from their origin after interaction with sub-micron sized structures [Con12; Pel14b; Wan14]. The dark-field contrast obtained in a grating interferometry setup is an anisotropic signal, which means that the measured signal depends on the orientation of the scattering material with respect to the grating sensitivity direction [Bay14a; Yas11]. This feature can be used to extract the information about the orientation of different materials from the variations in the dark-field signal.

Dark-field imaging techniques have recently become quite popular in several fields of research by showing promising results not only in medical applications, such as the diagnosis of pulmonary emphysema in lungs, providing better resolution of small, calcified tumor nodules in breast scanning [Gra15; Yar13; And05; Sid11], the visualization of the orientation of bone micro-architecture without requiring high resolution detectors [Pot12], x-ray imaging using microbubbles as a scattering contrast [Vel13], reconstruction of tiny dental tubules [Vog15], but also in material science applications, for example to acquire quantitative information on the form and structure factor of materials [Pra15] and investigation of the fiber orientation of injection molded polymers [Han15; Rev11].

Jensen *et al.* [Jen10; Pot12] introduced directional two dimensional x-ray dark-field imaging or x-ray vector radiography (XVR) to reconstruct structure orientations from several projections acquired by rotating the sample around the beam propagation direction.

Malecki *et al.* [Mal14; Mal13] introduced a novel three-dimensional extension of directional X-ray dark-field imaging, called X-ray Tensor Tomography (XTT), which places the sample on an Eulerian cradle, which allows rotation of the sample with three degrees of freedom to provide a three-dimensional reconstruction of x-ray scattering tensors at each location of the scanned sample, revealing the local orientation and

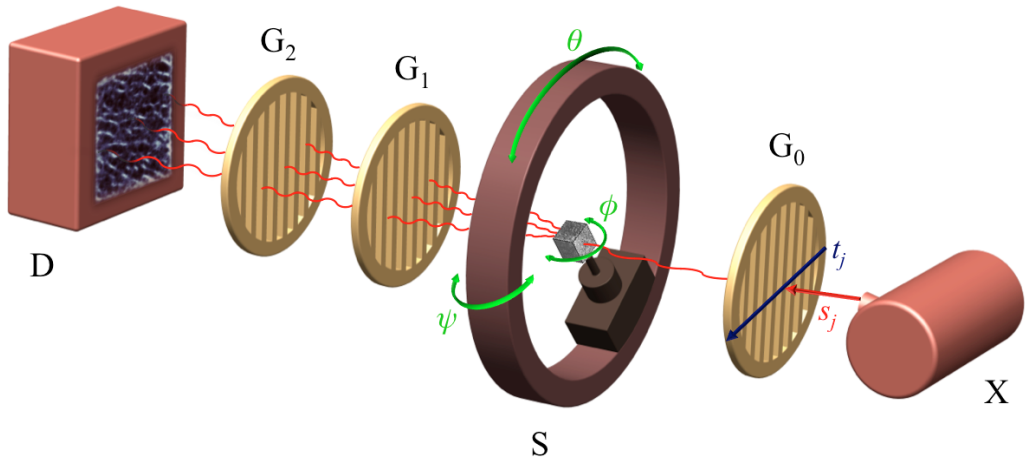

Figure 9.1.: Illustration of an x-ray tensor tomography setup including an x-ray tube (X), source grating (G_0), sample (S) mounted on an Eulerian cradle with three degrees of freedom (Euler angles ψ, θ, ϕ), shifting interferometer grating (G_1), static interferometer grating (G_2), and x-ray detector (D). The vector t_j refers to the sensitivity direction of the gratings, while s_j corresponds to the beam direction.

anisotropy of microstructures.

XTT is a promising technique with a number of applications, such as visualization of the directionally dependent information in three-dimensional volumes of carbon fibers, as well as medical imaging applications such as the visualization of tiny dentinal tubular structures of teeth. [Mal14; Vog15; Sey16b; Sey16a; Bay14b]. Recent studies, however, demonstrated the feasibilty of XTT imaging for larger variety of applications by introducing a sparse acquisition scheme to perform a full six dimensional XTT with at most two axes of sample rotation [Sha16] and also a novel general closed-form, continuous forward model for solving the anisotropic dark-field imaging to improve the resolution of multiple scattering directions in one volume element [Wie16].

9.3 XTT Setup and Acquisition

As illustrated in Figure 9.1, XTT is an ordinary setup of x-ray source and detector extended by an x-ray grating interferometer using three gratings (G_0, G_1, G_2) and the sample mounted on an Eulerian cradle.

While the sample is rotating around all three axes corresponding to the Euler angles (ψ, θ, ϕ), several horizontal steps of the phase grating (G_1) are used to acquire several images, allowing the recovery of the three signal components, attenuation contrast, phase-contrast and the dark-field contrast as shown in Figure 6.2 [Pfe06a; Bec10].

For XTT, the acquired dark-field images are used in an iterative reconstruction algorithm to recover scattering coefficients for different scattering directions, followed by a tensor fit.

An overview of the XTT acquisition and reconstruction method is shown in Figure 9.2.

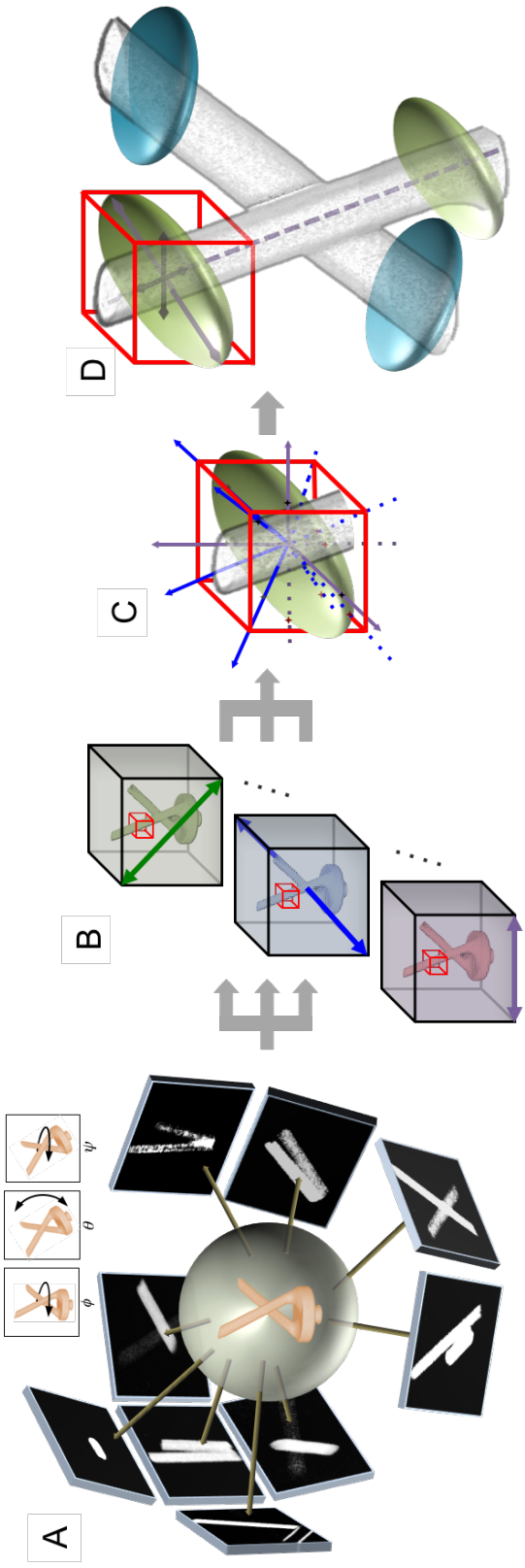

Figure 9.2.: An illustration of the XTT acquisition and reconstruction, (A) anisotropic dark-field signal from several non-standard acquisition poses, (B) simultaneously reconstructed scattering components, (C) tensor fitting from all scattering coefficients, and (D) smallest half-axis of the tensor represents the structure orientation. This Figure is adapted from [Sha16].

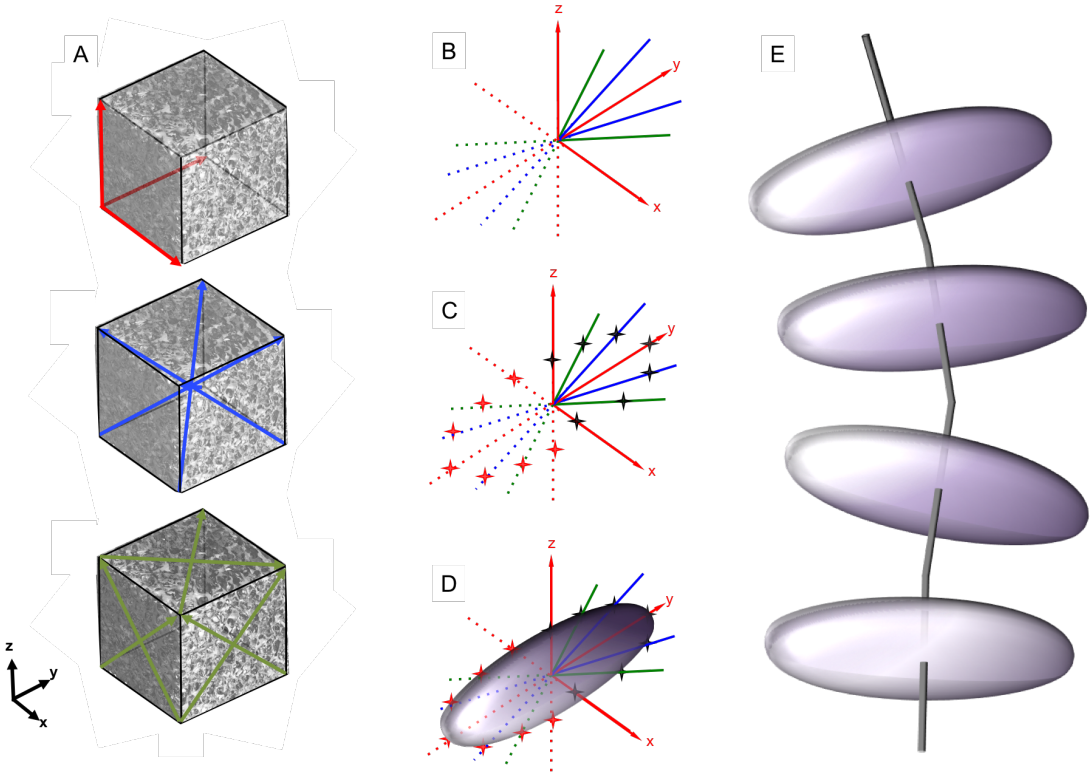

Figure 9.3.: Tensor fitting in x-ray tensor tomography: (A) Selected scattering directions $\hat{e}_k$, for example the coordinate axes, and the space and face diagonals, (B) scattering directions $\hat{e}_k$ shown for a location $x \in \mathbb{R}^3$ (coordinate axes shown in red, space diagonals shown in blue, and face diagonals shown in green), (C) scattering coefficients $\zeta_k(x)$ for every scattering direction $\hat{e}_k$ shown by black stars, corresponding mirrored coefficients along the negative scattering direction shown as red stars, (D) tensor fitted to the black and mirrored red stars, (E) several reconstructed scattering tensors, with their smallest half axis indicating the direction of a fiber or tube-like structure (in grey).

9.4 XTT Forward Model

As scattering is an anisotropic entity, a tensor in each location of the sample is required [Mal14]. In their work, Malecki *et al.* [Mal14] proposed to consider several auxiliary scattering directions $\hat{e}_k \in \mathbb{R}^3$, $k = 1, \ldots, K$, evaluating the tensor (see Figure 9.3(A,B)). For each of these directions and every location $x \in \mathbb{R}^3$, a corresponding scattering coefficient $\zeta_k(x) \in \mathbb{R}$ will be reconstructed, as illustrated in Figure 9.3(C). Finally, a tensor is fitted to the reconstructed scattering coefficients at location x using principal component analysis [Hot33] (see Figure 9.3(D)).

Every fitted tensor's major axis then points in the direction of maximum scattering, and the ratio between the length of the major and minor axis is a measure of the anisotropy at this location. For fibrous materials, the direction of the smallest half-axis indicates the direction of the fiber in that location (see Figure 9.3(E)).

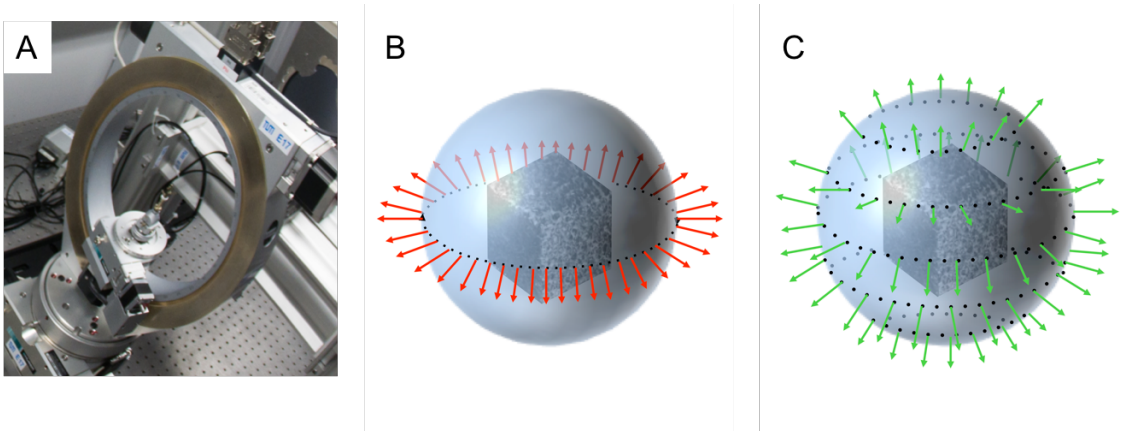

Figure 9.4.: CT and XTT viewing directions, (A) an Euler cradle used to sample the unit sphere for XTT measurements, (B) sampling coverage in CT and, (C) sampling unit sphere for XTT.

For tomographic reconstruction, we use the forward model proposed by Malecki *et al.* [Mal14],

$$m_j = \exp\left[-\int_{L_j} \sum_{k=1}^{K} \langle |\hat{s}_j \times \hat{e}_k| (\zeta_k(\mathrm{x})\hat{e}_k), \hat{t}_j \rangle^2 \mathrm{d}x \right]. \tag{9.1}$$

Here, $m_j \in \mathbb{R}$ denotes the j'th dark-field signal measurement, and $j = 1, ..., J$ extends over all pixels of all the detector images acquired for all angles ψ, θ, ϕ. L_j denotes the corresponding x-ray from the source to the j-th detector pixel, with normalized direction $\hat{s}_j \in \mathbb{R}^3$; the vector $\hat{t}_j \in \mathbb{R}^3$ denotes the normalized sensitivity direction of the grating interferometer and the $\hat{e}_k$ represent the normalized scattering directions chosen earlier, while $\zeta_k(x)$ represents the scattering coefficient to be reconstructed.

Since the measurements m_j depend on both the ray direction $\hat{s}_j$ and the grating sensitivity direction $\hat{t}_j$, it is necessary to rotate the sample not only around a single rotation axis as in traditional computed tomography, but to rotate it freely, sampling the unit sphere (see Figure 9.4).

9.5 XTT Reconstruction

Assuming a_j denotes the discretized x-ray transform along the ray-direction $\hat{s}_j$, then the matrix $A = (a_j), j = 1, ..., J$, also called 'system matrix', represents the measurement process. Furthermore, let the vector η_k denote the square root of the scattering coefficient ζ_k discretized on a voxel grid. Following the approach of Vogel *et al.* [Vog15], we then formulate the XTT reconstruction problem as a set of linear equations

$$-\ln m_j = \sum_{k=1}^{K} v_{kj} \langle a_j, \eta_k \rangle = \sum_{k=1}^{K} v_{kj} a_j^T \eta_k, \tag{9.2}$$

where the weight factors $v_{kj} := \left(|\hat{s}_j \times \hat{e}_k| \langle \hat{e}_k, \hat{t}_j \rangle \right)^2$ can be precomputed.

Assuming $diag(v_{kj})$ as a diagonal scaling matrix containing the weighting factors v_{kj} and Equation 9.2 a huge linear system can be derived as,

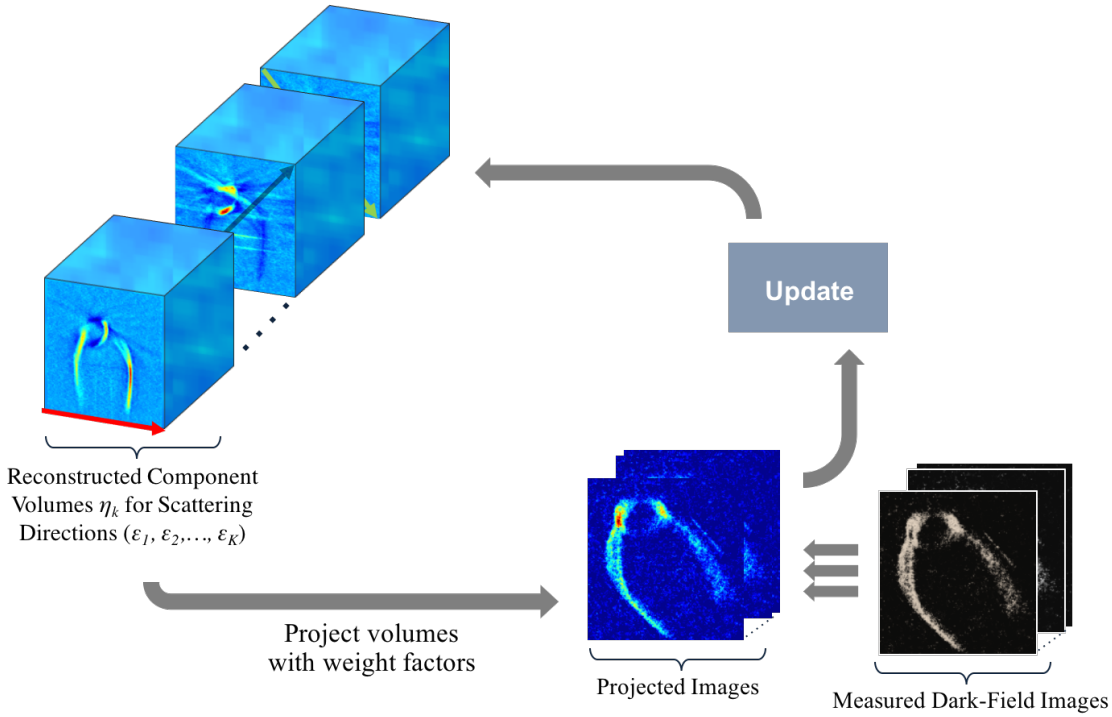

Figure 9.5.: Overview of the unregularized XTT reconstruction.

$$
\begin{aligned}
m &= \begin{bmatrix} v_{11}a_1^T \\ v_{12}a_2^T \\ \vdots \\ v_{1J}a_J^T \end{bmatrix} \eta_1 + \begin{bmatrix} v_{21}a_1^T \\ v_{22}a_2^T \\ \vdots \\ v_{2J}a_J^T \end{bmatrix} \eta_2 + \cdots + \begin{bmatrix} v_{K1}a_1^T \\ v_{K2}a_2^T \\ \vdots \\ v_{KJ}a_J^T \end{bmatrix} \eta_K \\
&= \begin{bmatrix} v_{11} & & & \\ & v_{12} & & \\ & & \ddots & \\ & & & v_{1J} \end{bmatrix} \begin{bmatrix} a_1^T \\ a_2^T \\ \vdots \\ a_J^T \end{bmatrix} \eta_1 + \begin{bmatrix} v_{21} & & & \\ & v_{22} & & \\ & & \ddots & \\ & & & v_{2J} \end{bmatrix} \begin{bmatrix} a_1^T \\ a_2^T \\ \vdots \\ a_J^T \end{bmatrix} \eta_2 + \cdots \\
&= diag(v_{1j})A\eta_1 + diag(v_{2j})A\eta_2 + \cdots + diag(v_{Kj})A\eta_K \\
&= \sum_k diag(v_{kj})A\eta_k = H\eta.
\end{aligned}
\tag{9.3}
$$

The reconstruction problem now reduces to computing K volumes η_k. As presented in Algorithm 5, unregularized reconstruction is performed iteratively in a block-sequential manner, starting with pre-computation of weighted forward projections WFP, and component-wise updates for modified right-hand sides r using a single CG iteration each.

An illustration of XTT reconstruction flowchart is shown in Figure 9.5. We will be using the abbreviation XTT for the unregularized XTT reconstruction (as in Algorithm 5).

Algorithm 3 X-ray tensor tomography reconstruction method. This algorithm is computing Q outer iterations of a block-sequential algorithm, using a single inner Conjugate Gradient step (CG). Here, diag(v_{kj}) denotes a diagonal scaling matrix containing the weighting factors v_{kj}, and A denotes the system matrix of the setup.

$\eta_k^0 = 0$ for all $k = 1, \ldots, K$
for outer iteration $q = 1$ to Q **do**
  // pre-compute weighted forward projections
  for scattering directions $k \in \{1, \ldots, K\}$ **do**
    $WFP_k = \text{diag}(v_{kj}) \cdot A \cdot \eta_k^{q-1}$
  end for

  // component-wise reconstruction
  for scattering directions $k \in \{1, .., K\}$ **do**
    // compute right-hand side
    $r = m - \sum_{l \neq k} WFP_l$
    // compute x_k using single CG iteration
    $x_k = \text{CG}(\text{diag}(v_{kj}) \cdot A, \quad r, \quad \eta_k^{q-1})$

    // update with relaxation
    $\eta_k^q = (1 - \frac{1}{k})\eta_k^{q-1} + \frac{1}{k} x_k$
  end for *// scattering directions k*
end for *// outer iteration q*

10. XTT Evaluation Techniques

10.1 Overview

In this chapter, we introduce several evaluation and image quality assessment techniques to investigate the existing XTT reconstruction methods and to compare them to the proposed regularized XTT reconstruction, denoising and regularization approaches in this study. A new tensor orientation evaluation method using the absorption images will be introduced in section 10.2 which follows with section 10.3 where we introduce couple of numerical analysis techniques to investigate and to compare the convergence of available and newly proposed methods. Finally, in section 10.4, several image quality assessment techniques will be introduced for noise estimation and contrast evaluation.

10.2 Tensor Orientation Evaluation

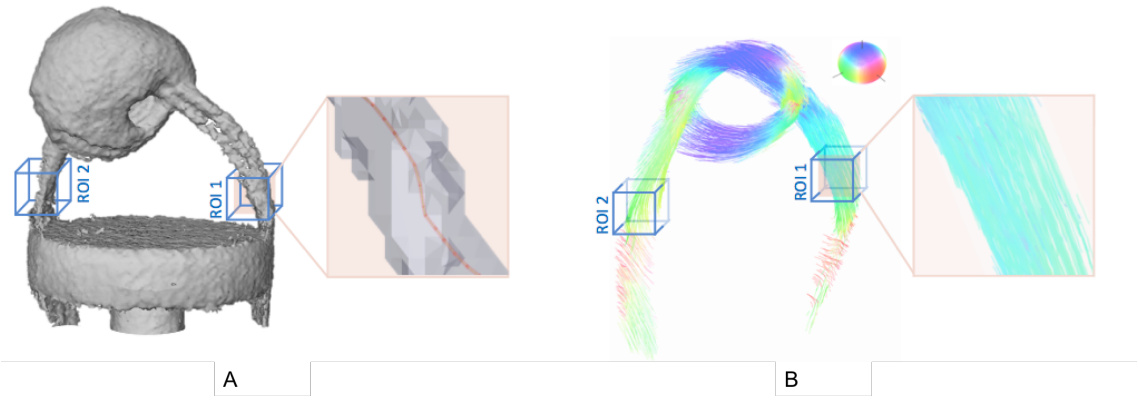

Figure 10.1.: Evaluation of XTT reconstructed images vs. attenuation image: (A) Fast marching method calculating centerline in region of interest of attenuation image, and (B) XTT orientations calculated after fitting tensor to XTT reconstructed image zoomed for the same region of interest.

In order to evaluate the orientations acquired after tensor fitting to XTT reconstructed images (as described in Figure 9.3), the attenuation contrast images of the carbon knot sample have been reconstructed using the attenuation projections which are acquired at the same time as dark-field projections measurements in XTT setup. Acquiring both attenuation and dark-field projections at the same time in XTT setup helps to do any of post evaluation steps without need to performing registration. Finally, we choose two regions of interest in reconstructed attenuation as well as in XTT reconstructed images as shown in Figure 10.1 and calculate the orientation of the attenuation image of carbon knot sample,W_{amp}, in these regions using fast marching centerline method [Bær01; HF07].

For evaluation we use,

$$\delta = \tan^{-1}\left(\frac{\|W_{amp} \times W_{xtt}\|}{W_{amp} \cdot W_{xtt}}\right), \tag{10.1}$$

where δ denotes the angle between W_{amp}, and corresponding W_{xtt} denoting the XTT direction extracted after tensor fitting in the same region [Sey18c].

10.3 Numerical Analysis

In order to study the numerical behavior of the proposed methods, we computed the normalized residual norms,

$$r^{(q)} := \frac{\|m - \sum_k diag(v_{kj}) \cdot A \cdot \eta_k^{(q)}|_2}{\|m\|_2}, \tag{10.2}$$

and also the normalized update,

$$\triangle^{(q)} := \frac{\text{mean}\|\eta_k^{(q)} - \eta_k^{(q-1)}\|_2}{\|\eta_k^{(q)}\|_2}. \tag{10.3}$$

10.4 Image Quality Assessment

In order to quantitatively measure the contrast in the images for the three different methods, we compute the contrast-to-noise ratio CNR() as,

$$CNR = \frac{|\bar{\eta}_{ROI} - \bar{\eta}_{BG}|}{\sigma_{BG}}, \tag{10.4}$$

where $\bar{\eta}_{BG}$ denotes the mean of the scattering signal of the all background (BG) area which is segmented and masked out using threshold mask.

Another qualitative evaluation metric that we use here is the signal-to-noise ratio (SNR),

$$SNR = \frac{\bar{\eta}_{ROI}}{\sigma_{BG}}, \tag{10.5}$$

where $\bar{\eta}_{ROI}$ denotes the mean of the scattering signal in a certain region of interest (ROI) of a component image η and σ_{BG} refers to the standard deviation of the background (BG) of each component.

To estimate noise levels, we use the median absolute deviation (MAD)[MT77],

$$MAD = \text{median}\big(|\eta_{ROI} - \text{median}(\eta_{ROI})|\big), \tag{10.6}$$

11. XTT Reconstruction, Regularization and Noise Reduction

11.1 Overview

In this chapter, we introduce several regularized reconstruction methods, noise reduction approaches and post processing techniques for XTT imaging data . We propose various regularized XTT reconstruction techniques such as parallel-block regularized XTT reconstruction technique in sections 11.2.2 and 11.2.1 and the whole-system regularized XTT reconstruction approach in section 11.3. Furthermore, two different noise reduction methods will be introduced for incorporation of denoising step into the projection domain measurements and image domain data respectively in sections 11.2.1 and 11.2.2. Finally, in section 11.6, we will explain several conducted experiments to evaluate the proposed methods and the corresponding results will be illustrated in section 11.7.

11.2 Block-parallel Regularized XTT Reconstruction Methods

Measured XTT data is always subject to signal fluctuations of various origins, which are generally and collectively referred to as "noise". The noise present in the recorded raw dark-field images will propagate through the reconstruction algorithm and influence the quality of the resulting images. Chabior *et al.*[Cha11] showed that the noise in dark-field contrast images will always be higher than in attenuation-contrast images. Thus, the XTT imaging modality is very vulnerable to noise and should highly profit from denoising.

Total variation (TV) denoising is a well-known technique that was originally developed for denoising images with additive Gaussian noise by Rudin, Osher and Fatemi [ROF92]. Since then, TV methods have been successfully applied to a multitude of other image denoising problems, also within the computed tomography community[SP08; CTL08b; SY14b; Sey13b; Ert12; Sey14]. In particular, the TV denoising approach is often used in order to recover images with a reduced noise level, while preserving the edges of the underlying signal.[CL97; DS96].

In this section, we investigate the applicability of component based denoising approach in XTT modality by incorporating a TV denoising step into the XTT reconstruction using two different pipeline designs and evaluate the best way to incorporate the TV noise reduction step for XTT data.

11.2.1 ADMM Regularized XTT Reconstructions

In this section, we introduce a way to add a total variation (TV) regularization step when updating each XTT component η_k. For this purpose, we use several iterations of the

alternating direction method of multipliers (ADMM) method in place of the original conjugate gradient (CG) step of XTT reconstruction method in section 9.5, which provides us with reasonable convergence rates within the first few iterations for each component [Boy11].

For each component, we thus compute an approximate solution as,

$$\arg\min_{\eta_k} \left\{ \tfrac{1}{2}\|A\eta_k - m\|_2^2 + \lambda\|z\|_1 \right\} \quad s.t. \quad F\eta_k = z. \tag{11.1}$$

where m refers to the full measurement vector $m = (m_j)$, F denotes the discretized finite differences operator and $\lambda \in \mathbb{R}$ refers to the regularization parameter.

The p-th iteration of ADMM now reduces to three steps. First we approximately solve a Tikhonov-regularized linear system for η_k using three iterations of conjugate gradient,

$$(A^T A + \rho F^T F)\eta_k^{p+1} = (A^T m + \rho F^T z^p + u^p), \tag{11.2}$$

where $\rho \in \mathbb{R}$ denotes the coupling parameter.

Second we perform the update,

$$z^{p+1} = S_{\lambda/\rho}(F\eta_k^{p+1} + u^p), \tag{11.3}$$

where $S_{\lambda/\rho}$ denotes the soft-thresholding operator. As third step we finally perform the update:

$$u^{p+1} = u^p + F\eta_k^{p+1} - z^{p+1}. \tag{11.4}$$

The full algorithm of the component-based TV regularization method $isshortrXTT - ADMM$ for XTT is shown in Algorithm 4. It consists of the outer iterations of the previous sequential algorithm [Vog15] to update each of the components η_k, as well as our proposed component-based TV regularization using several inner iterations of ADMM [Sey16b].

11.2.2 Total-Variation Regularized XTT Reconstruction

One approach to reduce noise in XTT is to incorporate anisotropic TV regularization into the standard XTT reconstruction method. To do so, we keep the iterative component-based scheme of unregularized XTT reconstruction, using Q outer iterations. However, in addition to the single CG step for each component η_k, we add a consecutive step applying TV regularization only to that component η_k.

To perform TV regularization, we use several iterations of the alternating direction method of multipliers [Boy11] (ADMM) applied separately to each component η_k,

$$\arg\min_{\eta} \left\{ \tfrac{1}{2}\|\eta - \eta_k\|_2^2 + \lambda\|F\eta\|_1 \right\}, \tag{11.5}$$

where $\lambda \in \mathbb{R}$ refers to the regularization parameter and F denotes the finite differences operator. The computational cost for each regularization step is negligible compared to the cost of the CG step.

The algorithm of component-based TV regularized CG reconstruction for XTT (in short rXTT) is shown in Algorithm 5. Figure 11.1 displays a simplified flowchart of the proposed regularized XTT (rXTT) technique [Sey18b].

Algorithm 4 ADMM regularized x-ray tensor tomography reconstruction method. This algorithm consists of the outer iterations of the previous sequential algorithm introduced in section 9.5 to update each of the components η_k, as well as our proposed component-based TV regularization using several inner iterations of ADMM.

$\eta_k^0 = 0$ for all $k = 1, \ldots, K$
for outer iteration $q = 1$ to Q **do**
  // pre-compute weighted forward projections
  for scattering directions $k \in \{1, \ldots, K\}$ **do**
    $WFP_k = \text{diag}(v_{kj}) \cdot A \cdot \eta_k^{q-1}$
  end for

  // component-wise reconstruction
  for scattering directions $k \in \{1, .., K\}$ **do**
    // compute right-hand side
    $r = m - \sum_{l \neq k} WFP_l$

    // run several ADMM iterations to compute x_k
    for inner iteration $p = 1$ to P **do**
      // step 1 of ADMM
      solve for x_k using three iterations of CG
      $(A^T A + \rho F^T F)(x_k^{p+1}) = (A^T r + \rho F^T z^p + u^p)$
      // step 2 of ADMM
      $z^{p+1} = S_{\lambda/\rho}(F x_k^{p+1} + u^p)$
      // step 3 of ADMM
      $u^{p+1} = u^p + F x_k^{p+1} - z^{p+1}$
    end for

    // update coefficients with relaxation
    $\beta = 1/K$
    $\eta_k^q = (1 - \beta)\eta_k^{q-1} + \beta x_k$
  end for *// scattering directions k*
end for *// outer iteration q*

11.3 Whole-System Regularized XTT Reconstruction Method

In addition to the component-wise block-parallel approach, we can also interpret the XTT reconstruction problem as a single linear system. The block-parallel approach, was introduced in section 11.2, in which we aimed to compute the tomographic reconstruction for each scattering direction in parallel. We will use the same problem formulation as a large-scale linear system, and directly apply an algorithm to deal with the whole linear problem at once.

Instead of the component-wise block-parallel approach, here, we can interpret the XTT reconstruction problem as a single linear system, with an unknown $\boldsymbol{\eta}$ consisting of all the components (η_k). For this we define the diagonal scaling matrix $D_k :=$

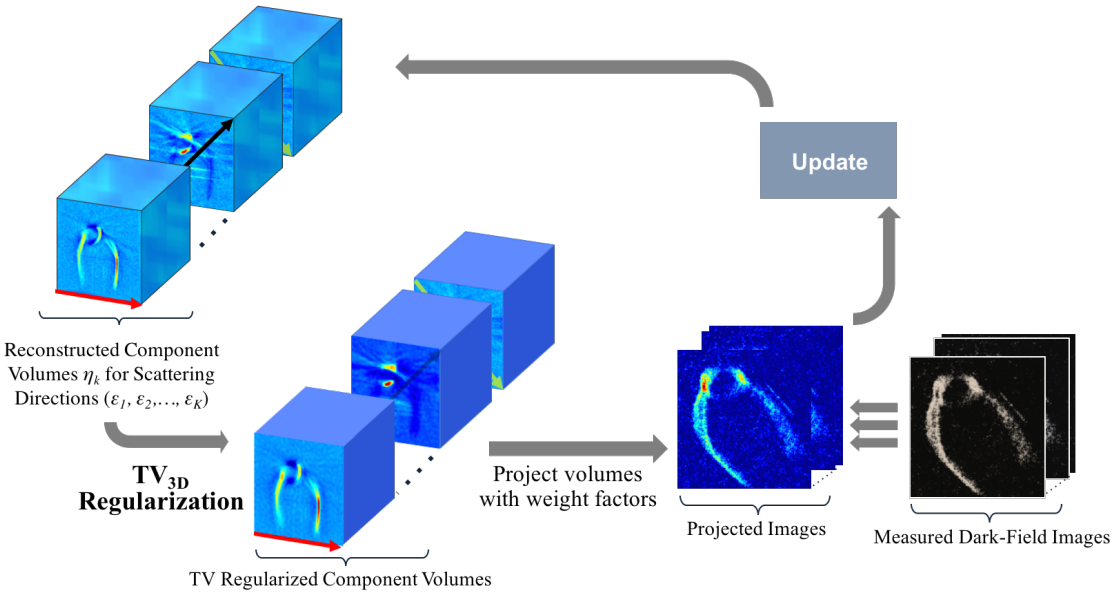

Figure 11.1.: Overview of the regularized XTT reconstruction.

$diag(v_{k1}, v_{k2}, ..., v_{kJ})$ containing the weight factors v_{kj}, we abbreviate $\boldsymbol{\eta} := (\eta_1, \ldots, \eta_K)$ and $\boldsymbol{m} := (m_1, \ldots, m_J)$ and can now write the XTT reconstruction problem as the linear system

$$\boldsymbol{m} = \boldsymbol{H}\boldsymbol{\eta} \tag{11.6}$$

using $\boldsymbol{H} := (D_1 A, D_2 A, ..., D_K A) \in \mathbb{R}^{J \times IK}$, a column block matrix.

We now add TV regularization and solve the whole system

$$\arg\min_{\boldsymbol{\eta}} \left\{ \tfrac{1}{2} \|\boldsymbol{H}\boldsymbol{\eta} - \boldsymbol{m}\|_2^2 + \lambda \|F\boldsymbol{\eta}\|_1 \right\} \tag{11.7}$$

using ADMM, applying again a few CG iterations for the data term and soft-thresholding for the ℓ_1 term. Please note that the finite differences operator F here respects the component boundaries of the η_k.

We will be using the abbreviation wXTT for the whole-system regularized XTT reconstruction in the following sections.

11.4 Projection Domain Denoising

The noise originally appears in the measured dark-field images, and is amplified by the ill-posed[Had02] XTT reconstruction process. Hence we propose to use two-dimensional TV denoising (TV_{2D}) directly on the acquired dark-field images (also called "projections"). Similar to rXTT previously, we employ ADMM on the measured dark-field images m,

$$\arg\min_{x} \left\{ \tfrac{1}{2} \|x - m\|_2^2 + \lambda \|Fx\|_1 \right\}, \tag{11.8}$$

performing two-dimensional TV denoising for each dark-field image m separately [Sey18b]. This approach is illustrated in Figure 11.2, and we abbreviate this method as TV→XTT in the following.

Algorithm 5 Regularized x-ray tensor tomography reconstruction method. This algorithm is computing Q outer iterations of a block-sequential algorithm, using a single inner Conjugate Gradient step (CG). P inner iterations of ADMM with TV are executed after CG for each component. Here, $\mathrm{diag}(v_{kj})$ denotes a diagonal scaling matrix containing the weighting factors v_{kj}, and A denotes the system matrix of the setup.

$\eta_k^0 = 0$ for all $k = 1, \ldots, K$
for outer iteration $q = 1$ to Q **do**
  // pre-compute weighted forward projections
  for scattering directions $k \in \{1, \ldots, K\}$ **do**
    $WFP_k = \mathrm{diag}(v_{kj}) \cdot A \cdot \eta_k^{q-1}$
  end for

  // component-wise reconstruction
  for scattering directions $k \in \{1, .., K\}$ **do**
    // compute right-hand side
    $r = m - \sum_{l \neq k} WFP_l$
    // compute x_k using single CG iteration
    $x_k = \mathrm{CG}(\mathrm{diag}(v_{kj}) \cdot A, \quad r, \quad \eta_k^{q-1})$

    // TV using several ADMM iterations
    for inner iteration $p = 1$ to P **do**
      $x_k = \mathrm{ADMM}(I, \quad x_k, \quad x_k)$
    end for

    // update with relaxation
    $\beta = 1/K$
    $\eta_k^q = (1 - \beta)\eta_k^{q-1} + \beta x_k$
  end for *// scattering directions k*
end for *// outer iteration q*

11.5 Image Domain Denoising

Similarly, one can denoise the resulting component images after reconstruction. Here, we apply three-dimensional TV denoising on each reconstructed component η_k separately after the unregularized reconstruction technique described in Algorithm 5. Here we also use the anisotropic TV model with ADMM, solving

$$\arg\min_{\eta} \left\{ \tfrac{1}{2} \|\eta - \eta_k\|_2^2 + \lambda \|F\eta\|_1 \right\}. \tag{11.9}$$

This approach is illustrated in Figure 11.3 and is abbreviated as XTT→TV in the following sections.

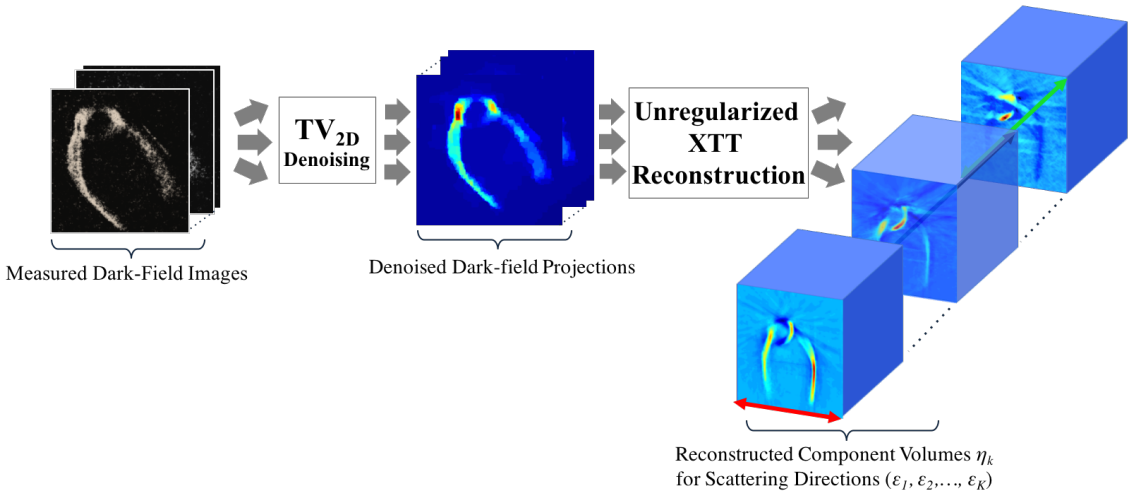

Figure 11.2.: Overview of the projection domain TV denoising for XTT reconstruction.

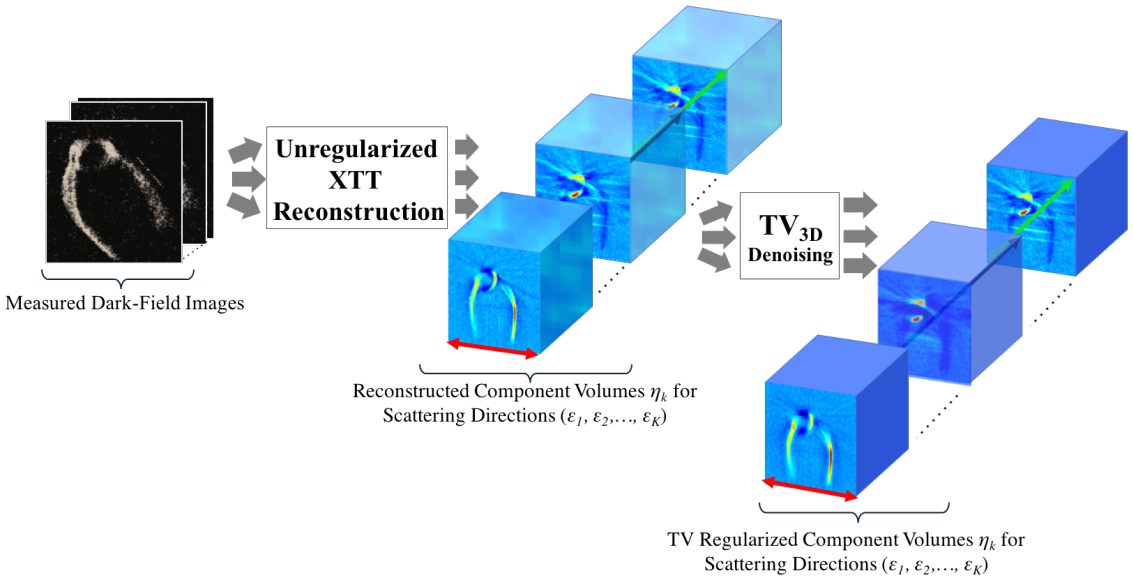

Figure 11.3.: Overview of the image domain TV denoising for XTT reconstruction.

11.6 Experiments

In this section, we show the experiments conducted to evaluate the proposed methods by applying them to several medical and non-medical sample datasets.

All samples were measured in the XTT setup located at our institute. The x-ray source was a conventional x-ray tube (MXR-160HP/11, Comet AG, Switzerland) with a focal spot size of 0.4 mm^2. Both measurements were performed at an acceleration voltage of 60 kVp. A flat panel x-ray detector with pixel pitch of 127μm (Varian PaxScan2520D, Varian Medical Systems, USA) was used to acquire the images. G_0 and G_2 were absorption gratings with a period of 10 μm and a duty cycle of 0.5, the phase grating G_1 had a phase shift of $\pi/2$ with a period of 5 μm and a duty cycle of 0.5. The grating G_2 was positioned in the first fractional Talbot distance. The grating G_1 was stepped for eight

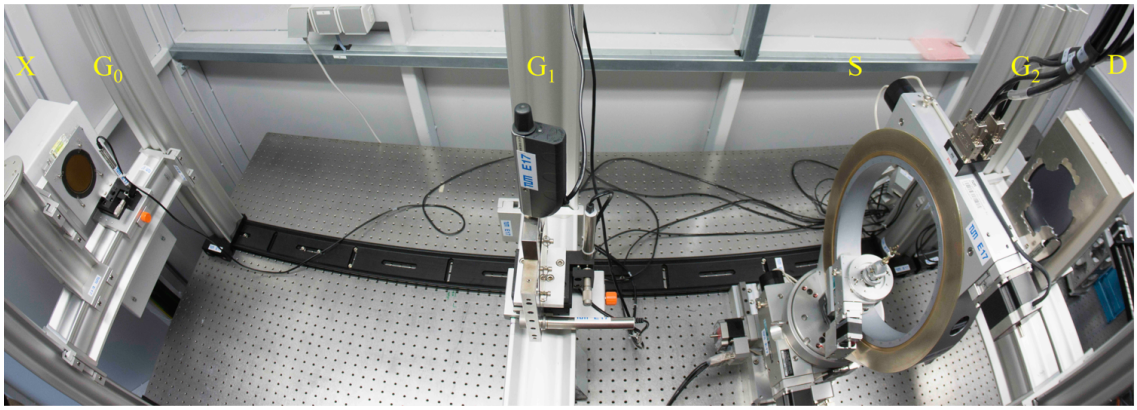

Figure 11.4.: Photography of the XTT setup used to measure the samples. From left to right: (S) x-ray source, (G_0) source grating, (G_1) phase grating, (S) sample mounted on the Euler cradle, (G_2) the analyzer grating and, (D) the detector

equally distanced phase steps in order to acquire sufficient data with an exposure time of 1 s per phase step for a stable extraction of the signal components including dark-field signal.[Pfe06a].

Our proposed methods are implemented within our C++ software framework for linear inverse problems, *CampRecon* [WVL14]. All experiments were run on a computer with dual Intel Xeon E5-2643 processors and four Nvidia Tesla K10 accelerators.

Each of the proposed methods were set to use $Q = 50$ outer iterations and $P = 2$ inner iterations (without employing any other stopping criterion). 13 scattering directions $\hat{\epsilon}_k$ were chosen as illustrated in Figure 9.3(a).

11.6.0.1 Carbon Fiber Knot Sample

The first sample is a "carbon knot", a knotted bunch of carbon fibers fixed by glue.

We use 112 dark-field images of 210×210 pixels acquired at different angles (ψ, θ, ϕ) for the carbon knot sample to reconstruct a discretized volume of 210^3 isotropic voxels.

Carbon knot sample was mounted in an Eulerian cradle at a position of 61.5 cm

Figure 11.5.: Photography of the carbon knot sample.

Figure 11.6.: Photography of the crossed sticks sample.

upstream of grating G_1 and where $\psi \in \{0°, 20°, 40°\}$, $\theta \in \{0°, 30°, 60°, 90°\}$ and $\phi \in \{0°, 30°, 60°, 90°\}$.

11.6.0.2 Crossed Sticks Sample

The second sample we used is a "crossed sticks", which consists of two wooden sticks attached to a sample holder using hot glue.

We use 121 x-ray dark field projections of 320×320 pixels, sparsely sampling the unit sphere. The reconstruction volume was discretized using 320^3 isotropic voxels.

Crossed sticks sample was mounted in an Eulerian cradle at a position of 61.5 cm upstream of grating G_1 and where $\psi \in \{0°, 20°, 40°\}$, $\theta \in \{0°, 30°, 60°, 90°\}$ and $\phi \in \{0°, 30°, 60°, 90°\}$.

11.6.0.3 Femur Sample

The second sample is a "femur sample", a human femur head bone sample excised into a cubic shape of 1 cm^3. We use 116 dark-field images of 350×350 pixels also acquired at different angles (ψ, θ, ϕ) for the femur sample to reconstruct a discretized volume of 350^3 isotropic voxels.

For the femur sample, we used a combination of Eulerian angles including $\psi \in \{0°, 20°, 40°\}$, $\theta \in \{0°, 30°, 60°, 90°\}$ and $\phi \in \{0°, 30°, 60°, 90°\}$.

11.6.1 Regularization Techniques Investigation

In this section, investigate the performance of implemented XTT, XTT-ADMM, rXTT and wXTT reconstruction methods. In order to have comparable computational costs, we selected 54 outer iterations for the original XTT reconstruction method and the proposed rXTT method (with 5 inner iterations to compute the TV regularization), while we used 6 outer iterations and 9 inner iterations for the XTT-ADMM method. Using grid search, we selected the coupling parameter $\rho = 10$ for the XTT-ADMM method and $\rho = 100$ for the proposed rXTT method. The regularization parameter λ was chosen using an adaptive thresholding scheme, such that 99% of the coefficients are zero afterwards.

The corresponding results of this experiment will be shown in section 11.7.1.

11.6.2 Denoising Techniques Investigation

ADMM has two parameters, the regularization parameter λ and the coupling parameter ρ. Due to the lack of any ground truth, we performed a systematic grid search to select the best parameters empirically by visual assessment. For the carbon knot sample, this resulted in the coupling parameter $\rho = 10^3$.

For the regularization parameter λ, we use an indirect scheme by choosing an adaptive percentual thresholding parameter β between 0% and 100%, such that β percent of the coefficients are zero. For the first experiments, we fixed $\beta = 80\%$ for all proposed methods to compare their performance in carbon knot dataset. Secondly, we additionally chose β such that identical noise levels are achieved according to the MAD estimator.

In particular, for the estimated noise level of 0.020, which is reached by setting β to 80% in rXTT, this leads to β =76% for wXTT, β =89% for TV→XTT and β =85% for XTT→TV. For the estimated noise level of 0.005, this leads to β =88% for wXTT, β =96% for TV→XTT, β =87% for rXTT and β =94% for XTT→TV and for the estimated noise level of 0.100, this leads to β =65% for wXTT, β =74% for TV→XTT, β =64% for rXTT and β =72% for XTT→TV (see Figure 11.13).

The corresponding results of this experiment will be shown in section 11.7.2.

11.7 Results

11.7.1 Regularization Techniques Investigation

Figure 11.8 shows the center slice of reconstructed component volumes η_1 for three scattering directions $\hat{\epsilon}_1 = (1, 0, 0)^T$, η_8 for $\hat{\epsilon}_8 = (0.7, 0.7, 0)^T$ and η_9 for $\hat{\epsilon}_9 = (0.7, -0.7, 1)^T$.

On the left hand side, the slices are from the unregularized XTT reconstruction, the middle column shows the result of the ADMM method, while the right hand side shows the results of the rXTT method. Corresponding CNR results are shown in Table 11.1.

Comparison of the components in Figure 11.8 demonstrates a qualitative improvement when using regularization, in particular in terms of suppressed background noise. Compared to ADMM approach, the proposed rXTT approach allows for an efficient incorporation of TV regularization and shows better noise suppression, while demonstrating less artifacts (see for example Figure 11.8(E) vs. (H)). The visualization of the fitted tensors in Fig. 11.9 shows a marked improvement, with smoother tensors representing the structure orientations, while the background is less noisy.

Figure 11.7 shows a comparison of $r^{(q)}$ and $\triangle^{(q)}$ for the three methods. The XTT method shows the smallest residual norm $r^{(q)}$, but oscillating behavior in update $\triangle^{(q)}$, while both the XTT-ADMM method and rXTT method show a larger residual norm and smoother updates.

Table 11.1.: CNR of slices from Fig. 11.8. Representative ROI is marked in red and background as green in Fig. 11.8(A).

Component	XTT	XTT-ADMM	rXTT
$\hat{\epsilon}_1$	2.63×10^5	2.88×10^5	1.32×10^6
$\hat{\epsilon}_8$	2.14×10^5	3.73×10^5	4.84×10^5
$\hat{\epsilon}_9$	4.40×10^5	8.07×10^5	1.04×10^6

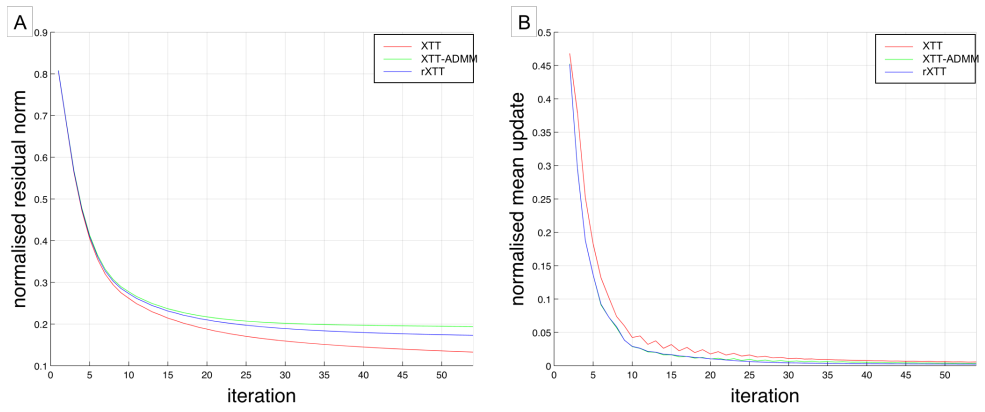

Figure 11.7.: Comparison of (A) normalized residual norm $r^{(q)}$ and (B) normalized mean update $\triangle^{(q)}$ for the three studied reconstruction methods.

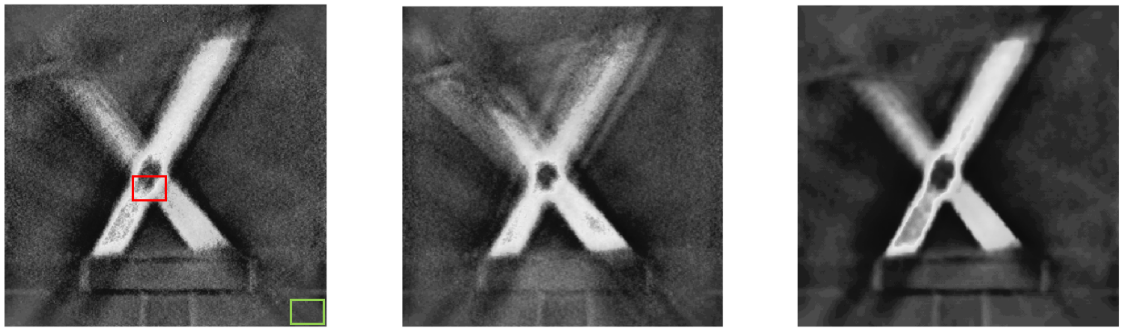

(A) XTT
$\hat{\epsilon}_1 = (1, 0, 0)^T$

(D) XTT-ADMM
$\hat{\epsilon}_1 = (1, 0, 0)^T$

(G) rXTT
$\hat{\epsilon}_1 = (1, 0, 0)^T$

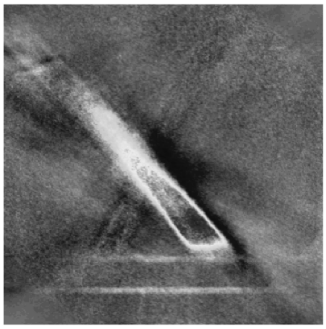

(B) XTT
$\hat{\epsilon}_8 = (0.7, 0.7, 0)^T$

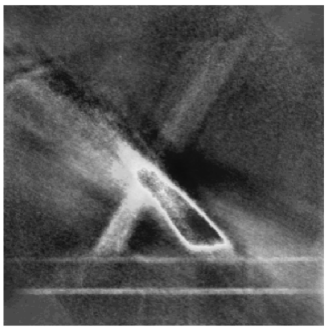

(E) XTT-ADMM
$\hat{\epsilon}_8 = (0.7, 0.7, 0)^T$

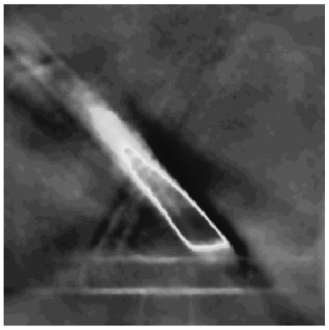

(H) rXTT
$\hat{\epsilon}_8 = (0.7, 0.7, 0)^T$

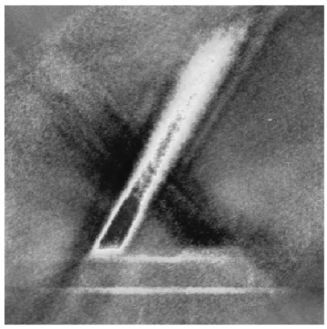

(C) XTT
$\hat{\epsilon}_9 = (0.7, -0.7, 1)^T$

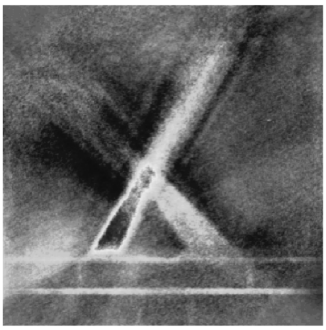

(F) XTT-ADMM
$\hat{\epsilon}_9 = (0.7, -0.7, 1)^T$

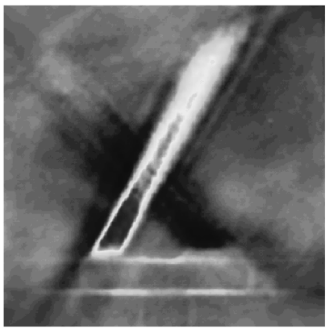

(I) rXTT
$\hat{\epsilon}_9 = (0.7, -0.7, 1)^T$

Figure 11.8.: Illustration of center slice of the reconstructed component volumes of crossed-sticks dataset using XTT, ADMM regularized XTT and TV regularized XTT reconstruction techniques corresponding to the scattering directions $\hat{\epsilon}_1, \hat{\epsilon}_8$. and $\hat{\epsilon}_9$ for all three methods. All images windowed to $[0.1, 0.9]$.

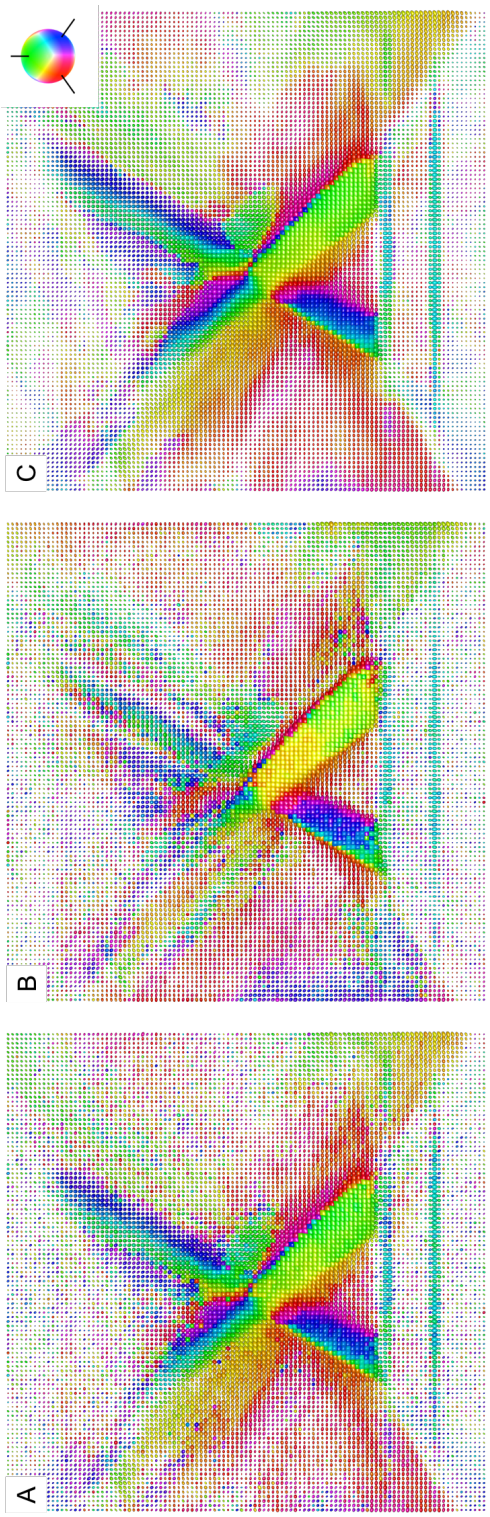

Figure 11.9.: Tensor visualization of a single slice of the reconstructed crossed sticks sample for all three methods: (A) XTT, (B) ADMM, and (C) rXTT. The structure orientation is color encoded as shown in orientation sphere in the right side of this figure.

11.7.2 Denoising Techniques Investigation

11.7.2.1 Dark-Field Projection Denoising

11.7.2.1.1. Carbon Knot Sample Figure 11.10 illustrates three dark-field images measured from carbon knot sample in three angle combinations $(\psi = 20°, \theta = 45°, \phi = 60°)$, $(\psi = 0°, \theta = 0°, \phi = 0°)$ and $(\psi = 0°, \theta = 60°, \phi = 0°)$, along with the results of two-dimensional TV denoising. As shown in this figure, for projection domain noise reduction (TV→XTT) of carbon knot sample, the noise level measured in terms of MAD and SNR shows a significant improvement for each of the dark-field images.

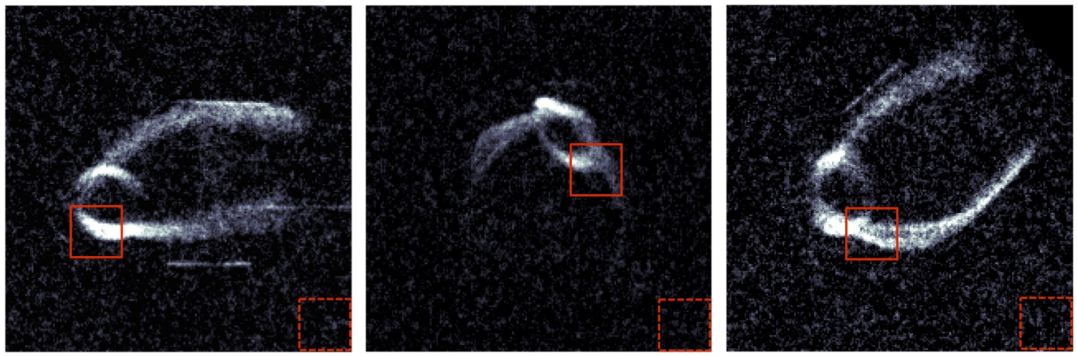

(A)
MAD: 0.051
SNR: 4.718

(B)
MAD: 0.041
SNR: 4.163

(C)
MAD: 0.053
SNR: 4.040

(D)
MAD: 0.032
SNR: 7.513

(E)
MAD: 0.030
SNR: 7.360

(F)
MAD: 0.029
SNR: 6.908

Figure 11.10.: Example images of two-dimensional TV denoising of dark-field image measurements of the carbon knot dataset, windowed to [0.1,0.75], (A-C) showing angle combinations $(\psi = 20°, \theta = 45°, \phi = 60°)$, $(\psi = 0°, \theta = 0°, \phi = 0°)$ and $(\psi = 0°, \theta = 60°, \phi = 0°)$, respectively, before denoising and (D-F) showing the same angles after denoising with β fixed to 80%. Corresponding MAD and SNR values are displayed below each image.

11.7.2.1.2. Femur Sample Figure 11.11 illustrates three dark-field images measured from three angle combinations $(\psi = 20°, \theta = 45°, \phi = 60°)$, $(\psi = 0°, \theta = 0°, \phi = 0°)$ and

$(\psi = 0°, \theta = 60°, \phi = 0°)$ of the femur sample, along with the results of two-dimensional TV denoising. As shown in this figure, for projection domain noise reduction (TV→XTT) of the femur sample, the noise level measured in terms of MAD and SNR shows a significant improvement for each of the dark-field images.

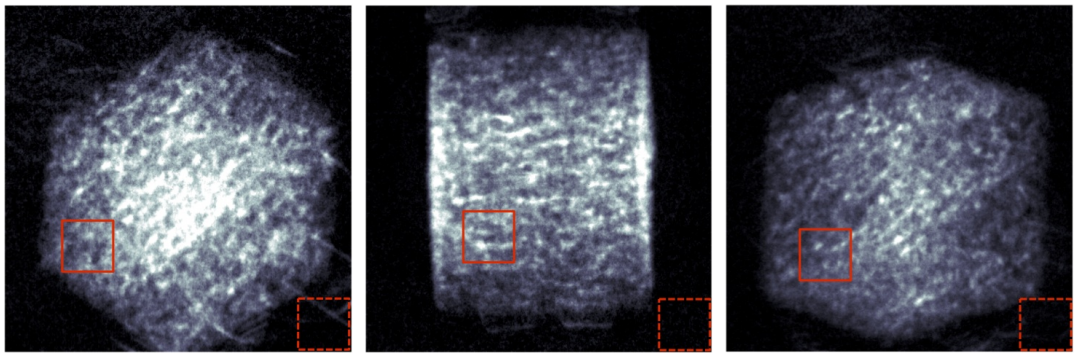

(A) MAD:0.029 SNR:6.812 | (B) MAD:0.028 SNR:6.933 | (C) MAD:0.029 SNR:6.500

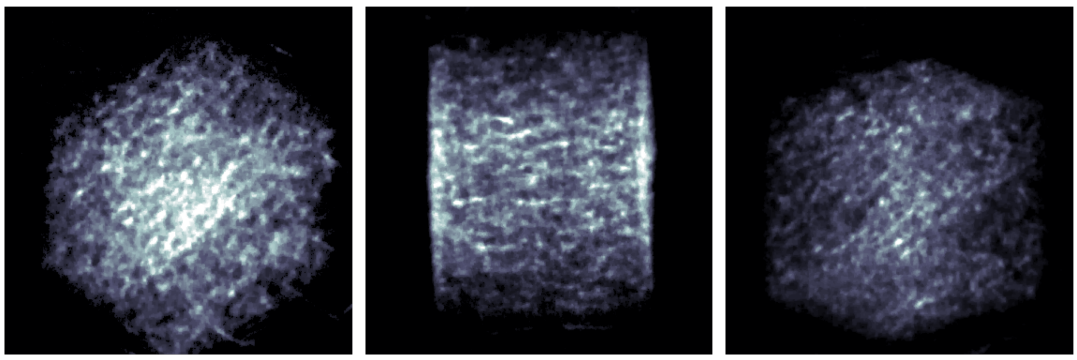

(D) MAD:0.027 SNR:7.673 | (E) MAD:0.025 SNR:7.574 | (F) MAD:0.025 SNR:7.671

Figure 11.11.: Illustration of two-dimensional TV denoising on dark-field image measurements of the femur dataset, (a-c) showing angle combinations of $(\psi = 20°, \theta = 0°, \phi = 180°)$, $(\psi = 0°, \theta = 30°, \phi = 0°)$ and $(\psi = 36°, \theta = 0°, \phi = 0°)$ respectively, before denoising and (d-f) showing the same angles after denoising with β fixed to 80%. Corresponding MAD and SNR values are displayed below each image.

11.7.2.2 Reconstructed Components

11.7.2.2.1. Carbon Knot Sample Figure 11.12 shows the center slice of the reconstructed and denoised component of the carbon knot dataset corresponding to the scattering direction $\hat{e}_3 = (0, 0, 1)$, with a zoomed area of interest marked in red boxes, and corresponding MAD estimates in the captions.

Reconstruction using the denoised dark-field images, instead of the original ones, shows a both qualitative and quantitative improvement in the reconstructed carbon knot

volumes, as shown in Figure 11.12(E). However, the TV→XTT approach requires a fairly high regularization parameter in order to compete with the rXTT and wXTT methods in terms of CNR and MAD which results in flatten features that are indistinguishable from noise as shown in Figure 11.12. This denoising methods can also lead to amplified streaking artifacts, as can be seen in Figure 11.12(B).

Both regularized XTT reconstruction (rXTT) and whole-system regularized XTT (wXTT) methods shows the most promising results for experimented knot dataset by reducing noise level and improving CNR compared to all other approaches, as seen in all the results.

In particular, for the carbon knot sample, the rXTT and wXTT methods are significantly reducing the background noise and dampens streak artifacts, as shown in Figure 11.12(A-E).

In order to investigate the effect of regularization parameters, we provide more data points by showing the results for parameters β, which lead to the same noise level as estimated by MAD in Figure 11.13 for carbon knot sample. In particular, for the estimated noise level of 0.020, which is reached by setting β to 80% in rXTT, this leads to β =76% for wXTT, β =89% for TV→XTT and β =85% for XTT→TV. For the estimated noise level of 0.005, this leads to β =88% for wXTT, β =96% for TV→XTT, β =87% for rXTT and β =94% for XTT→TV and for the estimated noise level of 0.100, this leads to β =65% for wXTT, β =74% for TV→XTT, β =64% for rXTT and β =72% for XTT→TV.

11.7.2.2.2. Femur Sample Figure 11.14 shows the center slice of the reconstructed and denoised component of the carbon knot dataset corresponding to the scattering direction $\hat{\epsilon}_1 = (1, 0, 0)$, with a zoomed area of interest marked in red boxes, and corresponding MAD estimates in the captions.

Similar to the results acquired for carbon knot sample, reconstruction using the denoised dark-field images, instead of the original ones, shows qualitative and quantitative improvements in the reconstructed femur sample volumes, as shown in Figure 11.14(E).

Regularized XTT reconstruction (rXTT) and whole-system regularized XTT reconstruction (wXTT) methods shows the most promising results for femur datasets by reducing noise level and improving CNR compared to all other approaches, as seen in all the results.

In particular, for the femur sample, the rXTT and wXTT methods are significantly reducing the background noise and dampens streak artifacts, as shown in Figure 11.14(A-E).

Denoising of the reconstructed component volumes after performing unregularized XTT reconstruction (XTT→TV) is the second proposed method. Comparison of the results for both samples show that this method is also decreasing the noise level (as measured by MAD), while increasing CNR for different components, see Figure 11.14(D). However, it seems that this method retains a significant amount of noise, in particular in the background areas of both samples, see Figure 11.14.

In order to investigate the effect of regularization parameters, we provide more data points by showing the results for parameters β, which lead to the same noise level as estimated by MAD in Figure 11.15 for femur sample. In particular, for the estimated noise level of 0.040, which is reached by setting β to 80% in rXTT, this leads to β =87% for TV→XTT and β =84% for XTT→TV. For the estimated noise level of 0.005, this leads to β =97% for TV→XTT, β =89% for rXTT and β =95% for XTT→TV and for the estimated

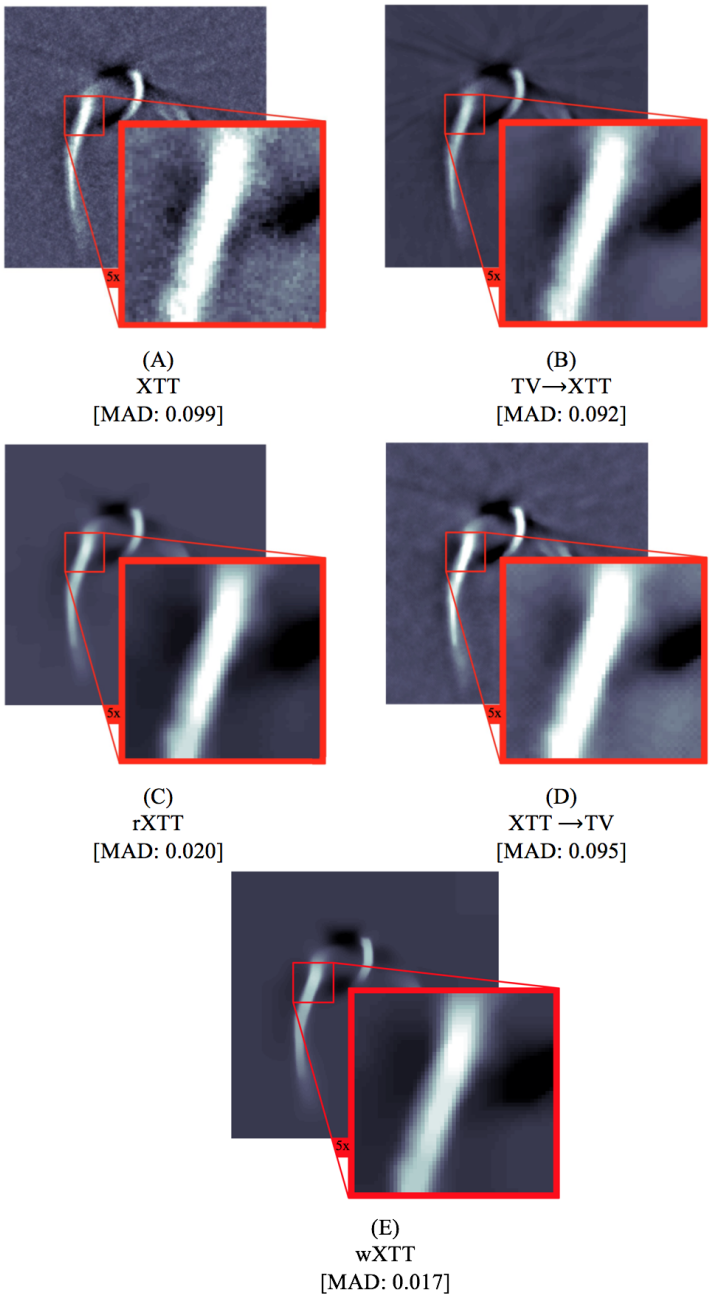

Figure 11.12.: Center slice of the reconstructed and denoised carbon knot dataset for component $\hat{\epsilon}_3 = [0, 0, 1]$. A ROI is marked with a red square and zoomed for the (A) XTT, (B) TV→XTT, (C) rXTT, (D) XTT→TV, and (E) wXTT methods. The parameter β was fixed to 80%. All images are windowed to [0.10,0.85].

noise level of 0.100, this leads to β =76% for TV→XTT, β =73% for rXTT and β =75% for XTT→TV.

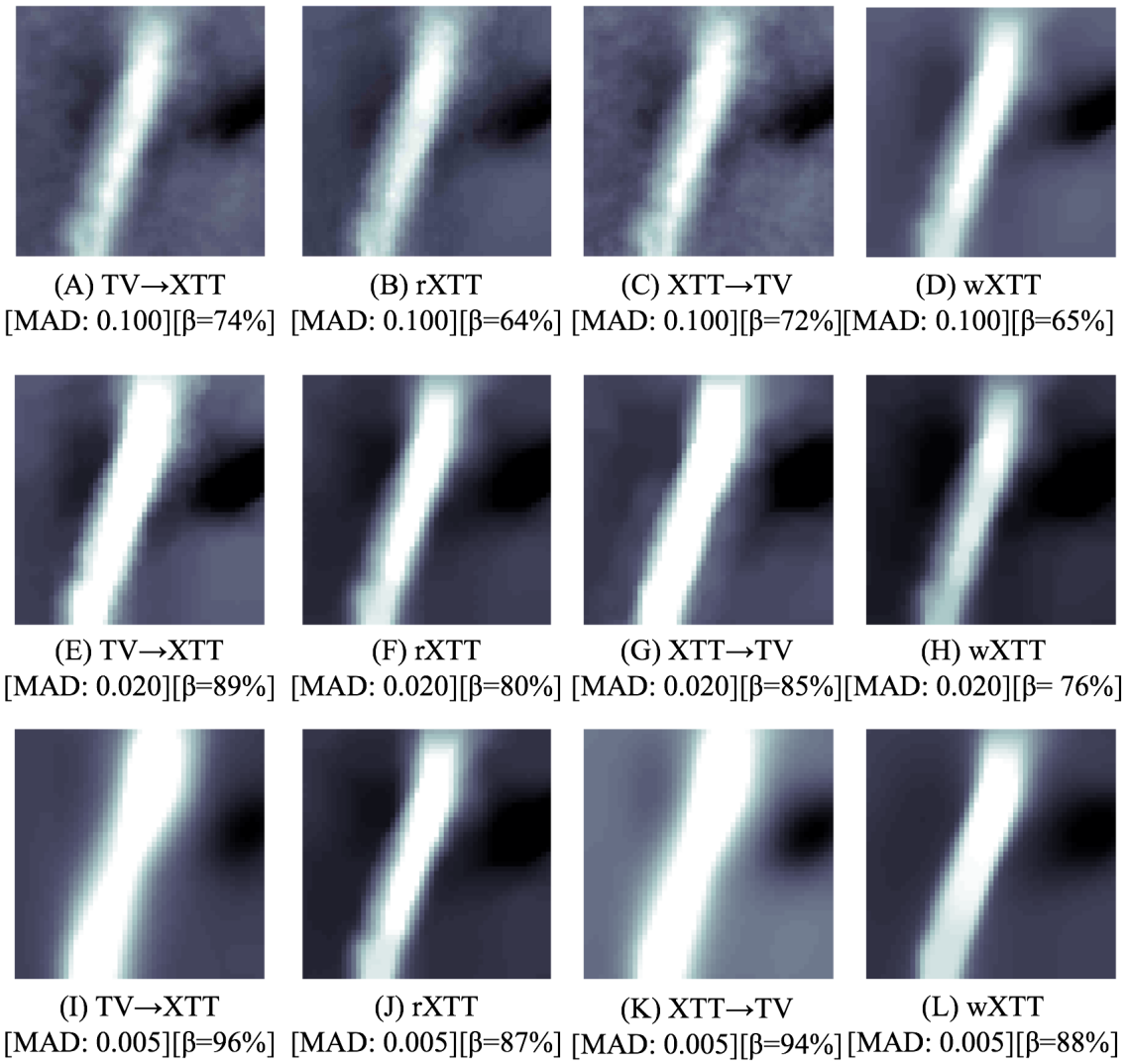

Figure 11.13.: Zoomed area of interest of the images (see Figure 11.12) of the carbon knot dataset corresponding to the scattering direction $\hat{\epsilon}_3$, windowed to [0.10,0.85]. The parameters β have been chosen such that the TV→XTT, rXTT and XTT→TV methods match in noise level as estimated by MAD. (A,E,I) TV→XTT, (B,F,J) rXTT, (C,G,K) XTT→TV, and (D,H,L) wXTT.

11.7.2.3 Components Quality Assessment

Illustration of MAD and CNR comparisons are shown in Figure 11.16, respectively, for the reconstructed components of the scattering directions $\hat{\epsilon}_1$, $\hat{\epsilon}_2$ and $\hat{\epsilon}_3$.

MAD and CNR comparisons for femur sample are shown in Figure 11.17, respectively, for the reconstructed components of the scattering directions $\hat{\epsilon}_1$, $\hat{\epsilon}_2$ and $\hat{\epsilon}_3$.

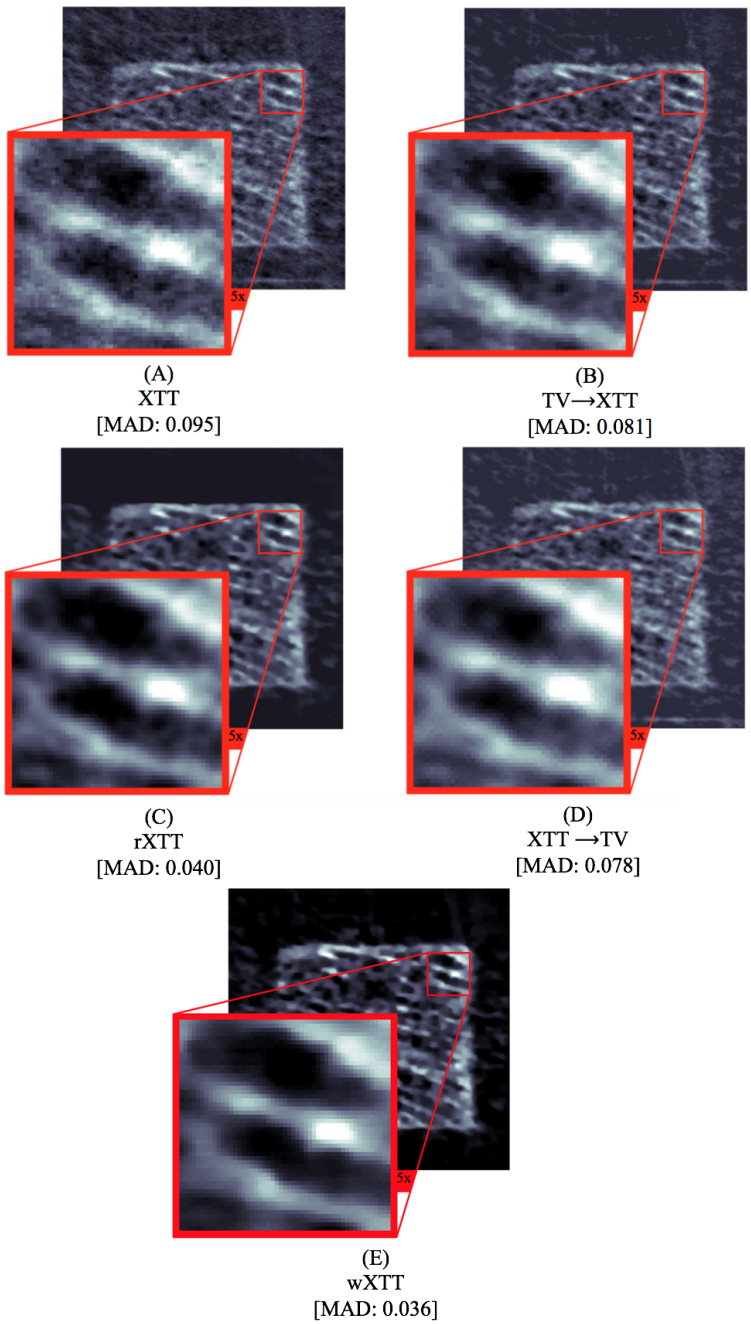

Figure 11.14.: Center slice of the reconstructed and denoised femur dataset for component $\hat{\epsilon}_1 = [1, 0, 0]$. A ROI is marked with a red square and zoomed for the (A) XTT, (B) TV→XTT, (C) rXTT, (D) XTT→TV, and (E) wXTT methods. The parameter β was fixed to 80%. All images are windowed to [0.05,0.80].

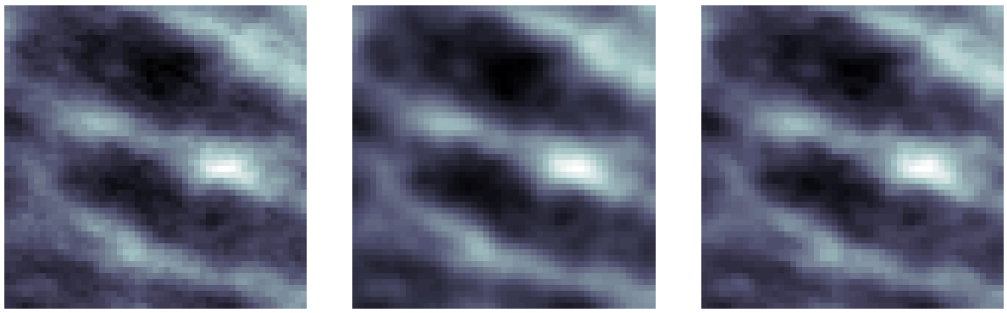

(A) TV→XTT
$[MAD : 0.100]$
$[\beta = 76\%]$

(B) rXTT
$[MAD : 0.100]$
$[\beta = 73\%]$

(C) XTT→TV
$[MAD : 0.100]$
$[\beta = 75\%]$

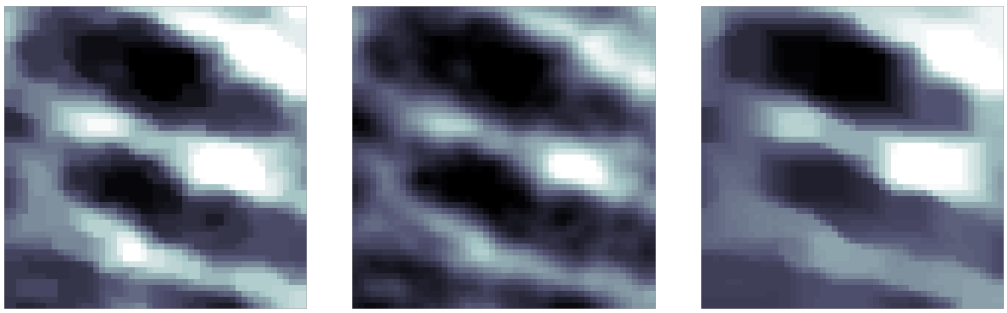

(D) TV→XTT
$[MAD : 0.040]$
$[\beta = 87\%]$

(E) rXTT
$[MAD : 0.040]$
$[\beta = 80\%]$

(F) XTT→TV
$[MAD : 0.040]$
$[\beta = 84\%]$

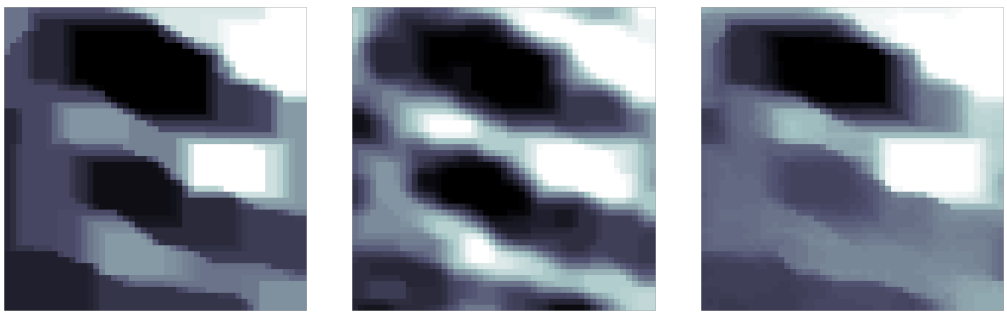

(G) TV→XTT
$[MAD : 0.005]$
$[\beta = 97\%]$

(H) rXTT
$[MAD : 0.005]$
$[\beta = 89\%]$

(I) XTT→TV
$[MAD : 0.005]$
$[\beta = 95\%]$

Figure 11.15.: Zoomed area of interest of the images (see Figure 11.14) of the femur dataset corresponding to the scattering direction $\hat{\epsilon}_1$, windowed to [0.05,0.80]. The parameters β have been chosen such that TV→XTT, rXTT and XTT→TV methods match in noise level as estimated by MAD. (A,D,G) TV→XTT, (B,E,H) rXTT, (C,F,I) XTT→TV

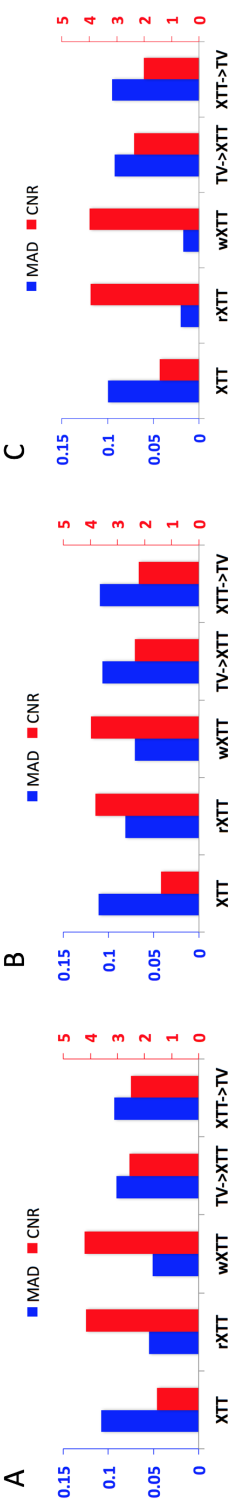

Figure 11.16.: MAD and CNR comparisons for different scattering directions (A) $\hat{\epsilon}_1$, (B) $\hat{\epsilon}_2$ and (C) $\hat{\epsilon}_3$ of the carbon knot reconstruction from Figure 11.12.

Figure 11.17.: MAD and CNR comparisons for different scattering directions (A) $\hat{\epsilon}_1$, (B) $\hat{\epsilon}_2$ and (C) $\hat{\epsilon}_3$ of the femur reconstruction from Figure 11.14.

11.7.2.4 Tensor Visualization

Figure 11.18 shows the center slice of the finally reconstructed tensors of carbon knot sample using all the scattering directions $\hat{\epsilon}_k$, visualized as tensors with the color encoding the main structure orientation (see orientation color coding sphere in the center of Figure 11.18).

Figure 11.19 shows the center slice of the finally reconstructed tensors of femur sample using all the scattering directions $\hat{\epsilon}_k$, visualized as tensors with the color encoding the main structure orientation (see orientation color coding sphere in the center of Figure 11.19).

11.7.2.5 Numerical Behavior

In order to study the convergence of proposed methods, a comparison of $r^{(q)}$ and $\Delta^{(q)}$ plots for the proposed methods was shown in Figure 11.20. The TV→XTT and XTT methods show smaller residual norm $r^{(q)}$, but oscillating behavior in update $\Delta^{(q)}$, while rXTT and wXTT methods shows a larger residual norm and smoother updates. The rXTT and wXTT methods have been shown to produce considerably less noise artifact and visually smoother, non-oscillating updates.

11.7.2.6 Tensor Orientation Evaluation

One of the limitations in XTT imaging assessment is the lack of any XTT ground truth phantom to evaluate the proposed reconstruction and image denoising methods. However, In order to evaluate the XTT reconstruction and noise reduction methods proposed in this paper, we introduced an approach based on the using of attenuation images as a standard ground truth.

Figure 11.21(A,B) shows a histogram comparison of the angular differences δ of the fiber orientations for regular XTT and the two proposed methods rXTT and wXTT. A corresponding box plot is shown in Figure 11.21(C,D). As shown in this figure, comparison between the orientation information acquired from XTT reconstruction and noise reduction methods shows fairly small angles of deviations δ's to the centerline orientation of attenuation image while the proposed rXTT method exposes smaller deviations comparing to the other methods.

11.8 Conclusion

In this chapter, we studied the best way to incorporate a denoising technique into the XTT reconstruction pipeline, in particular the popular total variation denoising technique. We proposed two different schemes of including denoising into the reconstruction process, one using a column block-parallel iterative scheme and one using a whole-system approach. Additionally, we compared results using a simple denoising approach, applied either before or after reconstruction. As shown in the experiments and corresponding results, all proposed methods show marked improvements in noise reduction for both of our experimental datasets.

In order to study the convergence speed of the proposed methods, a comparison of $r^{(q)}$ and $\Delta^{(q)}$ plots was shown in Figure 11.20. The TV→XTT and XTT methods show smaller

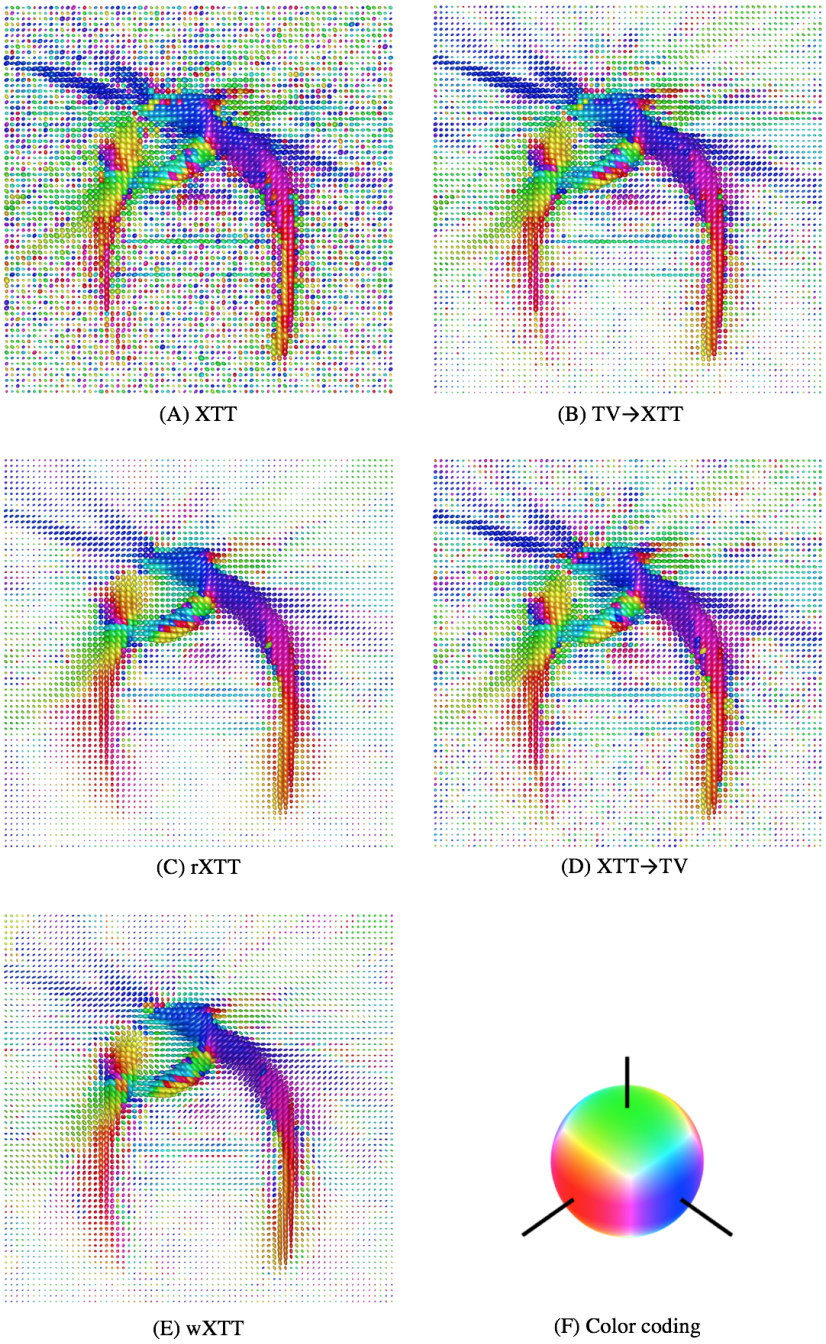

Figure 11.18.: Tensor visualization of a single slice of the reconstructed carbon knot sample volumes for all four methods: (A) XTT (B) TV→XTT, (C) rXTT, (D) XTT→TV, (E) wXTT and (F) The structure orientation is color encoded as shown in orientation sphere. β fixed to 80%.

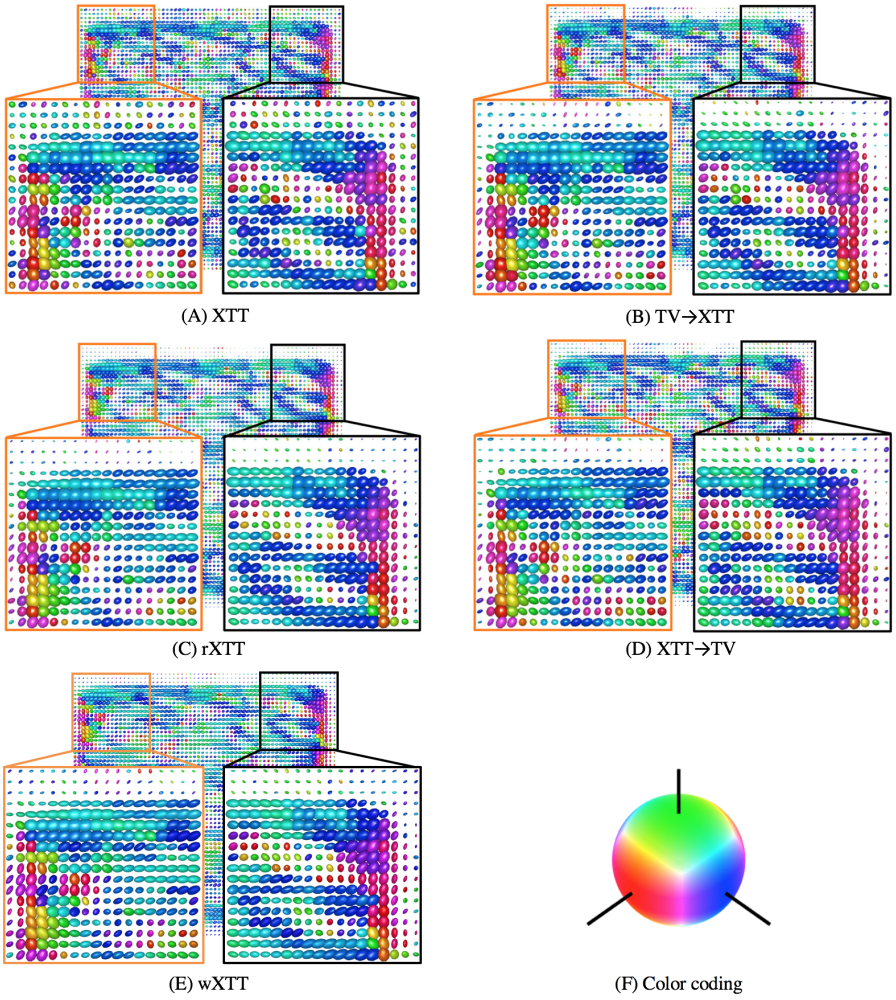

Figure 11.19.: Tensor visualization of a single slice of the reconstructed femur sample for all four methods: (A) XTT, (B) TV→XTT, (C) rXTT, (D) XTT→TV, (E) wXTT and (F) The structure orientation is color encoded as shown in orientation sphere. β fixed to 80%.

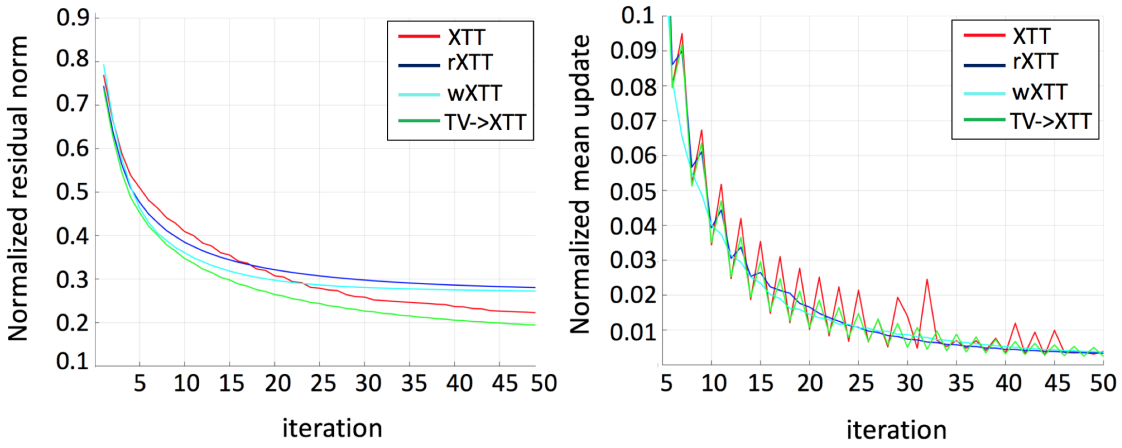

(A) Residual norm $r^{(q)}$ (B) Update $\Delta^{(q)}$

Figure 11.20.: Illustration of diagrams for (A) normalized residual norm $r^{(q)}$ and (B) normalized mean update $r^{(q)}$ for the proposed methods. Normalized mean horizontal axis is shown from iteration 5 to illustrate the difference between different plots.

residual norm $r^{(q)}$, but oscillating behavior in update $\Delta^{(q)}$, while the rXTT and wXTT methods show a larger residual norm and smoother updates.

One of the limitations in XTT imaging assessment is the lack of any XTT ground truth to evaluate the proposed reconstruction and image denoising methods. However, in order to evaluate the XTT reconstruction and noise reduction methods proposed in this paper, we introduced an approach based on the absorption images in place of a ground truth. As shown in Figure 10.1, the comparison between the fiber orientations acquired from the XTT reconstruction and noise reduction methods shows fairly small angles of deviations δ compared to the centerline orientation of absorption image, while both proposed rXTT and wXTT methods demonstrate even smaller deviations.

Both regularized XTT reconstruction (rXTT) and whole-system regularized XTT reconstruction (wXTT) methods show promising results for both datasets by reducing noise level and improving CNR compared to all other approaches, as seen in all the results. In particular, as shown in Figure 11.14 for the femur sample, the background noise is reduced significantly using rXTT and wXTT, and the zoomed image of Figure 11.14(A-E) illustrates a successful preservation of trabecular tissue edges in the sample. For the carbon knot sample, the rXTT and wXTT methods are significantly reducing the background noise and dampens streak artifacts, as shown in Figure 11.12(A-E).

For projection domain noise reduction (TV→XTT), the noise level has been measured in terms of MAD and SNR and shows a significant improvement for each of the dark-field images. Reconstruction using the denoised dark-field images, instead of the original ones, shows qualitative and quantitative improvements in the reconstructed volumes, as shown in Figures 11.12(D) and 11.14(D). However, the TV→XTT approach requires a fairly high regularization parameter in order to compete with the rXTT method in terms of CNR and MAD, which results in flattened features that are indistinguishable from noise as shown in Figure 11.12. This can also lead to amplified streaking artifacts, as can be seen in Figure 11.12(B).

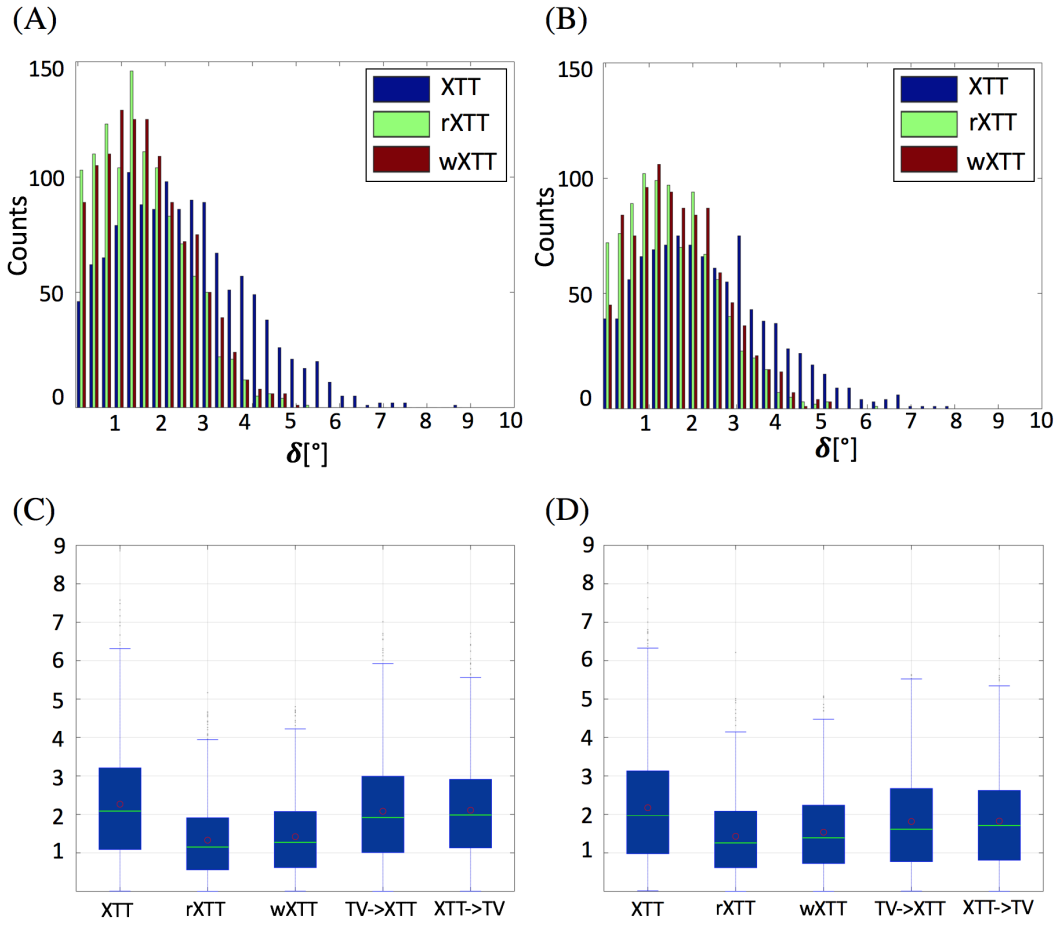

Figure 11.21.: Histogram showing angle differences δ comparison of attenuation reconstructed image with XTT reconstruction method and proposed noise reduction and regularization methods for ROI1 (A) and ROI2 (B). Box plots illustrating the distribution of data from all proposed reconstruction and denoising methods with green line and red circle marks showing the median and mean for (C) ROI1 and (D) ROI2, as marked in Figure 10.1.

Comparison of the results for both samples reconstructed and denoised using the denoising of reconstructed volumes method (XTT→TV), shows significant decrease in the noise level (as measured by MAD) and increasing CNR for different components, see Figures 11.12(D) and 11.14(D). However, it seems that this method retains a significant amount of noise, in particular in the background areas of both samples, see Figures 11.12 and 11.14.

In order to investigate the effect of the regularization parameter, we provide more data points by showing the results for parameters β, which lead to the same noise level as estimated by MAD in Figure 11.13 for carbon knot samples respectively.

As future work, it would be valuable to investigate the proposed methods using other samples with different characteristics and also using more advanced evaluation methods, such as a model-observer evaluation pipelines. Instead of using TV denoising, adapting the denoising method to a more exact noise model of the dark-field signal as acquired from a grating-based interferometry setup should yield further improvements in the

resulting image quality. The adapted denoising method could then be integrated into the XTT reconstruction pipeline in the same way as suggested in this work for the TV denoising method.

In summary, we have investigated several ways of incorporating a denoising approach into the XTT reconstruction technique. In particular, we studied a component-based regularized reconstruction technique, interleaving denoising with the regular block-parallel XTT reconstruction step in each iteration (rXTT), as well as a whole-system approach using regularization directly (wXTT). The results of the conducted experiments show a marked improvement in noise reduction for both experimental datasets, both qualitatively and quantitatively, for all methods, when compared to the unregularized XTT reconstruction technique. The two proposed approaches incorporating denoising into the reconstruction process, rXTT and wXTT, perform markedly better than the simple denoising of the raw dark-field images (TV$\rightarrow$XTT) or the reconstructed component images (XTT$\rightarrow$TV), with very slight advantages for the wXTT approach.

Part III.

CT PERFUSION IMAGING

12. CT Perfusion Imaging of the Liver

12.1 Overview

This chapter will provide an overview of CT perfusion (CTP) imaging and its applications for liver imaging. First, a theoretical overview of the CTP data acquisition will be presented in section 12.3. Next, in section 12.4, the forward model will be introduced. In section 12.5, we provide a review of several existing tomographic reconstruction techniques for CTP imaging and finally, will explain perfusion data analysis techniques in section 12.6.

12.2 Background

CT perfusion (CTP) is a functional imaging modality that requires the acquisition of a baseline image before injection of any contrast enhancement which will be followed by a series of images acquired as a function of time following an intravenous bolus injection of a conventional iodinated CT contrast material [Mil02; MG03b]. Thus, the temporal changes in contrast enhancement effectively provide a time–attenuation curve (TAC) , which can be analysed to quantify a range of parameters such as tissue blood-flow parameters that indicate the functional status of the vascular system within tumors and adjacent tissues [May00; MEK07; Jai08]. Typically, an iodinated contrast agent is administered and projection images are acquired before, during, and after the injection of contrast to track temporal changes in CT attenuation [Gil01]. (see Figure 12.1)

With the availability of wide-area detectors (e.g. 256 slices or more), CT can cover whole organs which has facilitated CTP in a variety of applications including head and neck, liver, lung and colorectal imaging [Mil12; MG03a]. CTP has shown remarkable results in diagnosing malignant and non-malignant parotid lesions [Bis07] and in assessing tumor vascularity changes that result from chemotherapy and radiation therapy [Sah07].

Liver CT perfusion provides valuable information on blood flow dynamics in the assessment of liver damage or severity of hepatic fibrosis in patients with chronic liver disease'[Has06], in the evaluation of therapeutic effectiveness for liver cancer [KKW14], and in the assessment of hepatic perfusion changes after surgical and radiological interventions [Qia10; Wei05]. Recent studies also revealed promising results of using CTP as a viable biomarker for of hepatocellular carcinoma (HCC) tumor and pancreatic lesion detection and analysis [Sah07; Ipp12].

12.3 Acquisition

Several data acquisition protocols have been proposed for CTP imaging. In this study, however, we use a similar protocol to the animal model with denser sampling at the beginning of the sequence [Bui11].

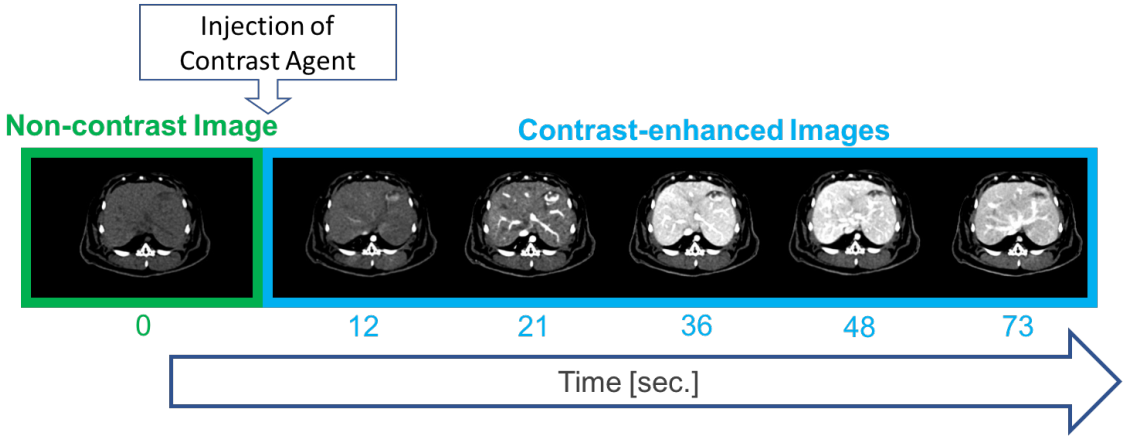

Figure 12.1.: An illustration of the dynamic enhanced CT perfusion imaging. Sequential CT scanning of the same tissue (rabbit abdomen in this figure) have been acquired before, during, and after injection of contrast to track temporal attenuation changes.

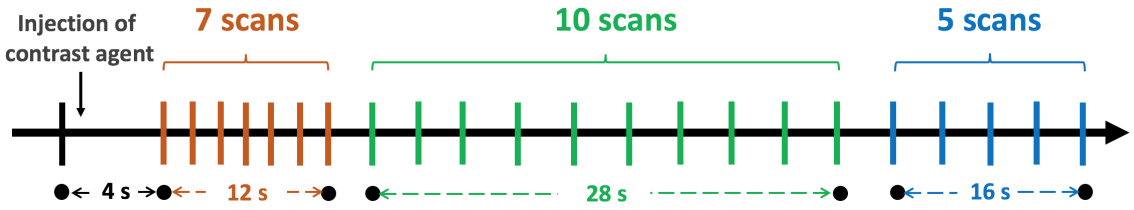

Figure 12.2.: Temporal sampling in the CT perfusion study.

The exact sampling pattern is shown in Figure Figure 12.2 starting with an initial non-enhanced scan followed by a 4 sec delay and 7 scans over 12 sec, a 6 sec delay followed by 8 scans over 28 sec, a 5 sec delay, and finally 5 scans over 16 sec.

12.4 Forward Model

We adopt a simple monoenergetic forward model for our experiments. The mean measurements in this transmission tomography model can be written as,

$$\bar{y}_i = I_0.exp(-[A\mu(t)]_i), \tag{12.1}$$

where I_0 is a gain term associated with the unattenuated x-ray fluence for each measurement. The patient anatomy (at a single time point) is denoted by the vector μ. We presume an ideal detector so that the random vector y is independent and Poisson distributed. The projection operation is denoted by A and $[A\mu]_i$ is the line integral associated with the i^{th} measurement.

12.5 Reconstruction

In this section, we discuss two different reconstruction methods that are applied to the data. These methods are outlined in the following sections.

12.5.1 Feldkamp–Davis–Kress Reconstruction

For a baseline analytic reconstruction, we used the Feldkamp–Davis–Kress (FDK) algorithm [FDK84] which is a commonly used method for direct CT reconstruction. Data was prepared using ideal gain correction, logarithmic transformation, and thresholding of the data at 10^{-4}. The reconstruction filter used for this approach was a raised cosine ramp function filter with a cutoff frequency of 0.8 times Nyquist.

12.5.2 Penalized-Likelihood Reconstruction

To investigated performance using a well-known MBIR approach we adopted a penalized-likelihood estimator [Fes00]. The objective function for this reconstruction may be written as

$$\phi(\mu; y) = -L(\mu; y) + \beta \|\psi_\mu\|, \tag{12.2}$$

where L represents the log-likelihood function which is derived using the Poisson likelihood assumption and a data model matching. The second term is a traditional edge-preserving roughness penalty term. The operator denotes a local pairwise voxel difference operator and, in this work, we will choose to implement using a Huber cost function [Hub64]. The regularization parameter controls the balance between the data fidelity and roughness penalty allowing user control of the noise-resolution trade-off. The optimization problem can be written as,

$$\mu_\Delta = \underset{\mu \in \mathbb{R}^{N_\mu}}{\operatorname{argmin}} \, \phi(\mu; y). \tag{12.3}$$

We solve this objective iteratively using the separable quadratic surrogates approach [EF99b] using 100 iterations and 10 subsets.

12.5.3 Prior Image Penalized-Likelihood Estimation (PIPLE)

To investigate performance using a prior image based MBIR approach we implemented a PIPLE as described in [Sta13] which has the following objective function

$$\phi(\mu; y) = -L(\mu; y) + \beta_R \|\psi\mu\| + \beta_P \|\mu - \mu_P\|, \tag{12.4}$$

with the same log-likelihood function and traditional roughness penalty as 12.2. The third term is a prior image penalty with denoting the prior image. The parameters β_R and β_P denote the relative strengths of the roughness and prior image penalty respectively. The optimization has the same form as 12.3 and is solved using the separable quadratic surrogates (SPS) algorithm [EF99b]. For PIPLE, 100 iterations and 10 subsets were used.

12.6 Hepatic Perfusion Analysis

We use the dual-input maximum slope method [Mil91; MHD93b] to calculate the perfusion metrics for both the baseline truth as well as processed data. The slope method is commonly used in the evaluation of dual liver blood supply components, i.e. hepatic arterial perfusion (HAP) and hepatic portal perfusion (HPP) (see Figure 12.3).

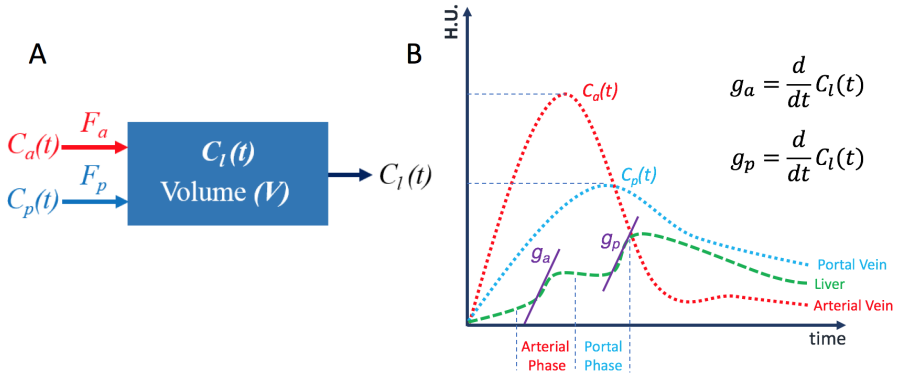

Figure 12.3.: Hepatic perfusion analysis, (A) Dual input liver perfusion model, and (B) Dual-input maximum slope method based on the equation for measurement of tissue perfusion, $C_a(t)$, $C_p(t)$ and $C_l(t)$ denote the concentration in aorta, portal vein and liver respectively where $C_l(t) = C_a(t) + C_p(t)$.

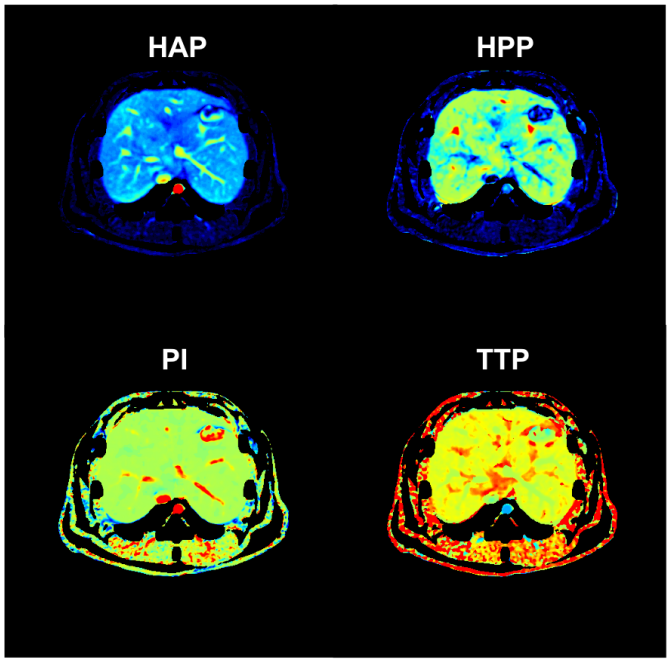

Figure 12.4.: Perfusion maps (HAP, HPP, PI and TTP) visualization for the rabbit's abdomen and liver acquired for the CT scans from Figure 12.1 with acquisition protocol of Figure 12.2.

The HAP was determined as the peak gradient of the hepatic TAC before the peak splenic attenuation (arterial phase) divided by the peak aortic attenuation. (Portal perfusion) presumed to be negligible during the arterial phase.) Thus,

$$HPP = \frac{F_a}{V} = \frac{\frac{dC_l(t)}{dt}_{max}}{C_a(t)_{max_{max}}}, \tag{12.5}$$

HPP was calculated by dividing the peak gradient of the hepatic TAC after the peak

splenic attenuation portal phase () by the peak portal vein attenuation as,

$$HPP = \frac{F_p}{V} = \frac{\frac{dC_l(t)}{dt}_{max}}{C_p(t)_{max}{}_{max}}, \tag{12.6}$$

where F_a and F_p denote the arterial and portal flows and $C_a(t)$, $C_p(t)$ and $C_l(t)$ refer to the concentration in aorta, portal vein and liver respectively ($C_l(t) = C_a(t) + C_p(t)$). Another common metric, the arterial fraction, or hepatic perfusion index (PI; %), was determined as,

$$PI = \frac{HAP + HPP}{HAP}. \tag{12.7}$$

The perfusion index is commonly used since it is less sensitive to some biases present in the HAP and HPP estimates. Note that in Figure 13.2, the tumor enhances more in the arterial phase than healthy tissue providing an important diagnostic cue.

Lastly, we also compute the time-to-peak (TTP) by identifying the maximum value in the TAC and recording the time to achieve that value since the injection. The TTP metric has previously been used in stroke imaging [May00], but may also provide an additional diagnostic test for identification of lesions in the liver.

Figure 12.4 illustrates an example perfusion maps obtained from reconstructed rabbit liver data.

13. Low-dose CT Perfusion Imaging

13.1 Overview

Our aim in this chapter is to describe low-dose CT perfusion (CTP) imaging and to introduce its applications in liver imaging scenarios. Next, we will provide an overview of the data generation in section 13.3. Then, a detailed discussions on the phantom design and proposed reconstruction method to reduce the radiation dose in CTP exams follows in sections 13.4 and 13.5 respectively. Next, in section 13.6, several experiments will be introduced and the corresponding results will be illustrated in section 13.7.

13.2 Background

CT perfusion imaging of the liver enables the evaluation of perfusion metrics that can reveal hepatic diseases and that can be used to assess treatment responses. Despite the potential clinical applications of the CTP, the excessive radiation dose exposed during the sequential scanning is a major drawback that limits more widespread use of CTP in clinical and research applications [Pan05; Ogu14]. Several techniques have been studied to decrease the radiation exposures including patient-size-specific scanning parameter modifications and variation of exposure throughout the temporal scanning [Mur05; OKM11; Che09; Li14]. However, lowering x-ray exposure, inevitably reduces the quality of the acquired images and can introduce noise and streak artifacts which, in turn, lowering the accuracy of the desired perfusion parameters.

Model-based iterative reconstruction (MBIR) techniques have been proposed as one of the solutions to improve the trade-off between radiation dose and acquired image quality. Recent studies on body CT scanning have demonstrated that such advanced processing methods can improve image quality in a low exposure scan, thereby reducing the effective dose exposed to the patient [Vor11; Har09]. Recent study of Negi et al. [Neg12] demonstrated that the adaptive iterative dose reduction (AIDR) reduced the image noise while maintaining hepatic perfusion parameters. However, most reconstruction methods tend to be applied in isolation, neglecting the large amount of shared information between scans.

In contrast, prior-image-based reconstruction (PIBR) approaches have been proposed to incorporate anatomical information found in previous scans. Prior information is much stronger than traditional assumptions of image smoothness and should allow for further reductions of noise and artifacts comparing to conventional MBIR regularization.

Example PIBR methods include prior-image-constrained compressed sensing () [CTL08b] and prior-image-registered penalized-likelihood estimation (PIRPLE) [Sta13]. Both of these techniques use a high quality prior image volume to help reconstruct low exposure or sparsely sampled projection data. PICCS has previously been investigated for small animal CTP [Net10]. A modification of PIRPLE with deformable registration

has been used to reduce x-ray exposures in lung nodule surveillance by more than an order of magnitude [Dan14]. Recently, Pourmorteza *et al*. [Pou16] proposed a novel Reconstruction of Difference (RoD) technique that uses a penalized likelihood objective to directly reconstruct the difference between an already scanned prior image and the current anatomy enabling direct reconstructions of anatomical change (analogous to digital sub- traction angiography) with reduced noise.

In this study, we investigate the feasibility of using RoD technique for liver CTP by providing a digital simulations based on real time activity data and introduce several evaluation and perfusion analysis techniques [Sey18a]. An illustration of the proposed acquisition and processing chain for liver CTP is shown in Figure 13.1.

Tomographic measurements (y_n) are acquired over a range of time points $n = 0$ to N. These measurements cover a changing anatomy (μ_n) from an unenhanced volume (pre-iodine-injection) at $n = 0$, through uptake and washout of the contrast. A high-quality unenhanced baseline image (μ_0) serves as a prior image (μ_p) for input into RoD to reconstruct difference image volumes ($\hat{\mu}_\Delta$) for all subsequent low-dose sequential data. These difference images can be used to form estimates of the current image anatomy ($\hat{\mu} = \mu_p + \hat{\mu}_\Delta$) at each time point. Subsequent perfusion analysis using standard computations on the entire image sequence is then used to create perfusion maps using various metrics.

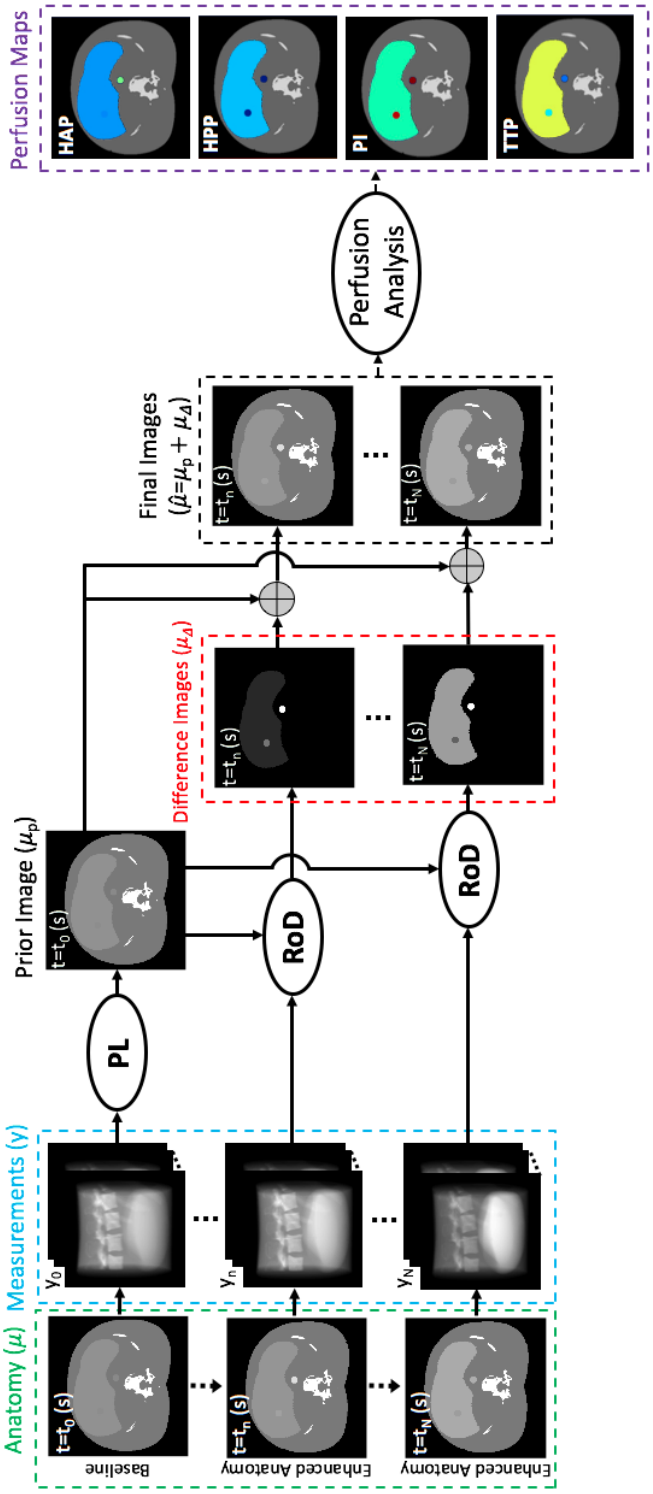

Figure 13.1.: Flowchart showing the acquisition, reconstruction and analysis chain for CT perfusion using RoD. Differences for each time point in the series are reconstructed relative to a high-quality non-contrast-enhanced baseline image. Estimates of the current anatomy may be formed by adding back the prior image, and subsequent perfusion analysis is applied to generate standard perfusion maps using different metrics.

13.3 Data Generation

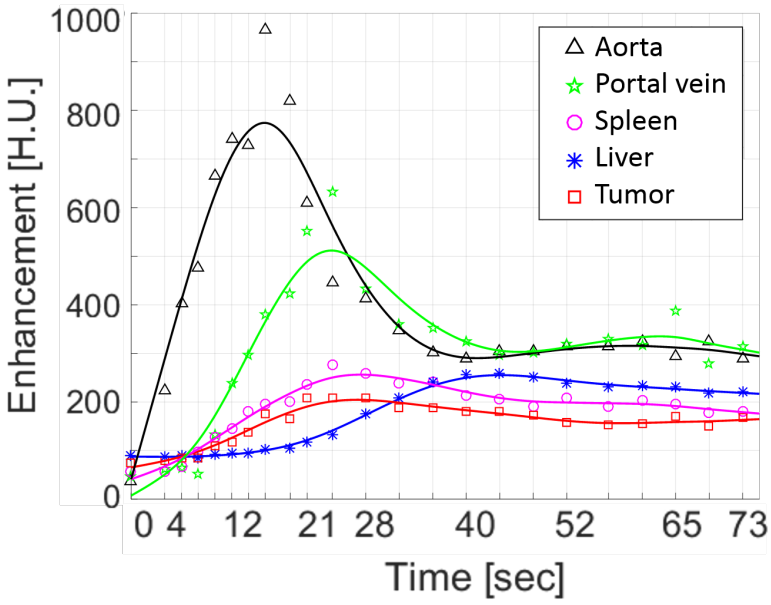

Figure 13.2.: TACs obtained from an abdominal scan of a rabbit animal model with HCC are obtained using a smooth fit to attenuation values at individual time points. A region of interest in five tissue types allowed estimation of TACs for the aorta, portal vein, spleen, healthy liver tissue, and a liver tumor.

For this study, we obtained realistic time-attenuation curves (TACs) from an animal model. Specifically, an adult male New Zealand white rabbit (3.5 kg) was selected for the study. The animal was implanted with a VX2 tumor in the left lobe of the liver using previously documented procedures [Che04; Bui11] and allowed to grow for 13-15 days prior to CTP imaging. The rabbit was sedated using ketamine (20 mg/kg) and xylazine (8 mg/kg) via intramuscular injection. CTP studies were acquired using an Aquilion ONE (Toshiba, Japan) 320-slice CT scanner with a 22 cm field-of-view and x-ray technique of 120 kVp and 80 mA. Contrast agent (1.5 ml/kg, 320 I/ml Visipaque, GE Healthcare, Princeton, NJ) was administered at 1 ml/second via a marginal ear vein followed by a 7 ml saline flush at 1 ml/second. Following a 6 sec delay, CT data was acquired at 2-sec intervals for 25 seconds, followed by 3-second intervals for 42 seconds. Each scan took 0.5 seconds for a total of 17.5 seconds of scan time (CTDIvol = 164.7 mGy). CT reconstruction was performed using AIDR 3D (Toshiba Medical Systems, Japan) with 0.349 mm voxels. In order to compensate for breathing motion, CT dataset were registered using Body Registration (Toshiba Medical Systems, Tochigi, Japan).

Regions-of-interest (ROI) were identified within the aorta, portal vein, spleen, healthy liver tissue, and the liver tumor. Attenuation was averaged over the region to form raw TAC samples. A smoothing spline function [Uns99; DAn10] was used to fit the liver perfusion TACs to reduce noise in the estimates. The resulting TACs for each region are shown in Figure 13.2.

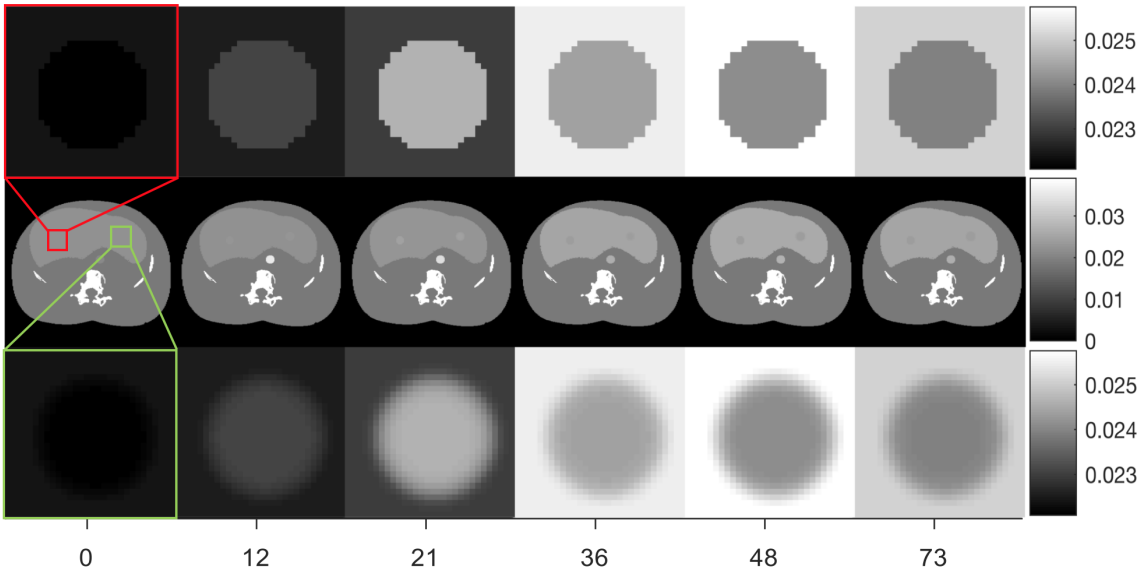

Figure 13.3.: 4D Digital liver phantom with two lesions designed for CT perfusion studies. Single slices and a zoomed region around both simulated homogeneous tumor (marked in red) and Gaussian tumor (marked in green) are shown for six time points in the sequence.

13.4 Phantom Design

To assess the performance of proposed methods in human CTP, TACs from Figure 13.2 were mapped onto a digital anthropomorphic phantom and two simulated spherical tumors were included afterwards.

Designed phantom covers an axial extent of 20.48 cm and includes two simulated spherical tumor based on the same tumor TAC. The homogeneous lesion with a diameter equal to 12 mm and a sharp edge profile is marked red in Figure 13.3). Second simulated tumor (marked green in Figure 13.3) has flat interior profile with a smooth edge based on a Gaussian profile. Both lesions have the same full-width half-maximum of 3.2 mm.

An illustration of dynamic digital liver phantom with two lesions is shown in Figure 13.3 for several time points.

Specifically, the healthy liver TAC was mapped onto the segmented liver, the aorta TAC was mapped onto the aorta, and a simulated spherical tumors were created using the tumor TAC.

Temporal sampling for data generation followed a similar protocol as that used in the animal model with denser sampling at the beginning of the sequence. The exact sampling pattern was shown in Figure Figure 12.2 starting with an initial non-enhanced scan followed by a 4 sec delay and 7 scans over 12 sec, a 6 sec delay followed by 8 scans over 28 sec, a 5 sec delay, and finally 5 scans over 16 sec.

13.5 Reconstruction of Difference

Reconstruction of Difference (RoD) algorithm aims to reconstruct the difference image (μ_Δ) between the current anatomy (μ) and a prior image (μ_p). In CT perfusion imaging,

RoD can be employed to reconstruct contrast changes as the difference image between the unenhanced baseline (as a prior image) and individual enhanced images of the same anatomy post-contrast-injection. Under the RoD model

$$\mu = \mu_p + \mu_\Delta. \tag{13.1}$$

Plugging into the forward model in Equation 12.1 yields,

$$y = [I_0.exp(-A\mu_p)].exp(-A\mu_\Delta) = g.exp(-A\mu_\Delta), \tag{13.2}$$

where g denotes a new "gain" parameter that includes μ_p. Thus the forward model has a familiar form (same as 12.1) and it is straightforward to write a penalized-likelihood objective function for estimation of the difference image, μ_Δ, as,

$$\phi(\mu_\Delta; y, \mu_p) = -L(\mu_\Delta; y, \mu_p) + \beta_R \|\psi_{\mu_\Delta}\| + \beta_M \|\mu_\Delta\|, \tag{13.3}$$

where the log-likelihood function is denoted with L. Two penalty terms are included: 1) an edge-preserving roughness penalty term which encourages the smoothness in the difference image and controlled by a regularization parameter β_R. (denotes a local pairwise voxel difference operator.) And, 2) a magnitude penalty on μ_Δ which encourages sparseness of the difference image controlled by parameter β_M. The second penalty term also controls the amount of prior information integrated from the unenhanced baseline image since increased sparsity of the change image implies increased similarity to the prior image.

The optimization problem for the image volume updates can be written as,

$$\begin{aligned} \mu_\Delta &= \arg\min_{\mu_\Delta} \phi(\mu_\Delta; y, \mu_p) \\ &= \arg\min_{\mu_\Delta} \{-L(\mu_\Delta; y, \mu_p) + \beta_R \|\psi_{\mu_\Delta}\| + \beta_M \|\mu_\Delta\|\} \end{aligned} \tag{13.4}$$

We solve the optimization problem for μ_Δ using separable paraboloidal surrogates (SPS) algorithm [EF99b] with 100 iterations and 10 subsets.

All reconstruction methods and evaluation routines were implemented in Matlab (The Mathworks, Natick, MA) with projectors/back-projectors in C/C++ using CUDA libraries for acceleration.

13.6 Experiments

All experiments used a common CT geometry. Table 13.1 summarizes the simulated system parameters. Projection data used the separable footprints projector [LFB10].

13.6.1 Regularization Investigation

13.6.1.1 Penalized-Likelihood Regularization

While PL reconstruction is widely used in CT, we are unaware of previous attempts to optimize regularization as a function of time throughout a contrast-enhanced study. To study general trends in optimal penalty strength for PL, we performed an exhaustive

Table 13.1.: Simulation parameters used for liver CTP studies.

Quantity	Value
Rotation Angle	360 degrees
Volume Size	$512 \times 512 \times 64$
Voxel Size	0.4 mm
Number of Projections	360
Source-to-Axis Distance	1000 mm
Source-to-Detector Distance	500 mm
Detector Pixel Size	$1mm \times 1mm$

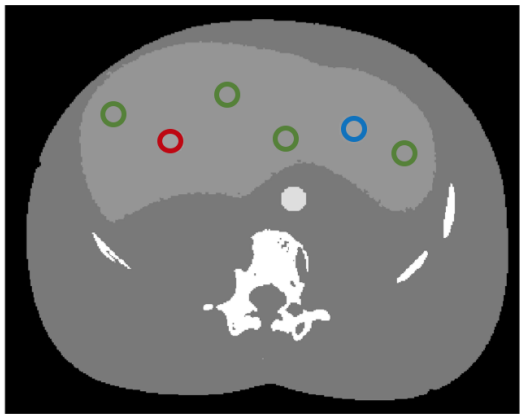

Figure 13.4.: ROIs for TAC and perfusion RMSE calculation. The ROI for the homogeneous and Gaussian tumors are marked in red and blue respectively and healthy liver tissue is marked with green circles.

1D search to find the optimal regularization parameter by comparing the root-mean-square error (RMSE) between the original image and the PL reconstructed image. We repeated this search for each time point. The incident fluence was fixed to $I_0 = 10^3$ for all experiments. RMSE was calculated in a 50×50 voxel ROI including the lesion and liver tissue around it (as illustrated in Figure 13.3).

13.6.1.2 Prior-Image Penalized-Likelihood Regularization

The PIPLE objective function includes two coefficients, β_R and β_P, which control the strength of the roughness and prior magnitude penalty, respectively. To study the optimal penalty strength, we performed an exhaustive 2D sweep of these parameters. Optimal parameters based on the RMSE around a region-of-interest (ROI), shown in Figure **??**) including the simulated tumor were selected for each time point in the temporal sequence.

13.6.1.3 Reconstruction of Difference Regularization

The RoD objective function includes two coefficients, β_R and β_M, which control the strength of the roughness and prior magnitude penalty, respectively. Similar to PIPLE optimization, we performed an exhaustive 2D sweep of these parameters to study the optimal penalty strength. Optimal parameters based on the RMSE around a region-of-

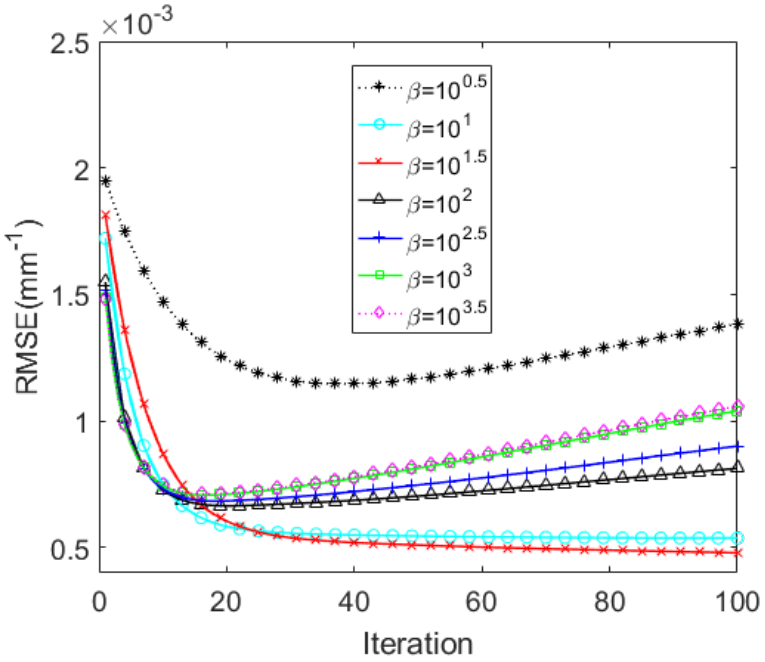

Figure 13.5.: Illustration of penalized-likelihood regularization parameter optimization using root-mean-square error (RMSE) change between iterations.

interest (ROI), shown in Figure 13.4) including the simulated tumor were selected for each time point in the temporal sequence.

13.6.2 Incident Fluence Investigation

To study the performance of RoD under different exposure conditions, we simulated different levels of Poisson noise for noisy measurements with fluence ranging from $I_0 = 5 \times 10^3$ to 10^5 (photons per pixel) in each of the time points. The prior image for RoD was produced by PL reconstruction of the $t = 0$ (unenhanced image volume) using $I_0 = 5 \times 10^3$ photons.

13.6.3 Time-Attenuation Curves

To study perfusion accuracy we conduct an analysis of TAC accuracy. For this study, TACs are reproduced for each reconstruction approach by averaging over healthy and tumor ROIs (shown in Figure 13.4). Errors are computed for each time point. RMSE is also computed for healthy liver and tumor ROI.

To consider the effects of noise, five different noise realizations were generated and reconstructed for all comparisons. Standard deviations over noise realizations were computed for each time point to place error bars on TAC estimate curves and their corresponding RMSE plots.

13.6.4 Perfusion Analysis

Another study conducted to investigate the perfusion accuracy of each approach is to assess perfusion metric accuracy. For this study, the four different perfusion metrics iden-

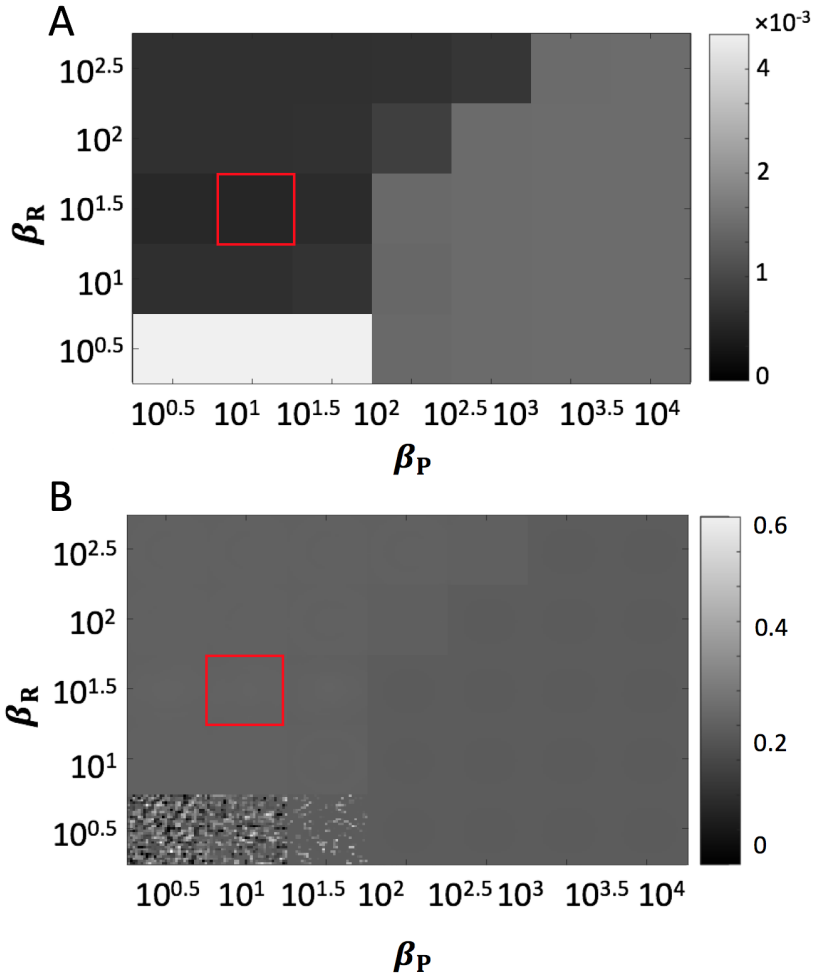

Figure 13.6.: Illustration of PIPLE regularization investigation for $I_0 = 10^3$ and $t = 21s$. (A) Regional RMSE as a function of both penalty coefficients β_R and β_P evaluated at a $10^{0.5}$ interval and (B) a zoomed ROI showing reconstructions μ associated with each regularization parameter pair. the red box denotes the optimal values.

tified previously are computed to form perfusion maps for each approach. Corresponding RMSE is also computed for healthy liver and tumor ROI.

To consider the effects of noise, five different noise realizations were generated and reconstructed for all comparisons and computed standard deviations over noise realizations were computed for the RMSE plots of the perfusion maps.

13.7 Results

13.7.1 Regularization Investigation

In this section, we will provide the results for investigation of the regularization parameter optimization for all iterative reconstruction approaches. Several plots and figures will be illustrated to show the best parameter selection procedure.

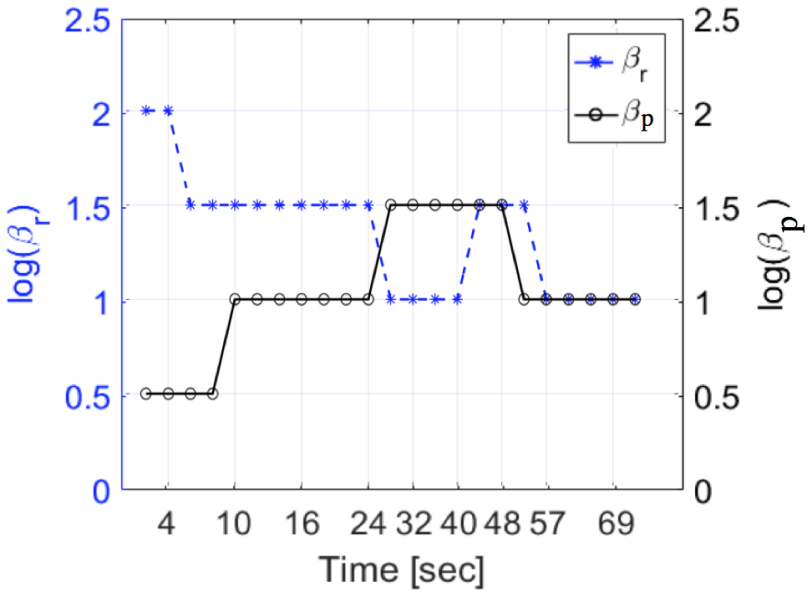

Figure 13.7.: Optimal PIPLE penalty coefficients, β_R and β_P, as a function of time in the sequential CTP study for incident fluence $I_0 = 10^3$.

13.7.1.1 Penalized-Likelihood Regularization

PL was used to reconstruct the simulated images using various regularization parameters swept linearly (in exponent) from $10^{0.5}$ to 10^4 at $10^{0.5}$ increments. The regularization parameter that resulted in the lowest RMSE was chosen as the optimal setting. As shown in Figure 13.5, across all time points $\beta = 10^{1.5}$ resulted in the best RMSE. This suggests an optimization for each time point is not strictly required for PL.

13.7.1.2 Prior-Image Penalized-Likelihood Regularization

Optimal penalty coefficients for PIPLE were computed for all images and exposure levels. The results of a sample 2D parameter sweep for the $I_0 = 10^3$ and $t = 21s$ scenario are shown in Figure 13.6. Specifically, both the RMSE and the reconstructed region-of-interest images are shown as a function of both regularization parameters. The best image quality in terms of RMSE has been achieved by setting $\beta_R = 10$ and $\beta_P = 10^{1.5}$ for this case. Similar patterns emerged for other exposure levels and time points with some variation in optimal parameter values.

Repeating the optimal parameter search for all time points, one can see varying optimality of regularization strength as a function of time point. These optima are shown in Figure 13.7. The optimal value of β_R is decreases for increasing the contrast while β_P is lower for increased contrast between the tumor and surrounding healthy tissue.

Performing an exhaustive search of the 2D and space for each time point may be a time consuming task.

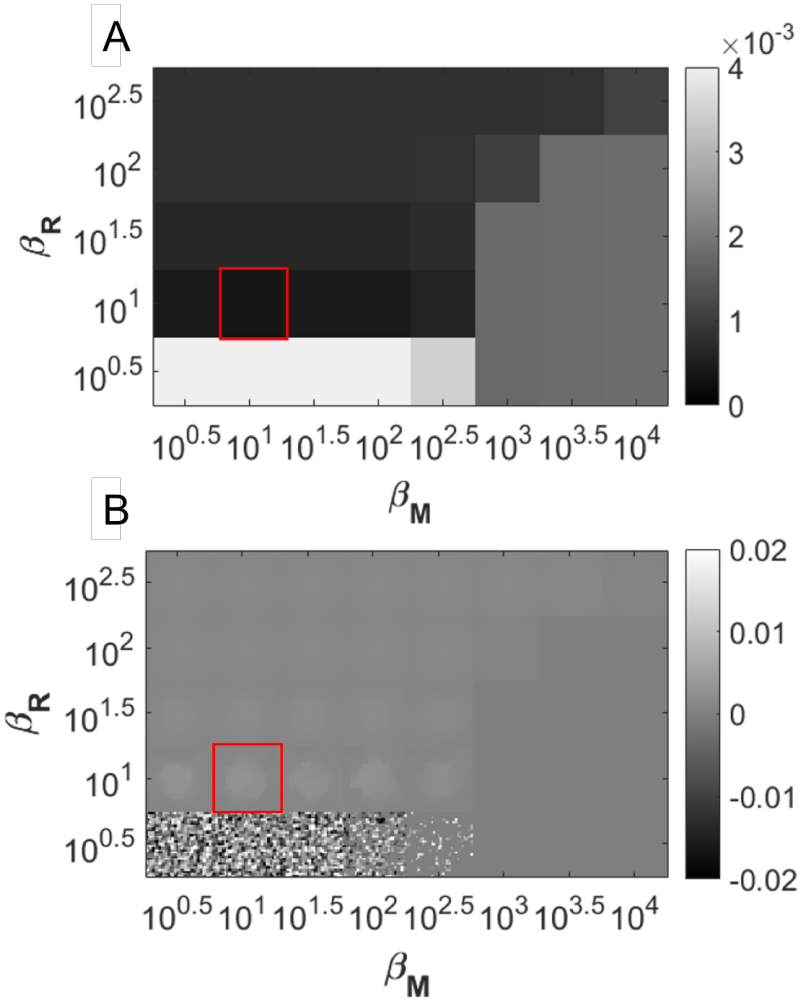

Figure 13.8.: Illustration of RoD regularization investigation for $I_0 = 10^3$ and $t = 21s$. (A) Regional RMSE as a function of both penalty coefficients β_R and β_M evaluated at a $10^{0.5}$ interval and (B) a zoomed ROI showing difference reconstructions μ_Δ associated with each regularization parameter pair. the red box denotes the optimal values.

13.7.1.3 Reconstruction of Difference Regularization

Optimal penalty coefficients for ROD were computed for all images and exposure levels. The results of a sample 2D parameter sweep for the $I_0 = 10^3$ and $t = 21s$ scenario are shown in Figure 13.8. Specifically, both the RMSE and the reconstructed region-of-interest difference images are shown as a function of both regularization parameters. One sees increased noise for lower values and increased blur for large β_R values. Similarly, large values of β_M decreases noise; however, values larger than 10^3 prevented the change from appearing in the reconstructed image. The best image quality in terms of RMSE has been achieved by setting $\beta_R = 10$ and $\beta_M = 10$ for this case. Similar patterns emerged for other exposure levels and time points with some variation in optimal parameter values.

Similar to PIPLE, repeating the optimal parameter search for RoD for all time points, one can see varying optimality of regularization strength as a function of time point. These optima are shown in Figure 13.9. As shown in this figure, the optimal value of β_R

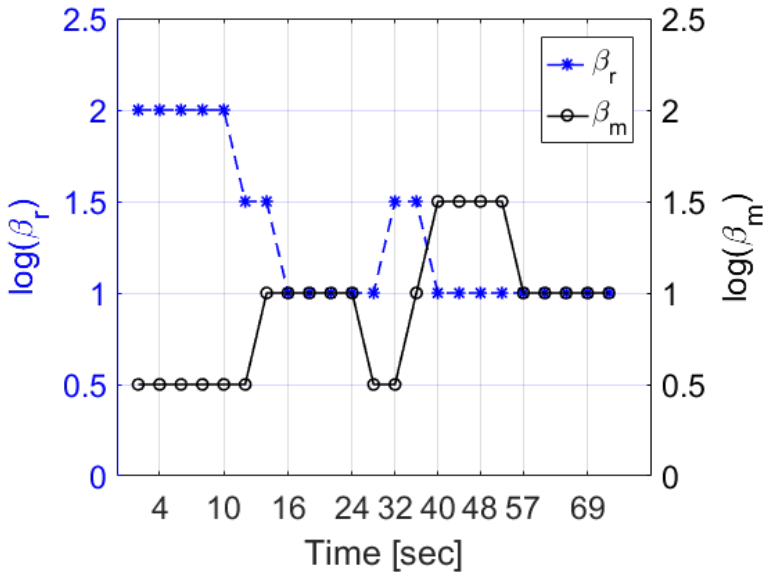

Figure 13.9.: Optimal RoD penalty coefficients, β_R and β_M, as a function of time in the sequential CTP study for incident fluence $I_0 = 10^3$.

is decreases for increasing contrast between tumor and healthy liver tissue. Similarly, we see the opposite relationship for β_M – increasing contrast between the tumor and healthy tissue corresponds to lower optimal values. This suggests that traditional regularization works better for high contrast regions and prior-image-based regularization is more important in low contrast regions.

Performing an exhaustive search of the 2D and 3D space for RoD at each time point may be a time consuming task (similar to PIPLE). However, the results shown in Figure 13.8 are similar to optimizations found in [Dan14], suggesting a directed 1D search could be used.

13.7.2 Incident Fluence Investigation

Figure 13.10(A) and 13.10(B) compare reconstructed ROI images using FDK, PL, PIPLE and RoD reconstruction techniques near the peak of the lesion enhancement curve ($t = 21s$) in the temporal series respectively for homogeneous and Gaussian tumors.

The performance of all methods deteriorated for very low exposures; however, RoD performed consistently qualitatively better than the other methods. These qualitative assessments are echoed in the RMSE values shown in Figure 13.10(C) and 13.10(D). The rank ordering of methods is consistent across all fluence levels with RoD outperforming PL, PIPLE and FDK, and FDK performing worst. The error bars in Figure 13.10(C) and 13.10(D) for different noise realizations shows that the rank order performance has not changed and performance differences are greater than the error bars.

13.7.3 Time-Attenuation Curves

Focusing on the $I_0 = 10^3$ scenario, Figure 13.11(A) and 13.11(B) show individual reconstruction of the homogeneous and Gaussian tumors ROIs across all time points using each reconstruction method, as well as the corresponding ground truth images.

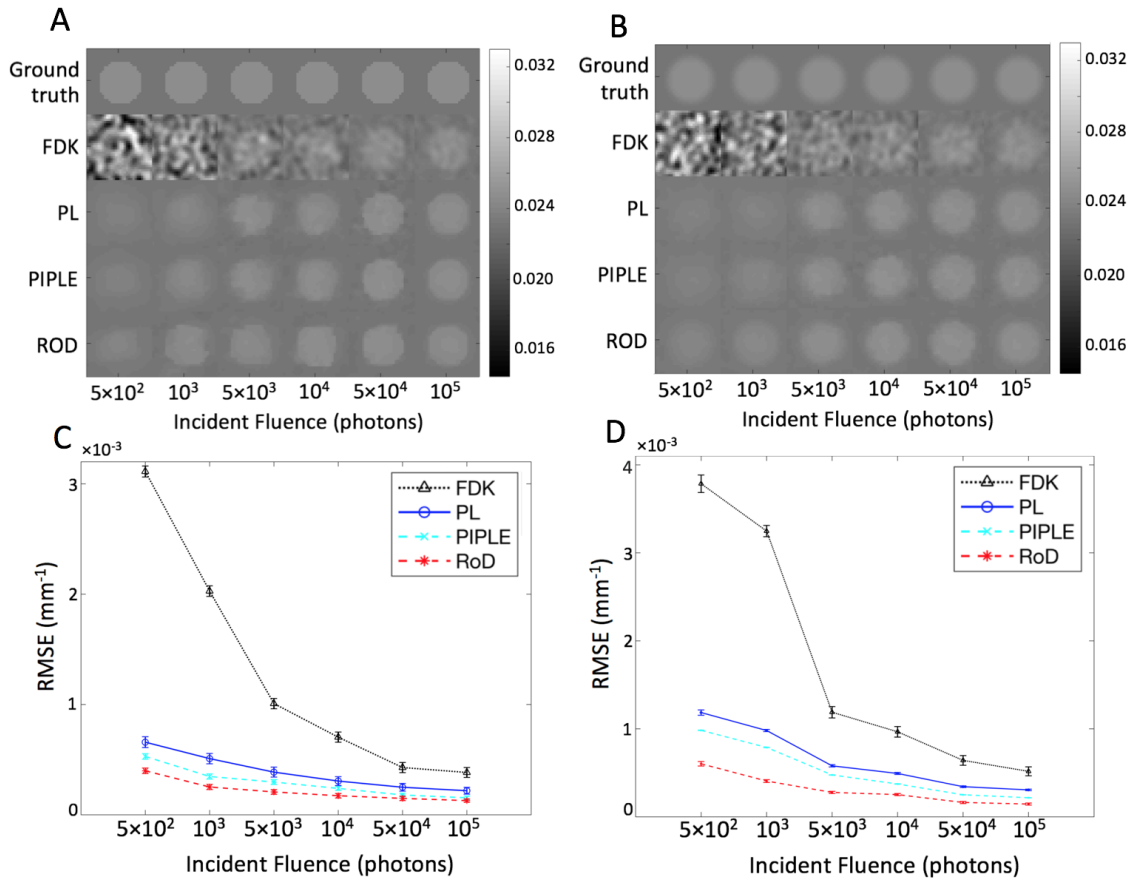

Figure 13.10.: Comparison of different reconstruction methods for incident fluence ranging from $I_0 = 5 \times 10^2$ to $I_0 = 10^5$ at the $t = 21s$ time point. (A) Homogeneous tumor ROI of the reconstructed volume using FDK, PL, PIPLE and RoD for different incident fluence values, and (B) Gaussian tumor ROI of the reconstructed volume using FDK, PL, PIPLE and RoD for different incident fluence values, (C) corresponding RMSE plots of FDK, PL, PIPLE and RoD for homogeneous tumor, and (D) corresponding RMSE plots of FDK, PL, PIPLE and RoD for Gaussian tumor.

Qualitative comparison of reconstructed images shows that RoD reconstruction yielded better image quality across the entire range, even in low contrast regions. In contrast FDK exhibits strong noise across all points. PL and PIPLE perform better but appear to have increased blur as compared with RoD images.

For the same incident fluence of $I_0 = 10^3$, we used all time points in the image sequence to form TACs for each reconstruction approach. Smoothed TACs based on a healthy liver, homogeneous and Gaussian tumors' ROIs are shown in Figure 13.12 for each reconstruction method and ground truth. TACs associated with the reconstructions are shown in Figure Figure 13.12(A), (C) and (E) for the healthy liver tissue, homogeneous tumor and Gaussian tumor tissues, respectively. RMSE plots associated with these estimates are shown in Figure 13.12 (B), (D) and (F) respectively. Stochastic fluctuations observed in the TACs are strongest for FDK and are mitigated by MBIR methods.

The best results are found of RoD which has the lowest RMSE across all time points.

RoD produces TACs closest to the ground truth with a more substantial improvement for the tumor ROI.

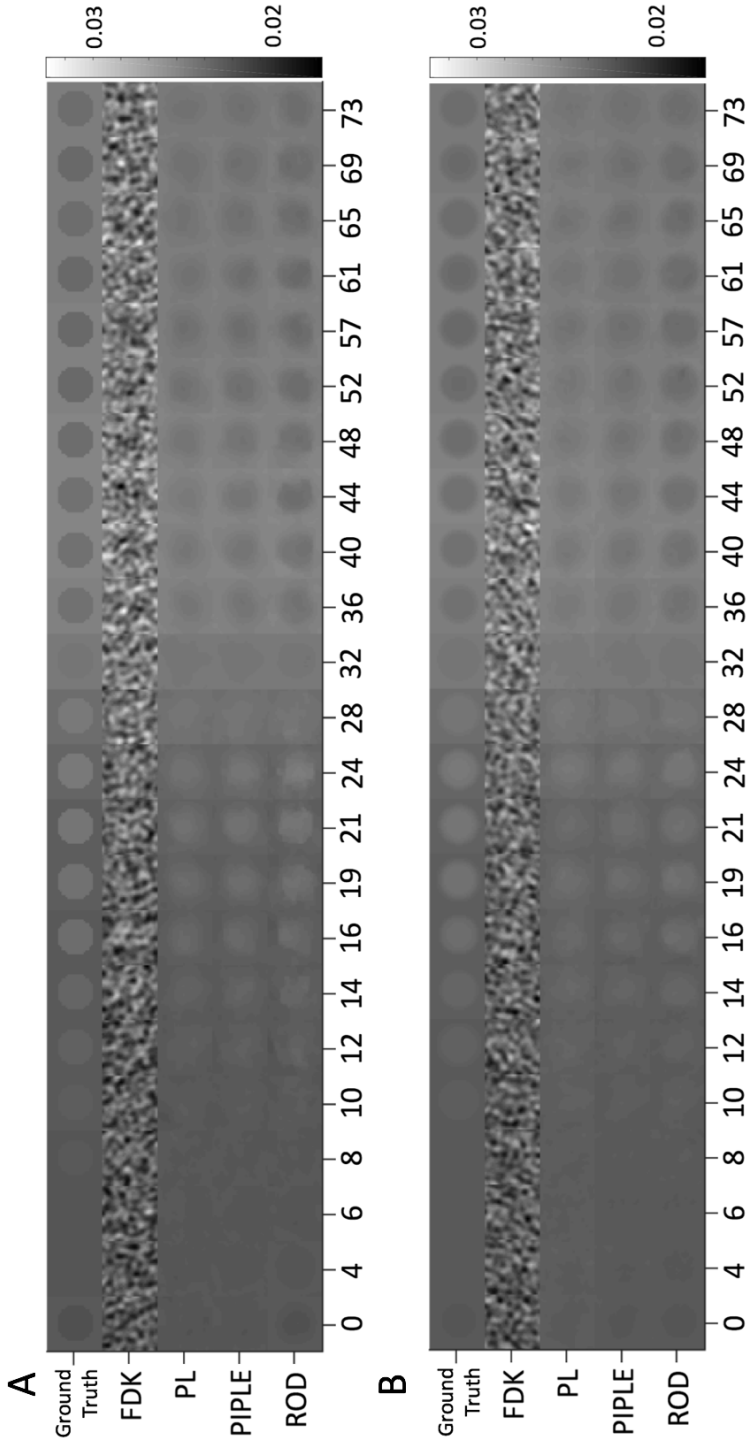

Figure 13.11.: (A) Comparison of homogeneous tumor ROI and (B) Gaussian tumor ROI for FDK, PL, PIPLE and RoD reconstructions for incident fluence $I_0 = 10^3$.

13.7.4 Perfusion Analysis

Figure 13.13 shows the calculated perfusion maps including HAP, HPP, PI and TTP maps for different reconstruction techniques at an incident fluence of $I_0 = 10^3$. Consistent with previous results FDK exhibits increased noise as compared with other approaches. Similarly, the tumor does not appear in the TTP map. RoD outperforms the other methods with better tumor PI contrast and a conspicuous tumor apparent in the TTP map. PL and RoD appear to perform comparably for the HAP and HPP maps. Corresponding RMSE comparisons for these perfusion maps are presented in Figure 13.14 for both the healthy liver and tumor ROIs. PL performs better than FDK, but increased blue in the PI map reduces conspicuity of the tumor. PIPLE performs better than FDK, PL and PIPLE, however the intensity of tumor region in the PI map is still lower than RoD and TTP map also shows a noisy appearance for the liver tissue.

Again, the quantitative results reinforce the qualitative observations with improved performance using RoD. As shown in this figure, the differences are greatest for PI and in the tumor ROI. Similar performance of PL and RoD in the tumor ROI is also noted.

13.8 Conclusion

In this chapter, a novel pipeline for acquisition, reconstruction and processing of sequential CTP imaging data was presented. In particular, an initial high-quality baseline reconstruction of the unenhanced anatomy was used in a prior-image-based reconstruction method called Reconstruction of Difference to improve the image quality of subsequent reconstructions of low-exposure contrast-enhance CT data. The proposed RoD approach outperformed both traditional approaches and another prior image method (PIPLE). The improved performance was demonstrated across a range of exposures for individual time-point reconstructions, for time-attenuation curve estimates, and in the computation of common perfusion metric maps.

The experimental conditions used a high-quality baseline image volume acquired at a fluence of 10^5 photons per detector element (which is a clinically relevant exposure in our experience). Using RoD suggests that this exposure could be dropped to 10^3 photons and retain useful perfusion images instead of repeating the 10^5 photon exposure over 20 times. In the low-exposure RoD case, the dose would be dominated by the initial baseline scan representing a substantial dose reduction (e.g. a 20 times reduction). These preliminary results suggest the underlying methodology is a potentially powerful approach that can be applied in sequential data reconstruction like CT perfusion. Moreover, such methods may enable techniques like liver CTP which have not found widespread clinical use due to radiation dose concerns.

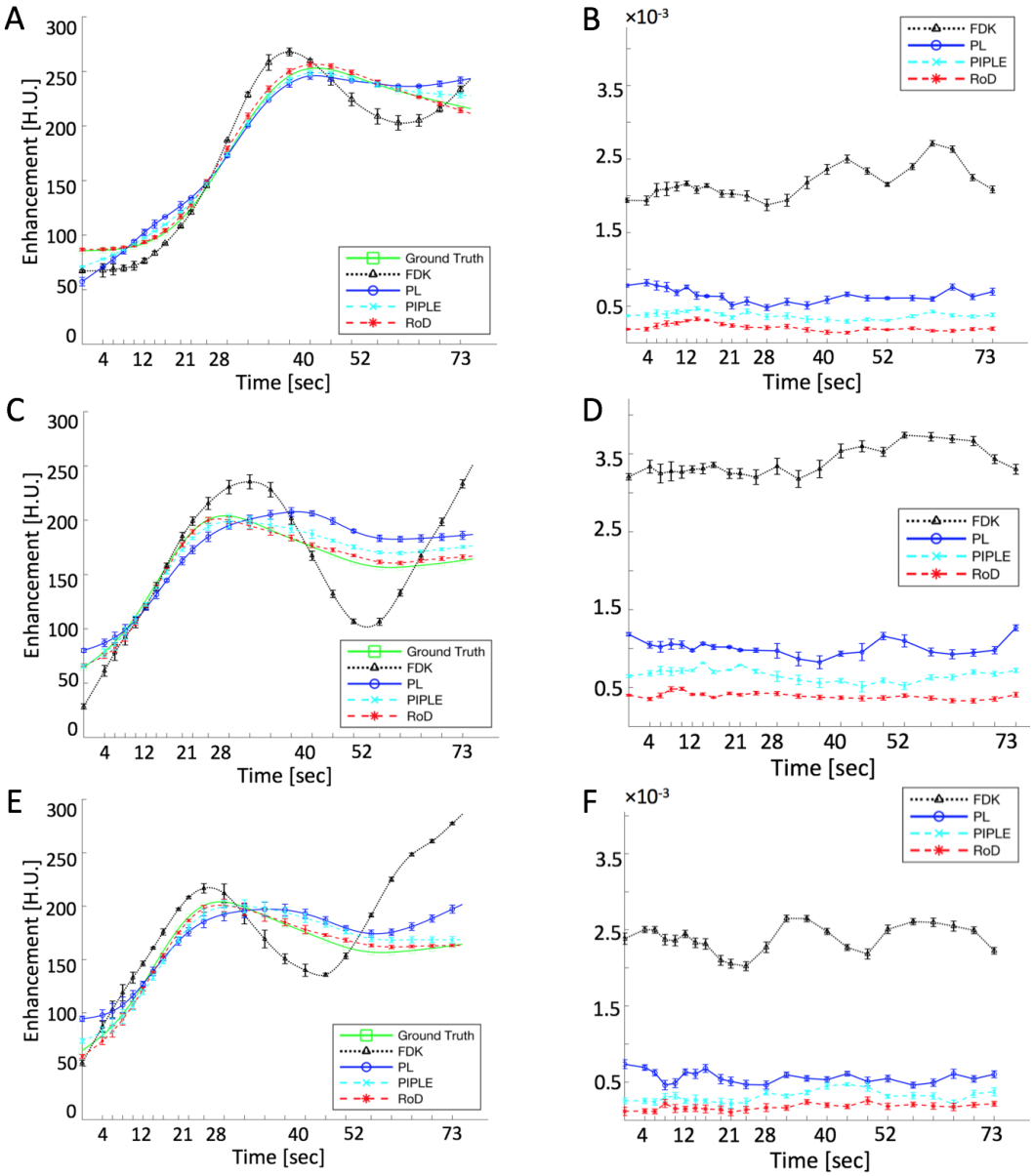

Figure 13.12.: Comparison of TAC estimates homogeneous Gaussian tumor ROIs for FDK, PL, PIPLE and RoD reconstructions for incident fluence (A) TAC plot resulting from averages over healthy liver tissue ROIs, (B) RMSE plot for TAC shown in (A), (C) TAC estimates for the homogeneous tumor ROI, and (D) RMSE plot for TAC shown in (C), (E) TAC estimates for the Gaussian tumor ROI and (F) RMSE plot for TAC shown in (E).

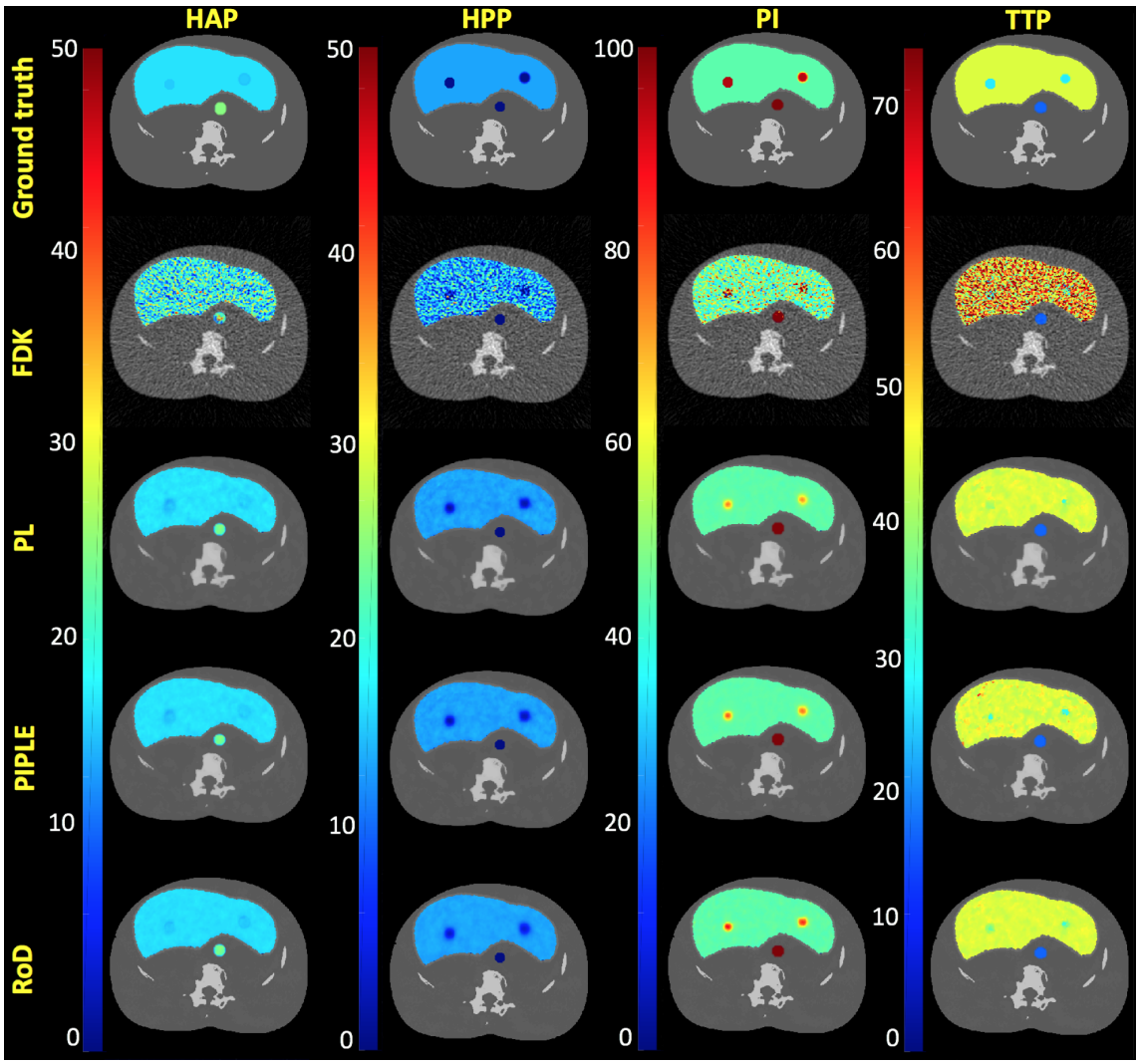

Figure 13.13.: HAP, HPP, PI and TTP maps for FDK, PL, PIPLE and RoD reconstruction methods compared to ground truth for an incident fluence of $I_0 = 10^3$ photons.

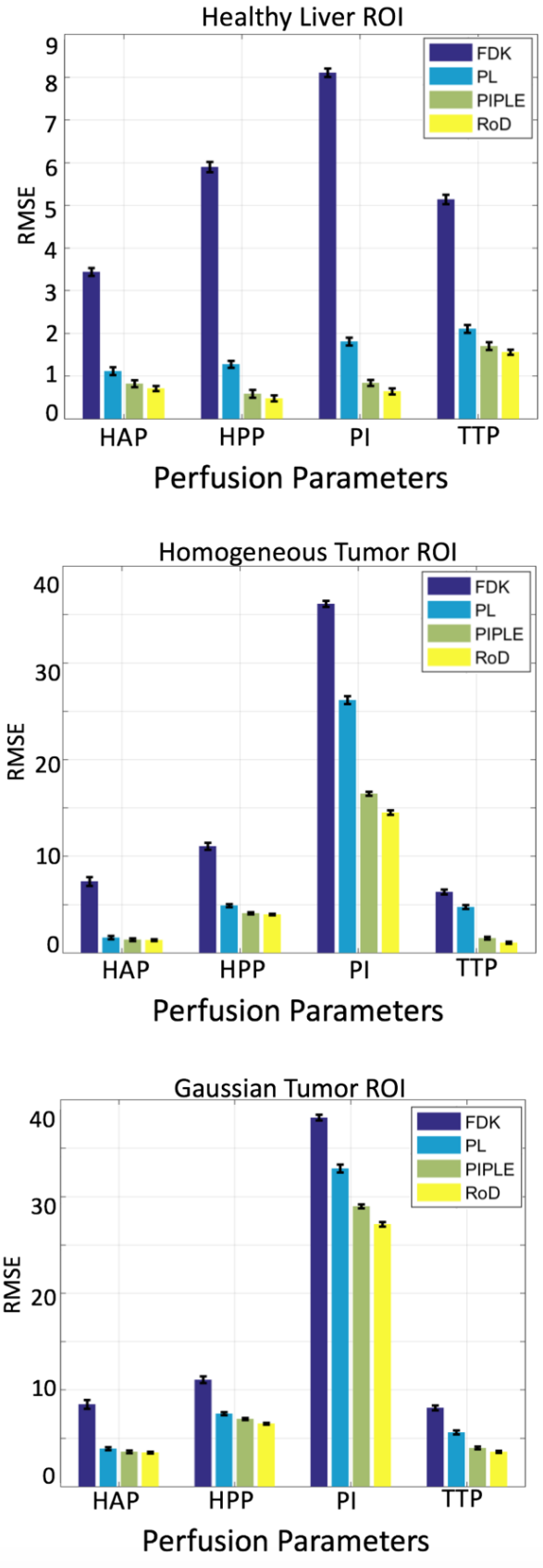

Figure 13.14.: RMSE comparisons of perfusion maps for incident fluence $I_0 = 10^3$ using (A) healthy liver ROIs, (B) the homogeneous tumor ROI and (C) the Gaussian tumor ROI.

14. Outlook

> Do not fear to be eccentric in opinion, for every opinion now accepted was once eccentric.
>
> *Bertrand Russell*

Medical imaging has advanced rapidly in the beginning of the twenty-first century. Diagnostic images captured at the right place and at the right time give physicians, surgeons, and researchers an important tool to help provide better patient care at a lower cost than before. The application of 3D and 4D imaging technologies have the potential to create better images for improved diagnostics in radiology. Recent advances in image acquisitions and formations, resulted in digital images rather than traditional non-digital data. Digital images are more than pictures; they offer sources of data which include several information and solutions that are not easily traceable by human eyes.

Improvements in x-ray based imaging such as computed tomography, in the next decades, will result in reductions of radiation dose in a way where this issue will no longer be of concern. Phase contrast x-ray imaging is also likely to be the next new imaging method to be explored more clinically and in the real applications area.

Until recently, all computed tomography systems reconstructed images using the filtered back projection techniques due to its relatively short running time using older computer systems. However, with recent improvements in computing power and the reduction in costs for the power itself, all the major imaging device vendors now include and offer iterative image reconstruction techniques. New noise reduction, regularization and artifact removal methods have been developed during last decade which enables diagnostic image clarity on low dose scans that was not possible before. This enables CT scanning at much lower doses that a decade ago.

In this thesis, we studied two novel four- and six-dimensional x-ray imaging modalities and investigated several data processing and analysis pipelines along with evaluation techniques to assess the effectiveness of proposed methods.

Particularly, in the first part of this study, we focused on X-ray Tensor Tomography, a novel imaging modality developed for three-dimensional reconstruction of x-ray scattering tensors from dark-field images obtained in a grating interferometry setup. In this part, we addressed one of the main limitations of X-ray Tensor Tomography which is the degradation of the measured two-dimensional dark-field images due to the detector readout noise and insufficient photon statistics affecting, which is consequently, affecting the reconstructed three-dimensional volumes from these data showing noise artifacts. We investigated the best way to incorporate total variation denoising technique into the reconstruction pipeline. Several different schemes for applying noise reduction methods based on two- and three-dimensional TV regularization have been proposed to reduce the noise level before, during or after the reconstruction process and evaluate the effectiveness and quality of images reconstructed and denoised using these schemes.

The quantitative and qualitative evaluation based on datasets from different industrial and clinical samples show improvements in noise reduction for all proposed methods compared to the method without denoising. The best results are achieved by the regularized reconstruction technique for x-ray Tensor Tomography, which aims in interleaving reconstruction and denoising.

In the second part, we studied the low-dose CT perfusion of the liver. Liver CT perfusion is a novel x-ray imaging technique that has demonstrated clinical utility in the detection, staging, and analysis of treatment response in hepatic diseases by enabling the evaluation of several perfusion metrics. We addressed the reduction of radiation exposures associated with hepatic CTP studies which is one the main limitations of CT perfusion tests by developing a novel scheme for acquiring and processing sequential CT perfusion data. We proposed to adapt Reconstruction of Difference method which estimates the difference between unenhanced baseline and subsequent scans. This use of the baseline as a prior image permits significant reductions in noise in reconstructions. Several experiments evaluating the performance of RoD relative to traditional analytic and model based iterative reconstruction methods suggest that proposed method produces better images, better quantification in the TACs, and better perfusion maps for commonly used perfusion metrics. These results suggest the RoD processing can dramatically reduce exposure requirements. In this case, the exposure of all but the unenhanced baseline scan was dropped by two orders of magnitude and accurate perfusion results were maintained.

Through all of this, exciting advances in diagnostic medical imaging, x-ray images processing and computed tomography can be expected. However, so much work is needed to reach to that point by developing faster, clearer and safer imaging technologies that would be available for majority of the populations in the world. On a more positive note, the future of medical imaging and image processing, will bring new capabilities and tools that have even greater medical values to improve humans' lives. We will see radiation dose in x-ray imaging modalities continue to drop and utilization of all imaging services become more efficient, with lower costs and even fewer waste in healthcare resources, to the benefit of patients, physicians and everyone in the healthcare cycle.

List of Figures

List of Tables

Acknowledgments

This dissertation could not have been completed without the great support that I have received from so many people over the years. I wish to offer my most heartfelt thanks to all of them.

First, I would like to especially thank my academic advisor Dr. Tobias Lasser for his guidance and for inspiring me with his deep understanding of several subjects in my projects. I would also like to thank him for his forbearance and understanding during some of the more difficult steps of my PhD studies and his endless supports and motivating helps during last years.

I also would like to thank Prof. Dr. Franz Pfeiffer, my second supervisor from Physics department, for many supports during these years and for hosting me and providing all infrastructures and facilities for my project.

I would like to thank Dr. J. Webster Stayman, my international supervisor from Johns Hopkins University, who was hosting me in his group. You taught me how the scientific community functions, and I could always talk to you during my stay in your lab, no matter if it was about 'the integral of all errors' or anything beyond that.

I would like to acknowledge support via BERTI, European Commission funded project under Grant Agreement Number 605162, which was a great support for my research during last years. I would like to mention plenty of useful trainings and courses arranged by BERTI office, which were motivation keys for me to continue my research and studies in an optimum way.

I would like to express my special appreciation and thanks to Dr. Andrea Glogger, BERTI manager, Dr. Petra Dorfner and Katharina Lang from Graduate School of Bio-engineering for their greatest supports with all official and non-official issues regarding my studies and my research in TUM and for arranging many of interesting events and useful training during the time I was attending as an ESR in BERTI.

I also would like to thank Prof. Dr. Nassir Navab, for lots of opportunities he provided for me throughout my PhD studies to have active interactions with his groups at both TUM and JHU.

I thank Dr. Christina Cozzini my industrial mentor and Dr. Jonathan Sperl and Dr. Dirk Beque from GE-GRC in Munich for their contributions during several meetings and events for my project with plenty of interesting suggestions and corrections for my work.

I want to express my gratitude to the people of both E17 and CAMP chairs, for making me feel like being among friends rather than just colleagues. My special thanks to Yash Sharma, Matthias Wieczorek, Florian Schaff, Christoph Jud, Friedrich Prade and all other Postdocs, Masters and PhD candidates in the group who helped me to develop and finish my project and with whom I had lots of fruitful discussions regarding the problems and issues I was facing in my research.

I am very grateful to Dr. Martin Dierolf, Andreas Fehringer and all the others that keep the IT infrastructure at the chair running and patiently helped me with all networks and servers problem.

I want to thank all the people in AIAI and I-Star labs and Carnegie Center of School of Medicine at Johns Hopkins University and specially Prof. Dr. Jeffrey Siewerdsen, Steven Tilley, Hao Dang, Dr. Hao Zhang, Dr. Grace Gang and Dr. Amir Manbachi who were hosting me for my international research stay during my PhD studies and whom I learned plenty of new and amazing techniques and scientific stuff during that time.

Publications Resulting from this Work

Peer-Reviewed Papers

1. S. Seyyedi, M. Wieczorek, F. Pfeiffer, and T. Lasser. (2018), "Incorporating a Noise Reduction Technique into X-ray Tensor Tomography", *IEEE Transactions on Computational Imaging.*

2. S. Seyyedi, E. Liapi, T. Lasser, R. Ivkov, R. Hatwar, and J. W. Stayman. (2018), "Low-Dose CT Perfusion of the Liver using Reconstruction of Difference", *IEEE Transactions on Radiation & Plasma Medical Science.*

Co-authored

1. Y. Sharma, M. Wieczorek, F. Schaff, S. Seyyedi, F. Prade, F. Pfeiffer, T. Lasser. (2016), "Six dimensional X-ray Tensor Tomography with a compact laboratory setup",*Applied Physics Letters.*, Volume 109 (2016).

Peer-Reviewed Conference Proceedings

1. S. Seyyedi, E. Liapi, T. Lasser, R. Ivkov, R. Hatwar, and J. W. Stayman. (2017), "Evaluation of Low-Dose CT Perfusion for the Liver using Reconstruction of Difference", *Proceedings of International Conference on Fully Three-Dimensional Image Reconstruction in Radiology and Nuclear Medicine*, Xi'an, China, 2017.

2. S. Seyyedi, M. Wieczorek, Y. Sharma, F. Schaff, C. Jud, F. Pfeiffer, and T. Lasser. (2016), "Component-based TV Regularization for X-ray Tensor Tomography", *Proceedings of 13th IEEE International Symposium on Biomedical Imaging (ISBI)*, Prague, Czech Republic, 2016, **(Accepted for oral presentation)** .

3. S. Seyyedi, M. Wieczorek, C. Jud, F. Pfeiffer, and T. Lasser. (2016), "A Regularized X-ray Tensor Tomography Reconstruction Technique", *Proceedings of International Conference on Image Formation in X-Ray Computed Tomography*, Bamberg, Germany, 2016.

Bibliography

[AB14] N. M. AB. *The Nobel Prize in Physics 1901*. 2014. URL: http://www.nobelprize.org/nobel_prizes/physics/laureates/1901/ (visited on 10/15/2017).

[ABP12] M. Analoui, J. D. Bronzino, and D. R. Peterson. *Medical imaging: principles and practices*. CRC Press, 2012.

[AF03] S. Ahn and J. A. Fessler. "Globally convergent image reconstruction for emission tomography using relaxed ordered subsets algorithms." In: *IEEE Transactions on Medical Imaging* 22.5 (2003), pp. 613–626.

[AH73] J. Ambrose and G. Hounsfield. "Computerized transverse axial tomography." In: *The British journal of radiology* 46.542 (Feb. 1973), pp. 148–9. ISSN: 0007-1285.

[AJ94] F. Anton and A. Jahnke. *Synchrotron radiation source*. US Patent 5,341,104. Aug. 1994.

[Alb77] R. D. Albert. *Scanning X-ray source*. US Patent 4,057,745. Nov. 1977.

[AM76] R. E. Alvarez and A. Macovski. "Energy-selective reconstructions in x-ray computerised tomography." In: *Physics in Medicine & Biology* 21.5 (1976), p. 733.

[AMS90] S. F. Ashby, T. A. Manteuffel, and P. E. Saylor. "A taxonomy for conjugate gradient methods." In: *SIAM Journal on Numerical Analysis* 27.6 (1990), pp. 1542–1568.

[And05] M. Ando, K. Yamasaki, F. Toyofuku, H. Sugiyama, C. Ohbayashi, G. Li, L. Pan, X. Jiang, W. Pattanasiriwisawa, D. Shimao, et al. "Attempt at visualizing breast cancer with X-ray dark field imaging." In: *Japanese j. of app. phys.* 44.4L (2005), p. L528.

[Ass15] S. Assili, A. F. Kazerooni, L. Aghaghazvini, H. S. Rad, and J. P. Islamian. "Dynamic contrast magnetic resonance imaging (DCE-MRI) and diffusion weighted MR imaging (DWI) for differentiation between benign and malignant salivary gland tumors." In: *Journal of biomedical physics & engineering* 5.4 (2015), p. 157.

[Ass17] S. Assili, L. Caldeira, P. Lehman, A. Shahbazi, C. Filss, N. J. Shah, and K. Langen. "Evaluation of 18 F-FET-PET and perfusion MRI texture features in brain tumor grades." In: (2017).

[Ass16] S. Assili. "Diffusion and Perfusion Magnetic Resonance Imaging:Fundamentals and Advances." In: *ArXiv e-prints* (Nov. 2016). arXiv: 1611.06826 [physics.med-ph].

[Awa04] K. Awai, K. Murao, A. Ozawa, M. Komi, H. Hayakawa, S. Hori, and Y. Nishimura. "Pulmonary nodules at chest CT: effect of computer-aided diagnosis on radiologists' detection performance." In: *Radiology* 230.2 (2004), pp. 347–352.

[Bær01] J. A. Bærentzen. *On the implementation of fast marching methods for 3D lattices*. Tech. rep. 2001.

[Bai05] D. L. Bailey, D. W. Townsend, P. E. Valk, and M. N. Maisey. *Positron emission tomography*. Springer, 2005.

[Bay14a] F. L. Bayer, S. Hu, A. Maier, T. Weber, G. Anton, T. Michel, and C. P. Riess. "Reconstruction of scalar and vectorial components in X-ray dark-field tomography." In: *Proceedings of the National Academy of Sciences* 111.35 (2014), pp. 12699–12704.

[Bay14b] F. L. Bayer, S. Hu, A. Maier, T. Weber, G. Anton, T. Michel, and C. P. Riess. "Reconstruction of scalar and vectorial components in X-ray dark-field tomography." In: *Proceedings of the National Academy of Sciences* 111.35 (2014), pp. 12699–12704.

[BCS12] A. Bravin, P. Coan, and P. Suortti. "X-ray phase-contrast imaging: from pre-clinical applications towards clinics." In: *Physics in medicine and biology* 58.1 (2012), R1.

[Bec10] M. Bech, O. Bunk, T. Donath, R. Feidenhans, C. David, and F. Pfeiffer. "Quantitative x-ray dark-field computed tomography." In: *Phys. in med. and bio.* 55.18 (2010), p. 5529.

[Bec09] M. Bech. "X-ray imaging with a grating interferometer." PhD thesis. Museum Tusculanum, 2009.

[Beh15] R. Behling. *Modern Diagnostic X-Ray Sources: Technology, Manufacturing, Reliability*. CRC Press, 2015.

[BF11] F. E. Boas and D. Fleischmann. "Evaluation of two iterative techniques for reducing metal artifacts in computed tomography." In: *Radiology* 259.3 (2011), pp. 894–902.

[BF12] F. E. Boas and D. Fleischmann. "CT artifacts: causes and reduction techniques." In: *Imaging Med* 4.2 (2012), pp. 229–240.

[BH65] U. Bonse and M. Hart. "An X-ray interferometer." In: *App. Phys. Lett.* 6.8 (1965), pp. 155–156.

[Bis07] S. Bisdas, M. Baghi, J. Wagenblast, R. Knecht, C. H. Thng, T. S. Koh, and T. J. Vogl. "Differentiation of benign and malignant parotid tumors using deconvolution-based perfusion CT imaging: Feasibility of the method and initial results." In: *European Journal of Radiology* 64.2 (2007), pp. 258–265. ISSN: 0720048X. DOI: 10.1016/j.ejrad.2007.02.032.

[BK04] J. F. Barrett and N. Keat. "Artifacts in CT: recognition and avoidance." In: *Radiographics* 24.6 (2004), pp. 1679–1691.

[Bla05] H. Blattmann, J.-O. Gebbers, E. Bräuer-Krisch, A. Bravin, G. Le Duc, W. Burkard, M. Di Michiel, V. Djonov, D. Slatkin, J. Stepanek, et al. "Applications of synchrotron X-rays to radiotherapy." In: *Nuclear Instruments and Methods in Physics Research Section A: Accelerators, Spectrometers, Detectors and Associated Equipment* 548.1 (2005), pp. 17–22.

[Boy11] S. Boyd, N. Parikh, B. P. E Chu, and J. Eckstein. "Distributed Optimization and Statistical Learning via the Alternating Direction Method of Multipliers." In: *Found. and Tre. in Mach. Lea.* 3.1 (2011), pp. 1–122. ISSN: 1935-8237. DOI: 10.1561/2200000016.

[Bui11] M. Buijs, J. A. Vossen, J.-F. H. Geschwind, N. Salibi, L. Pan, V. P. Ventura, E. Liapi, K. H. Lee, and I. R. Kamel. "Quantitative proton MR spectroscopy as a biomarker of tumor necrosis in the rabbit VX2 liver tumor." In: *Journal of Vascular and Interventional Radiology* 22.8 (2011), pp. 1175–1180.

[Buz08] T. M. Buzug. *Computed tomography: from photon statistics to modern cone-beam CT*. Springer Science & Business Media, 2008.

[Cas14] M. Castillo. "History and evolution of brain tumor imaging: insights through radiology." In: *Radiology* 273.2S (2014), S111–S125.

[CB13] V. Cnudde and M. N. Boone. "High-resolution X-ray computed tomography in geosciences: A review of the current technology and applications." In: *Earth-Science Reviews* 123 (2013), pp. 1–17.

[Cha11] M. Chabior, T. Donath, C. David, M. Schuster, C. Schroer, and F. Pfeiffer. "Signal-to-noise ratio in x ray dark-field imaging using a grating interferometer." In: *Journal of Applied Physics* 110.5, 053105 (2011).

[Che04] J.-H. Chen, Y. Lin, Y. Huang, T. Chen, W. Lin, and K. Han. "Induction of VX2 carcinoma in rabbit liver: comparison of two inoculation methods." In: *Laboratory animals* 38.1 (2004), pp. 79–84.

[Che09] M.-L. Chen, Q.-Y. Zeng, J.-W. Huo, X.-M. Yin, B.-P. Li, and J.-X. Liu. "Assessment of the hepatic microvascular changes in liver cirrhosis by perfusion computed tomography." In: *World J Gastroenterol* 15.28 (2009), pp. 3532–3537.

[CL97] A. Chambolle and P.-L. Lions. "Image recovery via total variation minimization and related problems." In: *Numerische Mathematik* 76.2 (1997), pp. 167–188.

[Cla98] J. F. Clauser. *Ultrahigh resolution interferometric x-ray imaging*. US Patent 5,812,629. Sept. 1998.

[Con12] W. Cong, F. Pfeiffer, M. Bech, and G. Wang. "X-ray dark-field imaging modeling." In: *JOSA A* 29.6 (2012), pp. 908–912.

[Coo16] W. D. Coolidge. *Vacuum-tube.* US Patent 1,203,495. Oct. 1916.

[Cor63] A. M. Cormack. "Representation of a Function by Its Line Integrals, with Some Radiological Applications." In: *Journal of Applied Physics* 34.9 (Sept. 1963), pp. 2722–2727. ISSN: 0021-8979. DOI: 10.1063/1.1729798.

[CTL08a] G.-H. Chen, J. Tang, and S. Leng. "Prior image constrained compressed sensing (PICCS): a method to accurately reconstruct dynamic CT images from highly undersampled projection data sets." In: *Medical physics* 35.2 (2008), pp. 660–663. ISSN: 00942405. DOI: 10.1118/1.2836423.

[CTL08b] G.-H. Chen, J. Tang, and S. Leng. "Prior image constrained compressed sensing (PICCS): a method to accurately reconstruct dynamic CT images from highly undersampled projection data sets." In: *Medical physics* 35.2 (2008), pp. 660–663.

[Cue02] C. A. Cuenod, I. Leconte, N. Siauve, F. Frouin, C. Dromain, O. Clément, and G. Frija. "Deconvolution technique for measuring tissue perfusion by dynamic CT: application to normal and metastatic liver." In: *Academic radiology* 9.1 (2002), S205–S211.

[Dam13] W. C. Dampier. *A shorter history of science*. Cambridge University Press, 2013.

[Dam71] R. Damadian. "Tumor detection by nuclear magnetic resonance." In: *Science* 171.3976 (1971), pp. 1151–1153.

[DAn10] M. D'Antò, M. Cesarelli, P. Bifulco, M. Romano, V. Cerciello, F. Fiore, and A. Vecchione. "Study of different Time Attenuation Curve processing in liver CT perfusion." In: *Information Technology and Applications in Biomedicine (ITAB), 2010 10th IEEE International Conference on*. IEEE. 2010, pp. 1–4.

[Dan14] H. Dang, A. Wang, M. S. Sussman, J. Siewerdsen, and J. W. Stayman. "dPIRPLE: a joint estimation framework for deformable registration and penalized-likelihood CT image reconstruction using prior images." In: *Physics in medicine and biology* 59.17 (2014), p. 4799.

[De 00] B. De Man, J. Nuyts, P. Dupont, G. Marchal, and P. Suetens. "Reduction of metal streak artifacts in x-ray computed tomography using a transmission maximum a posteriori algorithm." In: *IEEE transactions on nuclear science* 47.3 (2000), pp. 977–981.

[De 99] B. De Man, J. Nuyts, P. Dupont, G. Marchal, and P. Suetens. "Metal streak artifacts in X-ray computed tomography: a simulation study." In: *IEEE Transactions on Nuclear Science* 46.3 (1999), pp. 691–696.

[De 93] A. R. De Pierro. "On the relation between the ISRA and the EM algorithm for positron emission tomography." In: *IEEE transactions on Medical Imaging* 12.2 (1993), pp. 328–333.

[Don06] D. L. Donoho. "Compressed sensing." In: *IEEE Transactions on Information Theory* 52.4 (2006), pp. 1289–1306. ISSN: 00189448. DOI: Doi10.1109/Tit.2006.871582.

[DS96] D. C. Dobson and F. Santosa. "Recovery of blocky images from noisy and blurred data." In: *SIAM Journal on Applied Mathematics* 56.4 (1996), pp. 1181–1198.

[DWH03] S. Diederich, D. Wormanns, and W. Heindel. "Lung cancer screening with low-dose CT." In: *European journal of radiology* 45.1 (2003), pp. 2–7.

[Eas02] J. D. Eastwood, M. H. Lev, T. Azhari, T.-Y. Lee, D. P. Barboriak, D. M. Delong, C. Fitzek, M. Herzau, M. Wintermark, R. Meuli, et al. "CT perfusion scanning with deconvolution analysis: pilot study in patients with acute middle cerebral artery stroke." In: *Radiology* 222.1 (2002), pp. 227–236.

[EF99a] H. Erdogan and J. A. Fessler. "Monotonic algorithms for transmission tomography." In: *IEEE Transactions on Medical Imaging* 18.9 (1999), pp. 801–814. ISSN: 02780062. DOI: 10.1109/42.802758.

[EF99b] H. Erdogan and J. A. Fessler. "Monotonic algorithms for transmission tomography." In: *IEEE transactions on medical imaging* 18.9 (1999), pp. 801–814.

[EF99c] H. Erdogan and J. A. Fessler. "Ordered subsets algorithms for transmission tomography." In: *Physics in Medicine & Biology* 44.11 (1999), p. 2835.

[EK12] Y. C. Eldar and G. Kutyniok. *Compressed sensing: theory and applications*. Cambridge University Press, 2012.

[Erd99] H. Erdoğan. *Statistical image reconstruction algorithms using paraboloidal surrogates for PET transmission scans*. University of Michigan, 1999.

[Ert12] M. Ertas, A. Akan, K. Cengiz, M. Kamasak, S. Seyyedi, and I. Yildirim. "3-D tomosynthesis image reconstruction using total variation." In: *BioMedical Computing (BioMedCom), 2012 ASE/IEEE International Conference on*. IEEE. 2012, pp. 1–5.

[Eva68] R. D. Evans. "X-ray and γ-ray interactions." In: *Fundamentals (Second Edition)*. Elsevier, 1968, pp. 93–155.

[FDK84] L. Feldkamp, L. Davis, and J. Kress. "Practical cone-beam algorithm." In: *JOSA A* 1.6 (1984), pp. 612–619.

[Fes] J. A. Fessler. "Image reconstruction: Algorithms and analysis." In: ().

[Fes00] J. A. Fessler. "Statistical image reconstruction methods for transmission tomography." In: *Handbook of medical imaging* 2 (2000), pp. 1–70.

[FGZ80] E. Förster, K. Goetz, and P. Zaumseil. "Double crystal diffractometry for the characterization of targets for laser fusion experiments." In: *Kristall und Technik* 15.8 (1980), pp. 937–945.

[FP63] R. Fletcher and M. J. Powell. "A rapidly convergent descent method for minimization." In: *The computer journal* 6.2 (1963), pp. 163–168.

[FR64] R. Fletcher and C. M. Reeves. "Function minimization by conjugate gradients." In: *The computer journal* 7.2 (1964), pp. 149–154.

[FR96] J. A. Fessler and W. L. Rogers. "Spatial resolution properties of penalized-likelihood image reconstruction: space-invariant tomographs." In: *IEEE Transactions on Image processing* 5.9 (1996), pp. 1346–1358.

[Fun11] Y. Funama, K. Taguchi, D. Utsunomiya, S. Oda, Y. Yanaga, Y. Yamashita, and K. Awai. "Combination of a low tube voltage technique with the hybrid iterative reconstruction (iDose) algorithm at coronary CT angiography." In: *Journal of computer assisted tomography* 35.4 (2011), p. 480.

[Gam02] S. S. Gambhir. "Molecular imaging of cancer with positron emission tomography." In: *Nature Reviews Cancer* 2.9 (2002), p. 683.

[GBH70] R. Gordon, R. Bender, and G. T. Herman. "Algebraic reconstruction techniques (ART) for three-dimensional electron microscopy and X-ray photography." In: *Journal of theoretical Biology* 29.3 (1970), pp. 471–481.

[Gen02] K. Gentile. "The care and feeding of digital, pulse-shaping filters." In: *RF DESIGN* 25.4 (2002), pp. 50–58.

[Gey15] L. L. Geyer, U. J. Schoepf, F. G. Meinel, J. W. Nance Jr, G. Bastarrika, J. A. Leipsic, N. S. Paul, M. Rengo, A. Laghi, and C. N. De Cecco. "State of the art: iterative CT reconstruction techniques." In: *Radiology* 276.2 (2015), pp. 339–357.

[Gil01] J. Gillard, N. Antoun, N. Burnet, and J. Pickard. "Reproducibility of quantitative CT perfusion imaging." In: *The British journal of radiology* 74.882 (2001), pp. 552–555.

[GKR85] R. Glowinski, H. Keller, and L. Reinhart. "Continuation-conjugate gradient methods for the least squares solution of nonlinear boundary value problems." In: *SIAM journal on scientific and statistical computing* 6.4 (1985), pp. 793–832.

[Gor74] R. Gordon. "A tutorial on ART (algebraic reconstruction techniques)." In: *IEEE Transactions on Nuclear Science* 21.3 (1974), pp. 78–93.

[Gra15] S. Grandl, K. Scherer, A. Sztrókay-Gaul, L. Birnbacher, K. Willer, M. Chabior, J. Herzen, D. Mayr, S. D. Auweter, F. Pfeiffer, F. Bamberg, and K. Hellerhoff. "Improved visualization of breast cancer features in multifocal carcinoma using phase-contrast and dark-field mammography: an ex vivo study." In: *European Radiology* 25.12 (2015), pp. 3659–3668. ISSN: 1432-1084. DOI: 10.1007/s00330-015-3773-5.

[Had02] J. Hadamard. "Sur les problèmes aux dérivés partielles et leur signification physique." In: *Princeton University Bulletin* 13 (1902), pp. 49–52.

[Han15] C. Hannesschläger, V. Revol, B. Plank, D. Salaberger, and J. Kastner. "Fibre structure characterisation of injection moulded short fibre-reinforced polymers by X-ray scatter dark field tomography." In: *Case Studies in Nondestructive Testing and Evaluation* 3 (2015), pp. 34–41. ISSN: 2214-6571. DOI: http://dx.doi.org/10.1016/j.csndt.2015.04.001.

[Har09] A. K. Hara, R. G. Paden, A. C. Silva, J. L. Kujak, H. J. Lawder, and W. Pavlicek. "Iterative reconstruction technique for reducing body radiation dose at CT: feasibility study." In: *American Journal of Roentgenology* 193.3 (2009), pp. 764–771.

[Has06] K. Hashimoto, T. Murakami, K. Dono, M. Hori, T. Kim, M. Kudo, S. Marubashi, A. Miyamoto, Y. Takeda, H. Nagano, et al. "Assessment of the severity of liver disease and fibrotic change: the usefulness of hepatic CT perfusion imaging." In: *Oncology reports* 16.4 (2006), pp. 677–684.

[Her00] W. Herschel. "Experiments on the refrangibility of the invisible rays of the sun. by william herschel, ll. dfrs." In: *Philosophical Transactions of the Royal Society of London* (1800), pp. 284–292.

[Her09] G. T. Herman. *Fundamentals of computerized tomography: image reconstruction from projections*. Springer Science & Business Media, 2009.

[Her87] H. Hertz. "Ueber sehr schnelle electrische Schwingungen." In: *Annalen der Physik* 267.7 (1887), pp. 421–448.

[HF07] M. S. Hassouna and A. A. Farag. "Multistencils fast marching methods: A highly accurate solution to the eikonal equation on cartesian domains." In: *IEEE transactions on pattern analysis and machine intelligence* 29.9 (2007), pp. 1563–1574.

[HN82] T. Hayashi and S. Nomura. *X-ray tubes*. US Patent 4,344,011. Aug. 1982.

[Hoa14] J. K. Hoang, W.-k. Sung, M. Bahl, and C. D. Phillips. "How to perform parathyroid 4D CT: tips and traps for technique and interpretation." In: *Radiology* 270.1 (2014), pp. 15–24.

[Hoh06] M. Hoheisel. "Review of medical imaging with emphasis on X-ray detectors." In: *Nuclear Instruments and Methods in Physics Research Section A: Accelerators, Spectrometers, Detectors and Associated Equipment* 563.1 (2006), pp. 215–224.

[Hol10] T. A. Holly, B. G. Abbott, M. Al-Mallah, D. A. Calnon, M. C. Cohen, F. P. DiFilippo, E. P. Ficaro, M. R. Freeman, R. C. Hendel, D. Jain, et al. "Single photon-emission computed tomography." In: *Journal of nuclear cardiology* 17.5 (2010), pp. 941–973.

[Hot33] H. Hotelling. "Analysis of a complex of statistical variables into principal components." In: *Journal of educational psychology* 24.6 (1933), p. 417.

[HRH03] W. R. Hendee, E. R. Ritenour, and K. R. Hoffmann. "Medical imaging physics." In: *Medical Physics* 30.4 (2003), pp. 730–730.

[HS52] M. R. Hestenes and E. Stiefel. *Methods of conjugate gradients for solving linear systems*. Vol. 49. 1. NBS Washington, DC, 1952.

[Hsi09] J. Hsieh et al. "Computed tomography: principles, design, artifacts, and recent advances." In: SPIE Bellingham, WA. 2009.

[HT90] B. L. Holman and S. S. Tumeh. "Single-photon emission computed tomography (SPECT): applications and potential." In: *Jama* 263.4 (1990), pp. 561–564.

[Hu99] H. Hu. "Multi-slice helical CT: Scan and reconstruction." In: *Medical physics* 26.1 (1999), pp. 5–18.

[Hub64] P. J. Huber et al. "Robust estimation of a location parameter." In: *The Annals of Mathematical Statistics* 35.1 (1964), pp. 73–101.

[Hub82] J. Hubbell. "Photon mass attenuation and energy-absorption coefficients." In: *The International Journal of Applied Radiation and Isotopes* 33.11 (1982), pp. 1269–1290.

[IB95] V. Ingal and E. Beliaevskaya. "X-ray plane-wave topography observation of the phase contrast from a non-crystalline object." In: *Jour. of Phys. & App. Phys.* 28.11 (1995), p. 2314.

[Ipp12] D. Ippolito, C. Capraro, A. Casiraghi, C. Cestari, and S. Sironi. "Quantitative assessment of tumour associated neovascularisation in patients with liver cirrhosis and hepatocellular carcinoma: role of dynamic-CT perfusion imaging." In: *European radiology* 22.4 (2012), pp. 803–811.

[Jai08] R. Jain, S. Ellika, L. Scarpace, L. Schultz, J. Rock, J. Gutierrez, S. Patel, J. Ewing, and T. Mikkelsen. "Quantitative estimation of permeability surface-area product in astroglial brain tumors using perfusion CT and correlation with histopathologic grade." In: *American Journal of Neuroradiology* 29.4 (2008), pp. 694–700.

[Jen10] T. H. Jensen, M. Bech, O. Bunk, T. Donath, C. David, R. Feidenhans'l, and F. Pfeiffer. "Directional x-ray dark-field imaging." In: *Physics in Medicine and Biology* 55.12 (2010), p. 3317.

[JGM13] A. F. Juliano, D. T. Ginat, and G. Moonis. "Imaging review of the temporal bone: part I. Anatomy and inflammatory and neoplastic processes." In: *Radiology* 269.1 (2013), pp. 17–33.

[Kac37] S. Kaczmarz. "Angenaherte auflosung von systemen linearer gleichungen." In: *Bull. Int. Acad. Sci. Pologne, A* 35 (1937), pp. 355–357.

[Kal06] W. A. Kalender. "X-ray computed tomography." In: *Phys. Med. Biol* 51 (2006), pp. 29–43. DOI: 10.1088/0031-9155/51/13/R03.

[Kan05] J. A. Kanis, F. Borgstrom, C. De Laet, H. Johansson, O. Johnell, B. Jonsson, A. Oden, N. Zethraeus, B. Pfleger, and N. Khaltaev. "Assessment of fracture risk." In: *Osteoporosis international* 16.6 (2005), pp. 581–589.

[Kev98] B. Kevles. *Naked to the bone: Medical imaging in the twentieth century*. Basic Books, 1998.

[KHE87] W. A. Kalender, R. Hebel, and J. Ebersberger. "Reduction of CT artifacts caused by metallic implants." In: *Radiology* 164.2 (1987), pp. 576–577.

[KKW14] S. H. Kim, A. Kamaya, and J. K. Willmann. "CT Perfusion of the Liver: Principles and Applications in Oncology." In: *Radiology* 272.2 (2014), pp. 322–44. ISSN: 1527-1315. DOI: 10.1148/radiol.14130091.

[Kno83] G. Knoll. "Single-photon emission computed tomography." In: *Proceedings of the IEEE* 71.3 (1983), pp. 320–329.

[Koe98] M. Koenig, E. Klotz, B. Luka, D. J. Venderink, J. F. Spittler, and L. Heuser. "Perfusion CT of the brain: diagnostic approach for early detection of ischemic stroke." In: *Radiology* 209.1 (1998), pp. 85–93.

[Kon09] A. Konstas, G. Goldmakher, T.-Y. Lee, and M. Lev. "Theoretic basis and technical implementations of CT perfusion in acute ischemic stroke, part 1: theoretic basis." In: *American Journal of Neuroradiology* 30.4 (2009), pp. 662–668.

[KS88] A. C. Kak and M. Slaney. *Principles of computerized tomographic imaging*. IEEE press, 1988.

[L84a] K. Lange, R. Carson, et al. "EM reconstruction algorithms for emission and transmission tomography." In: *J Comput Assist Tomogr* 8.2 (1984), pp. 306–16.

[L84b] D. G. Luenberger, Y. Ye, et al. *Linear and nonlinear programming*. Vol. 2. Springer, 1984.

[La 97] J. L. de La Grange. *Théorie des fonctions analytiques*. 1797.

[Le 92] D. Le Bihan, R. Turner, P. Douek, and N. Patronas. "Diffusion MR imaging: clinical applications." In: *AJR. American journal of roentgenology* 159.3 (1992), pp. 591–599.

[Lee17] H. Lee, H. Kim, H. Han, M. Lee, S. Lee, H. Yoo, J. H. Chang, and H. Kim. "Microbubbles used for contrast enhanced ultrasound and theragnosis: a review of principles to applications." In: *Biomedical Engineering Letters* 7.2 (2017), pp. 59–69.

[Lee02] T.-Y. Lee. "Functional CT: physiological models." In: *Trends in biotechnology* 20.8 (2002), S3–S10.

[Lew97] R. Lewis. "Medical applications of synchrotron radiation x-rays." In: *Physics in medicine and biology* 42.7 (1997), p. 1213.

[LFB10] Y. Long, J. A. Fessler, and J. M. Balter. "3D forward and back-projection for X-ray CT using separable footprints." In: *IEEE transactions on medical imaging* 29.11 (2010), pp. 1839–1850.

[Li14] H.-o. Li, C. Sun, Z.-d. Xu, F. Miao, D.-j. Zhang, J.-h. Chen, X. Li, X.-m. Wang, C. Liu, and B. Zhao. "Low-dose whole organ CT perfusion of the pancreas: preliminary study." In: *Abdominal imaging* 39.1 (2014), pp. 40–47.

[LMS15] E. Liapi, M. Mahesh, and D. V. Sahani. "Is CT perfusion ready for liver cancer treatment evaluation?" In: *Journal of the American College of Radiology* 12.1 (2015), pp. 111–113. ISSN: 1558349X. DOI: 10.1016/j.jacr.2014.10.007.

[Low58] F. Low. "Bremsstrahlung of very low-energy quanta in elementary particle collisions." In: *Physical Review* 110.4 (1958), p. 974.

[Mal13] A. Malecki, G. Potdevin, T. Biernath, E. Eggl, E. G. Garcia, T. Baum, P. B. Noël, J. S. Bauer, and F. Pfeiffer. "Coherent superposition in grating-based directional dark-field imaging." In: *PloS one* 8.4 (2013), e61268.

[Mal14] A. Malecki, G. Potdevin, T. Biernath, E. Eggl, K. Willer, T. Lasser, J. Maisenbacher, J. Gibmeier, A. Wanner, and F. Pfeiffer. "X-ray tensor tomography." In: *EPL* 105.3 (2014), p. 38002.

[Mar16] H. E. Martz, C. M. Logan, D. J. Schneberk, and P. J. Shull. *X-ray imaging: Fundamentals, Industrial Techniques and Applications*. CRC Press, 2016.

[Max65] J. C. Maxwell. "A dynamical theory of the electromagnetic field." In: *Philosophical transactions of the Royal Society of London* 155 (1865), pp. 459–512.

[May00] T. E. Mayer, G. F. Hamann, J. Baranczyk, B. Rosengarten, E. Klotz, M. Wiesmann, U. Missler, G. Schulte-Altedorneburg, and H. J. Brueckmann. "Dynamic CT perfusion imaging of acute stroke." In: *American journal of neuroradiology* 21.8 (2000), pp. 1441–1449.

[MEK07] K. Miles, J. D. Eastwood, and M. Konig. *Multidetector computed tomography in cerebrovascular disease: CT perfusion imaging*. CRC Press, 2007.

[MG03a] K. A. Miles and M. R. Griffiths. "Perfusion CT: A worthwhile enhancement?" In: *British Journal of Radiology* 76.904 (2003), pp. 220–231. ISSN: 00071285. DOI: 10.1259/bjr/13564625.

[MG03b] K. A. Miles and M. Griffiths. "Perfusion CT: a worthwhile enhancement?" In: *The British journal of radiology* 76.904 (2003), pp. 220–231.

[MHD93a] K. A. Miles, M. P. Hayball, and A. K. Dixon. "Functional images of hepatic perfusion obtained with dynamic CT." In: *Radiology* 188.2 (1993), pp. 405–411. ISSN: 0033-8419, 1527-1315. DOI: 10.1148/radiology.188.2.8327686.

[MHD93b] K. A. Miles, M. P. Hayball, and A. K. Dixon. "Functional images of hepatic perfusion obtained with dynamic CT." In: *Radiology* 188.2 (1993), pp. 405–411.

[Mil12] K. A. Miles, T. Y. Lee, V. Goh, E. Klotz, C. Cuenod, S. Bisdas, A. M. Groves, M. P. Hayball, R. Alonzi, and T. Brunner. "Current status and guidelines for the assessment of tumour vascular support with dynamic contrast-enhanced computed tomography." In: *European Radiology* 22.7 (2012), pp. 1430–1441. ISSN: 09387994. DOI: 10.1007/s00330-012-2379-4.

[Mil02] K. Miles. "Functional computed tomography in oncology." In: *European Journal of Cancer* 38.16 (2002), pp. 2079–2084.

[Mil91] K. Miles. "Measurement of tissue perfusion by dynamic computed tomography." In: *The British journal of radiology* 64.761 (1991), pp. 409–412.

[Mil99] K. Miles. "Tumour angiogenesis and its relation to contrast enhancement on computed tomography: a review." In: *European journal of radiology* 30.3 (1999), pp. 198–205.

[Mom03] A. Momose, S. Kawamoto, I. Koyama, Y. Hamaishi, K. Takai, and Y. Suzuki. "Demonstration of X-ray Talbot interferometry." In: *Japanese journal of applied physics* 42.7B (2003), p. L866.

[Mom96] A. Momose, T. Takeda, Y. Itai, and K. Hirano. "Phase–contrast X–ray computed tomography for observing biological soft tissues." In: *Nature medicine* 2.4 (1996), pp. 473–475.

[Mos90] M. E. Moseley, Y. Cohen, J. Kucharczyk, J. Mintorovitch, H. Asgari, M. Wendland, J. Tsuruda, and D. Norman. "Diffusion-weighted MR imaging of anisotropic water diffusion in cat central nervous system." In: *Radiology* 176.2 (1990), pp. 439–445.

[MRA14] M. Mischi, N. Rognin, and M. Averkiou. "Ultrasound imaging modalities." In: (2014).

[MT77] F. Mosteller and J. W. Tukey. "Data analysis and regression: a second course in statistics." In: *Addison-Wesley Series in Behavioral Science: Quantitative Methods* (1977).

[Mur05] K. Murase, T. Nanjo, S. Ii, S. Miyazaki, M. Hirata, Y. Sugawara, M. Kudo, K. Sasaki, and T. Mochizuki. "Effect of x-ray tube current on the accuracy of cerebral perfusion parameters obtained by CT perfusion studies." In: *Physics in medicine and biology* 50.21 (2005), p. 5019.

[MW14] E. Maire and P. J. Withers. "Quantitative X-ray tomography." In: *International materials reviews* 59.1 (2014), pp. 1–43.

[Nak05] Y. Nakayama, K. Awai, Y. Funama, M. Hatemura, M. Imuta, T. Nakaura, D. Ryu, S. Morishita, S. Sultana, N. Sato, et al. "Abdominal CT with low tube voltage: preliminary observations about radiation dose, contrast enhancement, image quality, and noise." In: *Radiology* 237.3 (2005), pp. 945–951.

[Nas14] M. L. F. Nascimento. "Brief history of X-ray tube patents." In: *World Patent Information* 37 (2014), pp. 48–53.

[Neg12] N. Negi, T. Yoshikawa, Y. Ohno, Y. Somiya, T. Sekitani, N. Sugihara, H. Koyama, T. Kanda, N. Kanata, T. Murakami, et al. "Hepatic CT perfusion measurements: a feasibility study for radiation dose reduction using new image reconstruction method." In: *European journal of radiology* 81.11 (2012), pp. 3048–3054.

[Net10] B. E. Nett, R. Brauweiler, W. Kalender, H. Rowley, and G.-H. Chen. "Perfusion measurements by micro-CT using prior image constrained compressed sensing (PICCS): initial phantom results." In: *Physics in medicine and biology* 55.8 (2010), p. 2333.

[New04] I. Newton. "Opticks: Or a treatise of the reflexions, refractions, inflexions and colours of light." In: (1704).

[Odh01] C. Odhner. *The Nobel Prize in Physics 1901*. 1901.

[Ogu14] H. Ogul, M. Kantarci, B. Genç, B. Pirimoglu, N. Çullu, Y. Kizrak, Ö. Yilmaz, and N. Karabulut. "Perfusion CT imaging of the liver: review of clinical applications." In: *Diagnostic and Interventional Radiology* 20.5 (2014), p. 379.

[OKM11] M. Okada, T. Kim, and T. Murakami. "Hepatocellular nodules in liver cirrhosis: state of the art CT evaluation (perfusion CT/volume helical shuttle scan/dual-energy CT, etc.)" In: *Abdominal imaging* 36.3 (2011), pp. 273–281.

[Oli11] E. F. Oliveira, S. B. Melo, C. C. Dantas, D. A. Vasconcelos, and F. Cadiz. "Comparison among tomographic reconstruction algorithms with a limited data." In: *International Nuclear Atlantic Conference-INAC 2011*. 2011.

[oth60] and others. *X-ray tubes*. US Patent 2,952,790. Sept. 1960.

[Pan05] P. V. Pandharipande, G. A. Krinsky, H. Rusinek, and V. S. Lee. "Perfusion imaging of the liver: current challenges and future goals 1." In: *Radiology* 234.3 (2005), pp. 661–673.

[Pel14a] G. Pelzer, A. Zang, G. Anton, F. Bayer, F. Horn, M. Kraus, J. Rieger, A. Ritter, J. Wandner, T. Weber, A. Fauler, M. Fiederle, W. S. Wong, M. Campbell, J. Meiser, P. Meyer, J. Mohr, and T. Michel. "Energy weighted x-ray dark-field imaging." In: *Opt. Express* 22.20 (Oct. 2014), pp. 24507–24515. DOI: 10.1364/OE.22.024507.

[Pel14b] G. Pelzer, A. Zang, G. Anton, F. Bayer, F. Horn, M. Kraus, J. Rieger, A. Ritter, J. Wandner, T. Weber, et al. "Energy weighted x-ray dark-field imaging." In: *Optics express* 22.20 (2014), pp. 24507–24515.

[Pfe06a] F. Pfeiffer, T. Weitkamp, O. Bunk, and C. David. "Phase retrieval and differential phase-contrast imaging with low-brilliance X-ray sources." In: *Nat. phys.* 2.4 (2006), pp. 258–261.

[Pfe06b] F. Pfeiffer, T. Weitkamp, O. Bunk, and C. David. "Phase retrieval and differential phase-contrast imaging with low-brilliance X-ray sources." In: *Nature Physics* 2.4 (2006), pp. 258–261. ISSN: 1745-2473. DOI: 10.1038/nphys265.

[Pfe07] F. Pfeiffer, C. Kottler, O. Bunk, and C. David. "Hard x-ray phase tomography with low-brilliance sources." In: *Physical review letters* 98.10 (2007), p. 108105.

[Pfe08a] F. Pfeiffer, M. Bech, O. Bunk, P. Kraft, E. F. Eikenberry, C. Brönnimann, C. Grünzweig, and C. David. "Hard-X-ray dark-field imaging using a grating interferometer." In: *Nature Materials* 7.2 (2008), pp. 134–137. ISSN: 1476-1122. DOI: 10.1038/nmat2096.

[Pfe08b] F. Pfeiffer, M. Bech, O. Bunk, P. Kraft, E. F. Eikenberry, C. Brönnimann, C. Grünzweig, and C. David. "Hard-X-ray dark-field imaging using a grating interferometer." In: *Nat. mat.* 7.2 (2008), pp. 134–137.

[Pot12] G. Potdevin, A. Malecki, T. Biernath, M. Bech, T. H. Jensen, R. Feidenhans'l, I. Zanette, T. Weitkamp, J. Kenntner, J. Mohr, P. Roschger, M. Kerschnitzki, W. Wagermaier, K. Klaushofer, P. Fratzl, and F. Pfeiffer. "X-ray vector radiography for bone micro-architecture diagnostics." In: *Physics in Medicine and Biology* 57.11 (2012), p. 3451.

[Pou16] A. Pourmorteza, H. Dang, J. Siewerdsen, and J. W. Stayman. "Reconstruction of difference in sequential CT studies using penalized likelihood estimation." In: *Physics in medicine and biology* 61.5 (2016), p. 1986.

[Pra15] F. Prade, A. Yaroshenko, J. Herzen, and F. Pfeiffer. "Short-range order in mesoscale systems probed by X-ray grating interferometry." In: *EPL (Europhysics Letters)* 112.6 (2015), p. 68002.

[PRG16] A. du Plessis, S. G. le Roux, and A. Guelpa. "Comparison of medical and industrial X-ray computed tomography for non-destructive testing." In: *Case Studies in Nondestructive Testing and Evaluation* 6 (2016), pp. 17–25.

[Qia10] L. J. Qian, Z. G. Zhuang, Y. F. Cheng, Q. Xia, J. J. Zhang, and J. R. Xu. "Hemodynamic alterations in anterior segment of liver graft after right-lobe living-donor liver transplantation: computed tomography perfusion imaging findings." In: *Abdominal imaging* 35.5 (2010), pp. 522–527.

[Rad86] J. Radon. "On the determination of functions from their integral values along certain manifolds." In: *IEEE transactions on medical imaging* 5.4 (1986), pp. 170–176.

[Rev11] V. Revol, I. Jerjen, C. Kottler, P. Schütz, R. Kaufmann, T. Lüthi, U. Sennhauser, U. Straumann, and C. Urban. "Sub-pixel porosity revealed by x-ray scatter dark field imaging." In: *J. of App. Phys.* 110.4 (2011), p. 044912.

[Rit06] J. W. Ritter. "Bemerkungen zu Herschel?s neueren Untersuchungen über das Licht." In: *Physisch-Chemische Abhandlungen, in chronologischen Folge. II Band. Leipzig: Reclam* (1806), pp. 81–107.

[Rod01] A. Rode, B. Bancel, P. Douek, M. Chevallier, V. Vilgrain, G. Picaud, L. Henry, F. Berger, T. Bizollon, J.-L. Gaudin, et al. "Small nodule detection in cirrhotic livers: evaluation with US, spiral CT, and MRI and correlation with pathologic examination of explanted liver." In: *Journal of computer assisted tomography* 25.3 (2001), pp. 327–336.

[ROF92] L. I. Rudin, S. Osher, and E. Fatemi. "Nonlinear total variation based noise removal algorithms." In: *Phys. & Nonlin. Phen.* 60.1 (1992), pp. 259–268.

[Rön96] W. C. Röntgen. "On a new kind of rays." In: *Science* (1896), pp. 227–231.

[Ryd00] J. Rydberg, K. A. Buckwalter, K. S. Caldemeyer, M. D. Phillips, D. J. Conces Jr, A. M. Aisen, S. A. Persohn, and K. K. Kopecky. "Multisection CT: scanning techniques and clinical applications." In: *Radiographics* 20.6 (2000), pp. 1787–1806.

[Saa03] Y. Saad. *Iterative methods for sparse linear systems*. Vol. 82. siam, 2003.

[Sah07] D. V. Sahani, N.-S. Holalkere, P. R. Mueller, and A. X. Zhu. "Advanced hepatocellular carcinoma: CT perfusion of liver and tumor tissue–initial experience." In: *Radiology* 243.3 (2007), pp. 736–743. ISSN: 0033-8419. DOI: 10.1148/radiol.2433052020.

[Sch16] L. Schoeman, P. Williams, A. du Plessis, and M. Manley. "X-ray micro-computed tomography (μCT) for non-destructive characterisation of food microstructure." In: *Trends in Food Science & Technology* 47 (2016), pp. 10–24.

[Sch13] S. Schleede. "X-ray Phase-Contrast Imaging at a Compact Laser-Driven Synchrotron Source." PhD thesis. München, Technische Universität München, Diss., 2013, 2013.

[Set06] A. Sethi. "X-Rays: Interaction with Matter." In: *Encyclopedia of Medical Devices and Instrumentation* (2006).

[Sey13a] S. Seyyedi, K. Cengiz, M. Kamasak, and I. Yildirim. "An object-oriented simulator for 3D digital breast tomosynthesis system." In: *2013 8th International Symposium on Image and Signal Processing and Analysis (ISPA)*. Sept. 2013, pp. 262–267. DOI: 10.1109/ISPA.2013.6703750.

[Sey13b] S. Seyyedi, K. Cengiz, M. Kamasak, and I. Yildirim. "An object-oriented simulator for 3D digital breast tomosynthesis imaging system." In: *Computational and mathematical methods in medicine* 2013 (2013).

[Sey16a] S. Seyyedi, M. Wieczorek, C. Jud, F. Pfeiffer, and T. Lasser. "A Regularized X-ray Tensor Tomography Reconstruction Technique." In: *4th International Conference on Image Formation in X-Ray Computed Tomography*. July 2016.

[Sey16b] S. Seyyedi, M. Wieczorek, Y. Sharma, F. Schaff, C. Jud, F. Pfeiffer, and T. Lasser. "Component-based TV regularization for X-ray tensor tomography." In: *Biomedical Imaging (ISBI), 2016 IEEE 13th International Symposium on*. IEEE. 2016, pp. 581–584.

[Sey18a] S. Seyyedi, E. Liapi, T. Lasser, R. Ivkov, R. Hatwar, and J. W. Stayman. "Low-Dose CT Perfusion of the Liver using Reconstruction of Difference." In: *IEEE Transactions on Radiation and Plasma Medical Sciences* PP.99 (2018), pp. 1–1. ISSN: 2469-7311. DOI: 10.1109/TRPMS.2018.2812360.

[Sey18b] S. Seyyedi, M. Wieczorek, F. Pfeiffer, and T. Lasser. "Incorporating a Noise Reduction Technique Into X-Ray Tensor Tomography." In: *IEEE Transactions on Computational Imaging* 4.1 (Mar. 2018), pp. 137–146. DOI: 10.1109/TCI.2018.2794740.

[Sey18c] S. Seyyedi, M. Wieczorek, F. Pfeiffer, and T. Lasser. "Incorporating a Noise Reduction Technique into X-ray Tensor Tomography." In: *IEEE Transactions on Computational Imaging* (2018).

[Sey14] S. Seyyedi. "Sayısal Meme Tomosentezi Görüntülemenin Toplam Değişinti Minimizasyonu Kullanarak Sıkıştırılmış Algılama Yöntemleri Temelli Benzetimi, Değerlendirmesi Ve Çalışması." MA thesis. Fen Bilimleri Enstitüsü, 2014.

[Sha16] Y. Sharma, M. Wieczorek, F. Schaff, S. Seyyedi, F. Prade, F. Pfeiffer, and T. Lasser. "Six dimensional X-ray Tensor Tomography with a compact laboratory setup." In: *Applied Physics Letters* 109.13 (2016), p. 134102.

[She94] J. R. Shewchuk et al. *An introduction to the conjugate gradient method without the agonizing pain*. 1994.

[Shu15] K. K. Shung. *Diagnostic ultrasound: Imaging and blood flow measurements*. CRC press, 2015.

[Sid11] S. Sidhu, G. Falzon, S. Hart, J. Fox, R. Lewis, and K. Siu. "Classification of breast tissue using a laboratory system for small-angle x-ray scattering (SAXS)." In: *Phys. in med. and bio.* 56.21 (2011), p. 6779.

[Sin10] S. Singh, M. K. Kalra, J. Hsieh, P. E. Licato, S. Do, H. H. Pien, and M. A. Blake. "Abdominal CT: comparison of adaptive statistical iterative and filtered back projection reconstruction techniques." In: *Radiology* 257.2 (2010), pp. 373–383.

[SK17] J. Seo and Y.-s. Kim. *Ultrasound imaging and beyond: recent advances in medical ultrasound*. 2017.

[SL05] S. K. Shetty and M. H. Lev. "CT perfusion in acute stroke." In: *Neuroimaging clinics of North America* 15.3 (2005), pp. 481–501.

[Sni95] A. Snigirev, I. Snigireva, V. Kohn, S. Kuznetsov, and I. Schelokov. "On the possibilities of x-ray phase contrast microimaging by coherent high-energy synchrotron radiation." In: *Rev. of Sci. Ins.* 66.12 (1995), pp. 5486–5492.

[SP08] E. Y. Sidky and X. Pan. "Image reconstruction in circular cone-beam computed tomography by constrained, total-variation minimization." In: *Physics in medicine and biology* 53.17 (Sept. 2008), pp. 4777–4807.

[Spa94] C. Sparks. *Resonant anomalous X-ray scattering: theory and applications*. North Holland, 1994.

[Sta12] J. W. Stayman, Y. Otake, J. L. Prince, A. J. Khanna, and J. H. Siewerdsen. "Model-based tomographic reconstruction of objects containing known components." In: *IEEE transactions on medical imaging* 31.10 (2012), pp. 1837–1848.

[Sta13] J. W. Stayman, H. Dang, Y. Ding, and J. H. Siewerdsen. "PIRPLE: a penalized-likelihood framework for incorporation of prior images in CT reconstruction." In: *Physics in medicine and biology* 58.21 (2013), p. 7563.

[Sti52] E. Stiefel. "Über einige methoden der relaxationsrechnung." In: *Zeitschrift für angewandte Mathematik und Physik ZAMP* 3.1 (1952), pp. 1–33.

[SV82] L. A. Shepp and Y. Vardi. "Maximum likelihood reconstruction for emission tomography." In: *IEEE transactions on medical imaging* 1.2 (1982), pp. 113–122.

[SY14a] S. Seyyedi and I. Yildirim. "3D digital breast tomosynthesis image reconstruction using anisotropic total variation minimization." In: *2014 36th Annual International Conference of the IEEE Engineering in Medicine and Biology Society*. Aug. 2014, pp. 6052–6055. DOI: 10.1109/EMBC.2014.6945009.

[SY14b] S. Seyyedi and I. Yildirim. "3D digital breast tomosynthesis image reconstruction using anisotropic total variation minimization." In: *Engineering in Medicine and Biology Society (EMBC), 2014 36th Annual International Conference of the IEEE*. IEEE. 2014, pp. 6052–6055.

[Sza04] T. L. Szabo. *Diagnostic ultrasound imaging: inside out*. Academic Press, 2004.

[Ter83] M. M. Ter-Pogossian. "Positron emission tomography (PET)." In: *Diagnostic Imaging in Medicine*. Springer, 1983, pp. 273–277.

[Tik63] A. Tikhonov. "Solution of incorrectly formulated problems and the regularization method." In: *Soviet Meth. Dokl.* 4 (1963), pp. 1035–1038.

[Uns99] M. Unser. "Splines: A perfect fit for signal and image processing." In: *IEEE Signal processing magazine* 16.6 (1999), pp. 22–38.

[Van11] G. Van Gompel, K. Van Slambrouck, M. Defrise, K. J. Batenburg, J. de Mey, J. Sijbers, and J. Nuyts. "Iterative correction of beam hardening artifacts in CT." In: *Medical physics* 38.S1 (2011).

[Van79] A. Van Steenbergen. "Synchrotron radiation sources." In: *IEEE Transactions on Nuclear Science* 26.3 (1979), pp. 3785–3790.

[Vel13] A. Velroyen, M. Bech, A. Malecki, A. Tapfer, A. Yaroshenko, M. Ingrisch, C. C. Cyran, S. D. Auweter, K. Nikolaou, M. Reiser, and F. Pfeiffer. "Microbubbles as a scattering contrast agent for grating-based x-ray dark-field imaging." In: *Physics in Medicine and Biology* 58.4 (2013), N37.

[VLR13] V. Vardhanabhuti, R. Loader, and C. A. Roobottom. "Assessment of image quality on effects of varying tube voltage and automatic tube current modulation with hybrid and pure iterative reconstruction techniques in abdominal/pelvic CT: a phantom study." In: *Investigative radiology* 48.3 (2013), pp. 167–174.

[Vog15] J. Vogel, F. Schaff, A. Fehringer, C. Jud, M. Wieczorek, F. Pfeiffer, and T. Lasser. "Constrained X-ray tensor tomography reconstruction." In: *Opt. exp.* 23.12 (2015), pp. 15134–15151.

[Vog15] J. Vogel. "Tomographic Reconstruction beyond Classical X-ray CT." PhD thesis. Technische Universität München, 2015.

[Vor11] G. A. Vorona, R. C. Ceschin, B. L. Clayton, T. Sutcavage, S. S. Tadros, and A. Panigrahy. "Reducing abdominal CT radiation dose with the adaptive statistical iterative reconstruction technique in children: a feasibility study." In: *Pediatric radiology* 41.9 (2011), pp. 1174–1182.

[VSK85] Y. Vardi, L. Shepp, and L. Kaufman. "A statistical model for positron emission tomography." In: *Journal of the American statistical Association* 80.389 (1985), pp. 8–20.

[VV86] A. Van der Sluis and H. A. van der Vorst. "The rate of convergence of conjugate gradients." In: *Numerische Mathematik* 48.5 (1986), pp. 543–560.

[Wah12] B. Wahlberg, S. Boyd, M. Annergren, and Y. Wang. "An ADMM algorithm for a class of total variation regularized estimation problems." In: *IFAC Proceedings Volumes* 45.16 (2012), pp. 83–88.

[Wan14] Z. Wang, N. Hauser, G. Singer, M. Trippel, R. A. Kubik-Huch, C. W. Schneider, and M. Stampanoni. "Non-invasive classification of microcalcifications with phase-contrast X-ray mammography." In: *Nature communications* 5 (2014).

[War16] J. M. Warnett, V. Titarenko, E. Kiraci, A. Attridge, W. R. Lionheart, P. J. Withers, and M. A. Williams. "Towards in-process x-ray CT for dimensional metrology." In: *Measurement Science and Technology* 27.3 (2016), p. 035401.

[Wei05] C. Weidekamm, M. Cejna, L. Kramer, M. Peck-Radosavljevic, and T. R. Bader. "Effects of TIPS on liver perfusion measured by dynamic CT." In: *American Journal of Roentgenology* 184.2 (2005), pp. 505–510.

[WFV00] G. Wang, T. Frei, and M. W. Vannier. "Fast iterative algorithm for metal artifact reduction in X-ray CT." In: *Academic radiology* 7.8 (2000), pp. 607–614.

[Wie16] M. Wieczorek, F. Schaff, F. Pfeiffer, and T. Lasser. "Anisotropic X-Ray Dark-Field Tomography: A Continuous Model and its Discretization." In: *Physical Review Letters* 117.15 (2016), p. 158101.

[Wil13] M. J. Willemink, P. A. de Jong, T. Leiner, L. M. de Heer, R. A. Nievelstein, R. P. Budde, and A. M. Schilham. "Iterative reconstruction techniques for computed tomography Part 1: technical principles." In: *European radiology* 23.6 (2013), pp. 1623–1631.

[Wil91] K. Wille. "Synchrotron radiation sources." In: *Reports on Progress in Physics* 54.8 (1991), p. 1005.

[Win05] M. Wintermark, M. Sesay, E. Barbier, K. Borbély, W. P. Dillon, J. D. Eastwood, T. C. Glenn, C. B. Grandin, S. Pedraza, J.-F. Soustiel, et al. "Comparative overview of brain perfusion imaging techniques." In: *Stroke* 36.9 (2005), e83–e99.

[Win97] H. Winick. "Synchrotron radiation sources: Past, present and future." In: *Röntgen Centennial, X-rays in Natural and Life Sciences. World Scientific* (1997), pp. 45–64.

[WK03] A. Webb and G. C. Kagadis. "Introduction to biomedical imaging." In: *Medical Physics* 30.8 (2003), pp. 2267–2267.

[WME84] G. E. Wesbey, M. E. Moseley, and R. L. Ehman. "Translational molecular self-diffusion in magnetic resonance imaging. II. Measurement of the self-diffusion coefficient." In: *Investigative radiology* 19.6 (1984), pp. 491–498.

[WVL14] M. Wieczorek, J. Vogel, and T. Lasser. "CampRecon - a software framework for linear inverse problems." In: *TUM Technical Report* (2014). DOI: I1401.

[Xu17] S. Xu, A. Uneri, A. J. Khanna, J. Siewerdsen, and J. W. Stayman. "Polyenergetic known-component CT reconstruction with unknown material compositions and unknown x-ray spectra." In: *Physics in Medicine & Biology* 62.8 (2017), p. 3352.

[Yar13] A. Yaroshenko, F. G. Meinel, M. Bech, A. Tapfer, A. Velroyen, S. Schleede, S. Auweter, A. Bohla, A. Ö. Yildirim, K. Nikolaou, et al. "Pulmonary emphysema diagnosis with a preclinical small-animal x-ray dark-field scatter-contrast scanner." In: *Radiology* 269.2 (2013), pp. 427–433.

[Yas11] W. Yashiro, S. Harasse, K. Kawabata, H. Kuwabara, T. Yamazaki, and A. Momose. "Distribution of unresolvable anisotropic microstructures revealed in visibility-contrast images using x-ray Talbot interferometry." In: *Physical Review B* 84.9 (2011), p. 094106.

[Zha17] C. Zhang, W. Zbijewski, X. Zhang, S. Xu, and J. Stayman. "Polyenergetic known-component reconstruction without prior shape models." In: *Medical Imaging 2017: Physics of Medical Imaging*. Vol. 10132. International Society for Optics and Photonics. 2017, 101320O.

Index

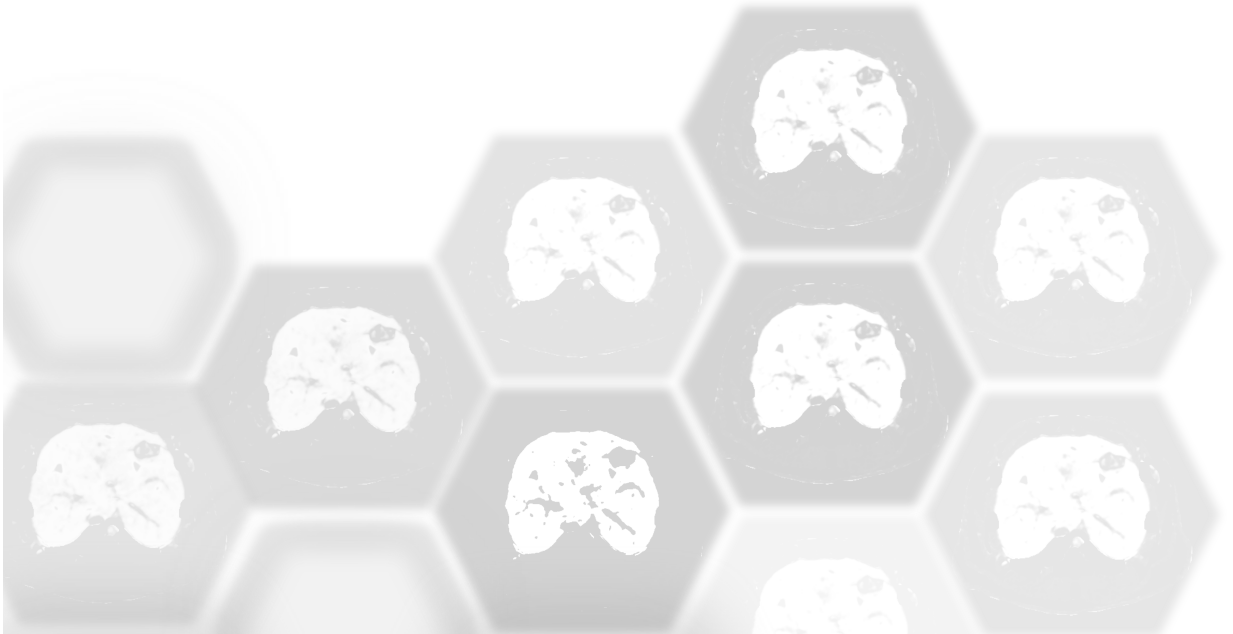

Doctoral Thesis
Technical University of Munich
Department of Informatics
July 2018